EPFL

Thèse n° 8915

Quantum dynamics in individual surface spins

Présentée le 21 septembre 2021

Faculté des sciences de base
IPHYS - Gestion
Programme doctoral en physique

pour l'obtention du grade de Docteur ès Sciences

par

Tobias BILGERI

Acceptée sur proposition du jury

Prof. C. Hébert, présidente du jury
Prof. H. Brune, directeur de thèse
Prof. A. F. Otte, rapporteur
Dr C. Lutz, rapporteur
Prof. J.-Ph. Ansermet, rapporteur

École
polytechnique
fédérale
de Lausanne

2021

It is not knowledge,
but the act of learning,
not possession but the act of getting there,
which grants the greatest enjoyment.
— Carl Friedrich Gauss

Dedicated to my family.

Acknowledgements

I would like to offer my sincere gratitude to Harald for inviting me to join his group and offering me the chance to carry out my doctoral thesis under his guidance. I would like to thank Fabian for introducing me to ESR-STM, and Johannes for elevating our laboratory standards to a new level. I would also like to thank all the other current and former doctoral students and post-docs I worked with in our team, many of you have become dear friends. On the other side of the globe, I would like to thank my amazing collaborators in Korea. It was a life changing experience to be hosted in your country for 10 months. I would also like to thank all those that supervised me during previous research projects, including C. Brun, T. Cren, A. Sukhovich, J. Fink and A. Grüneis, the lessons you taught me greatly helped me throughout this work.

Most importantly, I have to thank my family. I am truly gifted to have such amazing people by my side. This work would not be possible without your continuous support.

Lausanne, August 24, 2021 T. B.

Abstract

This thesis presents a combined experimental and theoretical study of the classical and quantum magnetization dynamics in single magnetic adatoms and molecules, and on the classical and quantum coherent control thereof.

First, a detailed description of the methods and in particular electron spin resonance scanning tunneling spectroscopy is given. Next, we give a detailed account of how to experimentally update a standard scanning tunneling microscope for such experiments, which ultimately lead us to set up the world's second microscope with such capabilities. Subsequently, we show how we iteratively improved the setup, and how we were able to achieve a transmission of radiofrequency voltages to the tunneling junction with almost no additional losses beyond the intrinsic limitations of the materials used, a great improvement compared to most setups presently in use.
Afterwards, we apply this technique to the metal-organic complex iron phthalocyanine. On MgO, we find it to form a spin-1/2 system, and we demonstrate quantum coherent control thereof, and investigate the magnetic interaction between surface-adsorbed molecules. Furthermore, we use this technique to experimentally demonstrate the magnetic stability of Dy adatoms on MgO. We find that this system, by several metrics, represents the worlds most stable single atom magnet discovered thus far. Using the capability of scanning tunneling microscopes to perform atomic manipulation, we ensemble atomically precise Dy nanostructures. By classically controlling the magnetic orientation of the Dy atoms, we are thus able to store information long-term in single adatoms and nanostructures even in absence of an external field, and create nanomagnets and local magnetic fields with unprecedented precision and stability.
Finally, we investigate the magnetic properties of Ho/MgO. Depending on the precise adsorption site and charge configuration, we find either long lifetimes in the case of top-site $4f^{10}$ Ho, which was recently discovered as world's first single atom magnet, or fast sub-barrier relaxation due to strongly mixed quantum states. Using a novel theoretical approach, we are able to disentangle the different contributions of the individual species measured in ensemble-averaging X-ray absorption studies, and lift the discrepancies between previous X-ray and scanning tunneling microscopy based studies on Ho/MgO. By theoretically describing the perturbing effects of the experimental probes driving the spin degree of freedom out of thermal equilibrium, we are able to explain the measured dynamics in good agreement with the experimental data.

Key Words: magnetization dynamics, spintronics, open quantum systems, scanning tunneling microscopy, pulsed electron spin resonance, quantum sensing, x-ray absorption, single magnetic adatoms, single magnetic molecules

Résumé

Cette thèse présente une étude expérimentale et théorique combinée de la dynamique classique et quantique de l'aimantation dans des adatomes et des molécules magnétiques individuels, et de leur contrôle cohérent classique et quantique.

Au debut, une description détaillée des méthodes et en particulier de la microscopie à effet tunnel par résonance de spin électronique est donnée. Ensuite, nous expliquons en détail comment mettre à jour expérimentalement un microscope à effet tunnel standard pour de telles expériences, ce qui nous a finalement permis de mettre en place le deuxième microscope au monde équipé de telles capacités. Ensuite, nous montrons comment nous avons amélioré itérativement la configuration et comment nous avons réalisé une transmission de tensions radiofréquences à la jonction à effet tunnel sans presque aucune perte additionelle au-delà des limites des matériaux utilisés, une grande amélioration par rapport à la plupart des configurations actuellement utilisées.
Ensuite, nous appliquons cette technique au complexe métal-organique de phtalocyanine de fer. Sur MgO, nous découvrons qu'il forme un système de spin-1/2, nous démontrons son contrôle cohérent quantique et étudions l'interaction magnétique entre les molécules individuelles adsorbées en surface. De plus, nous utilisons cette technique pour démontrer expérimentalement la stabilité magnétique des adatomes de Dy sur MgO. Nous constatons que ce système, selon plusieurs paramètres, représente l'aimant monoatomique le plus stable au monde découvert à ce jour. En utilisant la capacité des microscopes à effet tunnel à effectuer des manipulations atomiques, nous assemblons des nanostructures de Dy avec une précision atomique. En contrôlant classiquement l'orientation magnétique des atomes de Dy, nous sommes ainsi capables de stocker des informations à long-terme dans des nanostructures monoatomiques, même en l'absence de champ externe, et de créer des nano-aimants et des champs magnétiques locaux avec une précision et une stabilité sans précédent.
Enfin, nous étudions les propriétés magnétiques de Ho/MgO. Dépendant du site d'adsorption et de la configuration de la charge, nous trouvons soit de la stabilité magnetique de longues durée dans le cas du $4f^{10}$ Ho adsorbé sur O, qui a été récemment découvert comme le premier aimant atomique stable au monde, soit une relaxation rapide par effet tunnel due à des états quantiques fortement mélangés. En utilisant une nouvelle approche théorique, nous sommes capables de distinguer les différentes contributions des espèces individuelles mesurées dans les études macroscopiques d'absorption de rayons X, et de lever les divergences entre les études précédentes basées sur les rayons X et la microscopie à effet tunnel sur Ho/MgO. En

expliquant théoriquement les effets perturbateurs des sondes expérimentales entraînant le degré de liberté du spin hors de l'équilibre thermique, nous sommes capable d'expliquer la dynamique mesurée en bon accord avec les données expérimentales.

Mot-clefs : dynamique de l'aimantation, spintronique, systèmes quantiques ouverts, microscopie à effet tunnel, résonance de spin électronique pulsée, détection quantique, absorption des rayons X, adatomes magnétiques individuels, molécules magnétiques individuels.

Zusammenfassung

Diese Arbeit kombiniert experimentelle und theoretische Ansätze zur Erforschung von klassischer und quantenphysikalischer Magnetisierungsdynamik in einzelnen magnetischen Adatomen und Molekülen, sowie von klassischer und quantenkohärenter Kontrolle des magnetischen Zustands dieser Systeme.

Zuerst präsentieren wir eine detaillierte Einführung in die verwendeten Methoden, mit besonderem Fokus auf Rastertunnelmikroskop basierten Elektronenspinresonanzexperimenten. Der erste Teil der Forschungsarbeit beschäftigte sich mit dem Aufrüsten eines klassischen Rastertunnelmikroskops für Experimente solcherart. Im Zuge dieser Arbeit erbauten wir das zweite Rastertunnelmikroskop weltweit mit Spinresonanz-Fähigkeiten, was im Detail beschrieben wird. Im Anschluss dessen zeigen wir iterative Verbesserungen, insbesondere mit Bezug auf die Radiofrequenztransmission. Hierbei erreichten wir, dass die Wechselspannung fast ohne über die intrinsische Materiallimitierung hinausgehende Verluste zum Tunnelübergang zu geführt werden kann, was eine grosse Verbesserung zu den meisten verwendeten Systemen darstellt.
Anschliessend wenden wir diese Technik zur Untersuchung der metallorganischen Verbindung Eisen-Phthalocyanine an. Diese Verbindung bildet auf MgO ein Spin-1/2 System, welches wir über lokale Elektronenspinresonanz quantenkohärent manipulieren. Darüber hinaus untersuchen wir die anisotropische magnetische Wechselwirkung zwischen einzelnen Moleküle.
Im Anschluss untersuchen wir Dy Adatatome mit unterschiedlichen, Rastertunnelmikroskop basierenden Experimenten. Wir finden, dass dieses System anhand mehrerer Bewertungskriterien das magnetisch stabilste, bisher entdeckte Adatom darstellt. Wir verwenden die Fähigkeit des Mikroskops zur strukturellen Manipulation einzelner Atome, um atomar präzise definierte Nanostrukturen herzustellen. Somit sind wir in der Lage, klassische Information in magnetischen Nanostrukturen langfristig auch in Abwesenheit eines externen magnetischen Feldes zu speichern, sowie stabile nanomagnetische Strukturen mit bisher unbekannter Präzision und Stabilität zu erschaffen.
Zuletzt erforschen wir im Detail die magnetischen Eigenschaften von Ho/MgO als Funktion der Adsorbtionsstelle und der Ladungskonfiguration. Für $4f^{10}$ Ho adsorbiert auf O finden wir langlebige magnetische Stabilität, in Übereinstimmung mit jüngsten Studien, die in diesem System zum ersten mal langfristige magnetische Stabilität in einzelnen Adatomen entdeckt haben. Für zwischen O und Mg adsorbiertes $4f^{10}$ Ho, sowie für $4f^{11}$ Ho, finden wir stark gemischte Quantenzustände und daraus resultierend kurzlebige magnetische Zustän-

de aufgrund eines effizienten quantenmechanischen Tunneleffekts. Anhand eines neuen theoretischen Ansatzes können wir die unterschiedlichen Beiträge dieser Spezien zu makroskopischen, Röntgenstrahlung basierten Experimenten entflechten und einzeln betrachten. Dieser Ansatz erlaubt es uns zudem, Unstimmigkeiten in der bisherigen Interpretation von auf Rastertunnelmikroskop und Röntgenstrahlung basierten Experimenten zu erklären. Des Weiteren können wir, unter detaillierter Beschreibung des Einflusses der experimentellen Probe, beschreiben, wie die experimentelle Beobachtung den magnetischen Freiheitsgrad aus dem thermischen Gleichgewicht hebt, und finden ultimativ eine sehr gute Übereinstimmung zwischen theoretisch vorhergesagter und experimentell beobachteter Magnetisierungsdynamik.

Schlagwörter: Magnetisierungsdynamik, Spintronik, offene Quantensysteme, Rastertunnelmikroskopie, gepulste Elektronenspinresonanz, Quantensensorik, Röntgenabsorption, einzelne magnetische Adatome, einzelne magnetische Moleküle

Contents

List of Figures

List of Tables

Introduction

Modern society has an ever increasing demand for information processing. This trend is first and foremost possible through technological advances in computational power and data storage. Easy and cheap availability thereof is fundamental to what some call the fourth industrial revolution, which refers to a new wave of automation through tools such as advanced sensing, internet of things, big data, machine learning and artificial intelligence. This ever increasing demand naturally leads to an increased use of resources and energy, and therefore leads to the question of how information processing can be done more efficiently. Here, modern physics is again the forefront of progress, and novel technologies based on spintronics, modern quantum materials, quantum sensing, and quantum information processing are highly sought after to make information processing more efficient, and in some cases to make wholly new applications possible. In this work, we investigate quantum dynamics in individual spins on surfaces. These spins represent an open quantum system and are either given by single adatoms or single molecules on surfaces. Both these systems are promising platforms for classical and quantum information processing. The classical route requires among other things accessibility to read and write magnetic states, as well the intrinsic ability to store this information over extended periods of time. Quantum sensing, quantum simulation and quantum information processing often require great experimental resolution or the ability to perform sufficiently fast quantum coherent control within the available quantum coherence time. On the technical side, new experimental setups have to be created to carry out modern experiments. On the theoretical side, relevant factors on the intrinsic and extrinsically induced static and dynamic properties have to be analyzed and routes toward optimization thereof have to be found. All these tasks were carried out as part of this thesis and are documented here in detail.

Regarding classical information storage in individual spins, for a long time after the discovery of single molecule magnets (SMM) [1], the search for magnetic stability at elevated temperatures has been relatively stagnant and magnetic stability above a few Kelvin has remained elusive. Single magnetic adatoms (SAM) are a comparably young field of research, with first hints towards significant magnetic anisotropy appearing relatively recently in 2003 [2]. Nonetheless SAMs were the first system to show significant magnetic stability at temperatures up to approx. 40 K [3]. In recent years, SMMs closed this gap and complexes with thermal sta-

bility up to 80 K have been created [4]. At the same time, a different path of research attempted to exploit the properties of such individual spin centers for potential applications in quantum information. Some of the most recent highlights of research on magnetic molecules include the observation of long lived Rabi oscillations at room temperature [5] or the implementation of a quantum algorithm using all electric control of nuclear spins in single magnetic molecules [6]. With respect to single spins on surfaces, such kinds of experiments became thinkable only recently with the discovery of electron spin resonance (ESR) scanning tunneling microscopy (STM) [7], with the first and until this work only example of coherent manipulation being published as late as 2019 [8].

Some of the first STM signatures of single spins on surfaces have been observed through many-body interactions with metallic and superconducting substrates [9–11]. In 2003, using X-ray absorption measurements, it was discovered that single spins on surfaces can possess a giant magnetic anisotropy of several meV per atom, which is a magnitude larger than what is typically observed in bulk materials [2]. Shortly after, the first STM study of a single magnetic adatom appeared [12]. In this study, the spin was characterized through inelastic scattering of the tunneling electrons which leads to characteristic steps in differential conductance spectra. Furthermore, the authors in ref. [12] used a thin insulating film to decouple the spin from the electron bath of the substrate, a technique followed in many studies up to this date. A few years later, first single adatom magnetization curves were measured using spin polarized (SP) currents of a magnetic tip [13]. In 2010, pump-probe measurements with temporal resolution down to the nanosecond range have been demonstrated in magnetic adatoms on copper nitride [14].

In 2016, the first ESR-STM experiments were published. This novel experimental tool allows investigating magnetic surface structures with an energy resolution enhanced by several orders of magnitude. A variety of phenomena could now be observed on the single adatom level, such as dipolar coupling between individual adatoms [15] and hyperfine couplings [16]. As recently demonstrated, this tool also allows for coherent manipulation of individual magnetic adatoms [8]. In this thesis we describe in detail how to set up such an experiment, and present the first observation of ESR and coherent manipulation of a single metal-organic molecule.

Again in 2016, using Synchrotron based X-ray measurements, the first SAM was discovered in Ho/MgO/Ag(100) [3]. The remarkable stability found in this study required several things: A large uniaxial anisotropy contribution stemming from the large spin of the lanthanide Ho in combination with the strong electrostatic interaction with the oxygen atom sitting underneath the Ho, a weak mixing of the lowest lying multiplets due to the weak off-diagonal crystal field contributions, and separation of the Ho from the conduction electrons using a thin insulating thin film. Equally, the proximity of the silver substrate is required to allow for a 4f10 charge

configuration, as will be demonstrated later. Most recently, we discovered Dy/MgO/Ag(100) to be the first similarly stable SAM with several additional remarkable properties compared to Ho.

The methods section of this thesis gives a general introduction to single spins on surfaces, approaches to describe them theoretically as well as experimental methods for characterization and control. The first results section deals with upgrading a conventional STM for ESR-STM. During the first year of this thesis, world's second ESR-STM was created, and based on the initial experience further upgrades to the experimental setup have been made. Afterwards, we present the first ESR study of individual metal-organic molecules on a surfaces as well as quantum coherent control thereof. The last two sections will deal with SAMs. First, an STM study of Dy/MgO/Ag(100) is introduced, whereby we find it to be world's most stable SAM. Afterwards, results on the theoretical description on the static and dynamic properties of world's first SAM, Ho/MgO/Ag(100), are given and compared the X-ray experiments.

1 Methods

The main experimental approaches to characterize single spins on surfaces are scanning tunneling microscope (STM) based methods and Synchrotron based x-ray methods, specifically x-ray absorption spectroscopy (XAS), x-ray magnetic circular dichroism (XMCD), and x-ray magnetic linear dichroism (XMLD). The reasons therefore are simple. STM naturally is a surface sensitive experimental method with sub-single-atom resolution and can detect discrete magnetic excitations in individual and coupled spins with high precision. X-ray based ensemble methods are the only ensemble methods with enough resolution to detect the magnetic properties of a diluted monolayer of spins (about 10^{12} spins per mm^2 given one spin each nm^2) and allows among other things to differentiate between orbital and spin contributions to the total angular momentum, and gives a direct view of the filling of the electronic levels. This chapter introduces these two techniques with a particular focus on advanced spin characterization and manipulation in STM experiments. Equally, to understand single surface spins from a theoretical point of view, multiplet calculations are introduced.

1.1 Scanning tunneling microscopy

The scanning tunneling microscope was invented by Binnig and Rohrer [17] in 1982. It allowed to investigate surfaces with unprecedented atomic resolution and the inventors were promptly rewarded by the Nobel prize in 1986. The fundamental building blocks are shown in fig. 1.1. Fundamentally, an atomically sharp needle is moved in parallel to the surface of a conductive sample. The sample is probed using an electric current typically in the pA to nA regime. By measuring in the tunneling regime at small voltages and currents, a much greater resolution was achieved compared to other techniques such as the topografiner invented a decade earlier by Young *et al.* [18]. The same team has also succeeded in measuring the transition from the field emission to the tunneling regime using piezoelectric elements as we do today, but failed to mechanically stabilize the system enough to observe atomic corrugations [19]. Following the initial discovery, a large set of tools has been added to the STM [20]. Exemplary, by placing the STM in an cryogenic environment, surface diffusion of single atoms can be suppressed and creating well defined nanostructures atom-by-atom became possible [21]. Using magnetic tips

to create spin-polarized currents allowed for atomic scale imaging of magnetic nanostructures [22]. A most recent technique is electron spin resonance (ESR) STM introduced by Baumann *et al.* in 2015 [7]. As no detailed review on this topic exists, this section will focus extensively on the fundamentals required to understand this novel tool. Excellent literature on other fundamental technical and theoretical aspects of scanning tunneling microscopy can be found for example in refs. [23, 24]

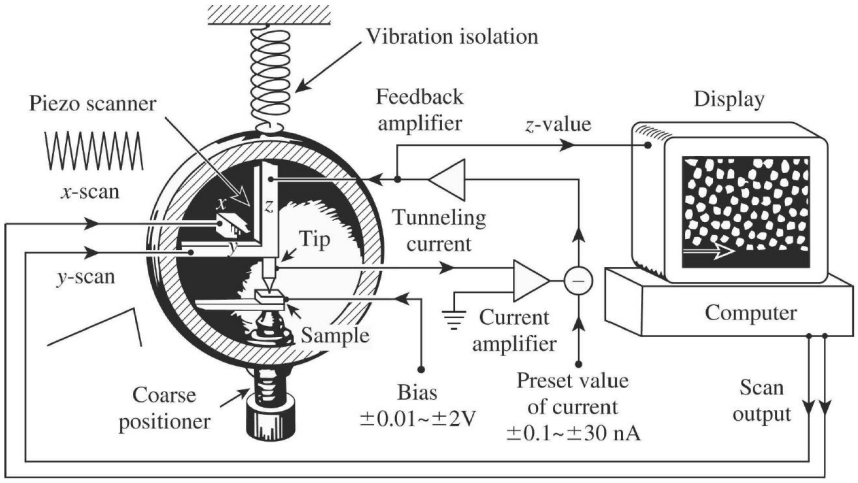

Figure 1.1: **STM Schematic**: On the left, an exemplary STM head is shown, whereas the electronic setup is displayed on the right. While the fundamental experimental setup has not changed since this schematic was published in C.J. Chen's classic introduction to STM in 1993 [23], several new tools have been added on top. Particularly relevant for this work is the ability of an STM to function in a cryogenic environment, as well as radio-frequency capabilities, which will be discussed in detail later.

1.1.1 Tunneling theory

Scanning tunneling microscopy fundamentally relies on the quantum mechanical tunneling. Here we present an introduction by looking at electron tunneling through a one-dimensional potential barrier, as schematically shown in fig. 1.2. In the single particle picture, the electron wave function $\varphi(z)$ must satisfy the Schroedinger equation

$$-\frac{\hbar^2}{2m}\frac{d^2}{dz^2}\varphi(z) = (E - V(z))\varphi(z) \tag{1.1}$$

The solution of the wave function in the three regions left and right of the barrier is given by an oscillating complex-valued probability density

$$\varphi(z) = \begin{cases} Ae^{ikz} + Be^{-ikz} & z < 0 \\ Ce^{\kappa z} + De^{-\kappa z} & 0 \leq z << \leq d \\ Fe^{ikz} & z > d \end{cases} \tag{1.2}$$

The wave numbers are given by $k = \sqrt{2mE/\hbar^2}$ and $\kappa = \sqrt{2m(V_0 - E)/\hbar^2}$. This equation can be simplified by using the fact that the wave function is continuously differentiable as detailed in ref. [24]. The work function Φ is given by the difference between the vacuum level V_0 and the Fermi level E_F plus an eventually applied bias $-eV$ for $|eV| \ll V_0$ for both electrodes on either side of the barrier. Assuming Φ to be equal in both electrodes, we eventually find the transmission coefficient T given by

$$T = \frac{I(z)}{I(0)} = \exp(-2\kappa z) \tag{1.3}$$

with $\kappa = 5.1\sqrt{\Phi}\ \mathrm{nm}^{-1} \approx 11.4\ \mathrm{nm}^{-1}$ for typical metals with work functions around 5 eV. This leads to a decrease in current by approximately one order of magnitude per 0.1 nm distance and therefore to the outstanding topographical resolution in the tunneling regime. A better understanding of the voltage dependence in STM experiments can be gained through the Bardeen model for tunneling, which ultimately yields [23]

$$I \propto \int_0^{eV} \rho_T(E_F - eV + \epsilon)\rho_S(E_F - \epsilon)d\epsilon \tag{1.4}$$

where ρ_T and ρ_S denote the density of states (DOS) in tip and sample. Hence, the current is dependent on the integrated joint DOS between tip and sample. The differential conductance as a function of the applied voltage can be used to extract the energy dependent DOS, and is typically probed using a lock-in technique. When probing for discrete spin excitations, one ideally has a constant DOS to purely observe the effect of the excitation.

1.1.2 Spin-dependent transport

Direct observation of sub-nanometer-scale magnetic structures became possible with the introduction of SP-STM in 1990 [22]. An excellent review is given for example in ref. [25]. Experiments typically rely on ferromagnetic (FM) or antiferromagnetic (AFM) ordering at the apex of the STM tip leading to a finite spin polarization of the electrons close to the Fermi level. A common definition of the degree of spin polarization η of the tunneling current is given by

$$\eta = \frac{N_\uparrow - N_\downarrow}{N_\uparrow + N_\downarrow} \tag{1.5}$$

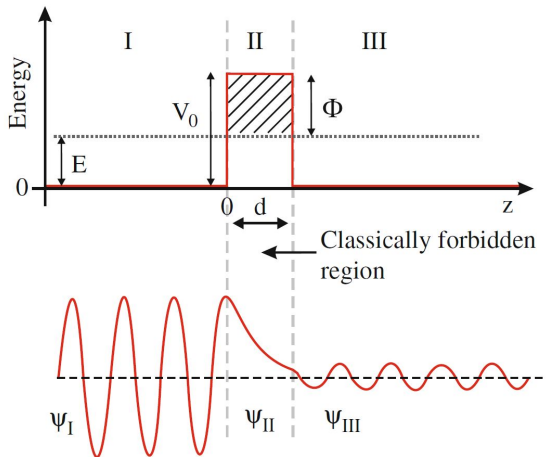

Figure 1.2: **Tunneling across a 1-dim. barrier**: The upper graph shows a one-dimensional energy landscape, where two electrodes are separated by a potential barrier. The lower graph shows a schematic of an electron wave function entering from the left side and performing classically forbidden sub-barrier tunneling [24].

where $N_\uparrow$ and $N_\downarrow$ denote the available tunneling electrons with spin alignments parallel and antiparallel w.r.t. some axis. Within the Landau transport theory framework, the total conductance can be decomposed into two fully spin-polarized transport eigenchannels, and, for a fully spin polarized current, a point contact of $G_0/2$ has been observed in single magnetic adatoms [26]. The relative change in resistance between parallel and anti-parallel alignment of two electrons is called tunnel-magnetoresistance. Typical materials for bulk magnetic tips include Fe (FM) and Cr (AFM). A possible advantage of bulk magnetic tips can be the relatively stable magnetic orientation, allowing for changes in an externally applied magnetic field without changing the magnetic properties of the tip. As part of this work, we published research on the fabrication and characterization of MnNi (AFM) tips [27] displayed in fig. 1.3. For all subsequent work, however, the magnetic tips were created by using a non-magnetic tip and picking up individual Fe atoms from the surface. For typical ESR experiments at magnetic fields $\geq$ 100 mT, picking up a handful of atoms often suffices to create an ESR-active STM tip. As described in detail later, we were also able to create tips with a stable magnetic orientation even in the absence of an external field by picking up large numbers of $\geq$ 30 Fe atoms. This likely leads to superparamagnetic clusters of FM coupled Fe atoms, likely in combination with a distinct shape anisotropy. Most tips, however, required a magnetic field to show sufficient spin polarization. Advantages of such tips can be that the axis of spin polarization can follow the external field to some degree, the easy preparation of such tips given the samples used throughout this work where small amounts of Fe are co-deposited, as well as facile re-preparation in case of an accidental tip indent.

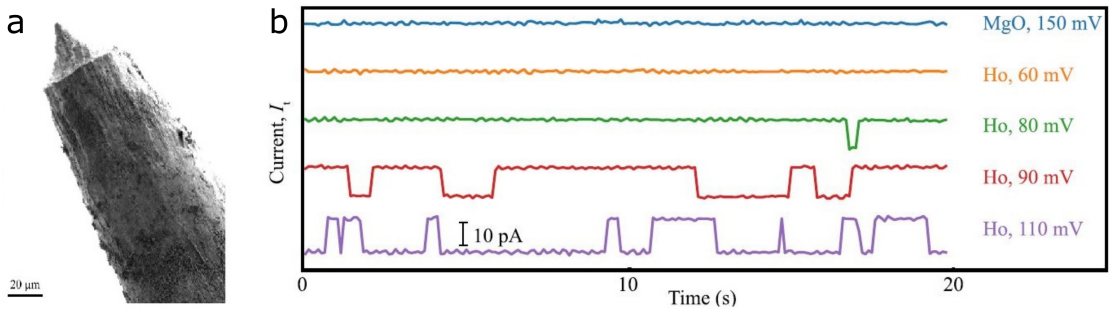

Figure 1.3: **Spin polarized MnNi tip**: **a**, Scanning electron microscopy image showing the apex of an MnNi STM tip. **b**, Magnetic two-state switching measured on a Ho adatom deposited on an ultrathin MgO film on Ag(100). The magnetic contrast in this case is approx. 10%. Larger applied voltages allow access to more efficient magnetization reversal pathways and therefore increase the switching rate (I = 100 pA, T = 4.7 K, zero external field) [27].

1.1.3 Spin-flip spectroscopy

Spin-flip spectroscopy is one type of inelastic tunneling spectroscopy (IETS). In IETS, tunneling electrons are used to probe usually discrete excitations in a system under investigation. The name derives from the fact that the electrons inelastically exchange energy with the system. If the energy of the tunneling electrons exceeds the energy of the excitation, a new transport channel opens up and the conductance increases. When measuring the current as a function of voltage, this shows up as a broadened kink in the conductance spectra, or equally as a broadened step in the differential conductance, at the point where the energy of the tunneling electrons is equal to the energy of the excitation under investigation. The broadening can result from effects such as temperature broadening, bias-line noise or life-time broadening. IETS applied to spin excitations is often referred to as spin-flip spectroscopy and was first demonstrated in single atoms on surfaces in 2004 [12]. The defining characteristic of spin-flip spectroscopy is the alteration of energy and angular momentum of the surface spin. Typically the tunneling electrons and surface spin exchange both energy and angular momentum, although induced tunneling of magnetization without momentum exchange has also been observed in Fe/MgO [28] and will also be discussed in detail later for Ho and Dy/MgO.

Spins on surfaces can be described within the framework of open quantum systems. An excellent introduction to the theory of open quantum systems and quantum dynamics therein can be found in Breuer *et al.* [29]. The Hamiltonian of the surface spin system can be assumed to be of the form

$$H = H_S + H_B + H_I \tag{1.6}$$

H_S denotes the free Hamilton of the spin system and includes terms such as the spin-orbit coupling, crystal field and Zeeman energy. For coupled spin systems, H_S also includes the spin-spin interaction such that the total spin system can be described. H_B and H_I describe

the bath and its interaction with the spin system. This interaction can be given for example by coupling to phonons and environmental spins. Within the very similar context of molecular magnets, a detailed description of different scattering mechanisms is given for example in Gatteschi *et al.* [30]. A somewhat particular effect observed in spins on surfaces and ultrathin insulators is the coupling to itinerant electrons of the underlying metallic substrate. While transition metal adatoms on metal surfaces often show a strong many-body-interaction and no discrete spin excitation, for Fe/MgO/Ag(100) it has been shown that the coupling gets reduced for increasing insulating film thickness allowing for extended single spin lifetimes in individual Fe spins [28].

The so far mentioned spin-bath interactions drive the spin system towards thermal equilibrium. However, one also needs to consider the influence of the measurement process. While in STM and ESR-STM, the tunneling electrons and microwave radiation can drive the spin out of equilibrium, in x-ray absorption measurements x-ray induced secondary electrons have a similar effect, as will be demonstrated later. Nonetheless, all results in this work can be described within the weak coupling limit (Born approximation), *i.e.*, where the density matrix of spin and bath are given by a tensor product [29]

$$\rho(t) \approx \rho_{\mathrm{S}}(t) \otimes \rho_{\mathrm{B}} \tag{1.7}$$

Treating the system within the strong coupling limit would become necessary for example in the presence of a significant Kondo interaction, where a perturbative approach for spins on surfaces has been developed and applied to successfully approximate this regime [31]. In this subsection we describe the differential conductance across surface spin systems when they are in thermal equilibrium with the environment, whereas more complex phenomena will be described afterwards.

Following the excellent reviews by M. Ternes [31, 32], the differential conductance in the weak coupling and thermal equilibrium limit, where the internal dynamic dominates over the measurement induced dynamics, can be written as

$$\frac{dI}{dV}(V) = \frac{G}{e^2} \sum_{i,f} p_i \Big(P^{\mathrm{ts}}_{fi} \theta(eV - \epsilon_{fi}) - P^{\mathrm{st}}_{fi} \theta(-eV - \epsilon_{fi}) \Big) \tag{1.8}$$

where G denotes the set-point conductance, p_i the occupation of state i following the Boltzmann distribution, P^{ts}_{fi} the transition matrix element for electrons tunneling from tip to sample, ϵ_{fi} the energy difference between initial and final state, and θ the temperature broadened step function

$$\theta(x) = \frac{1 + (x-1)\exp(x)}{\big(1 + \exp(x)\big)^2} \tag{1.9}$$

using $x = \epsilon / (k_{\mathrm{B}} T_{\mathrm{eff}})$. Neglecting the spin polarization, this will lead to a constant differential conductance with broadened step-like increases whenever the applied voltage becomes equal to a transition energy ϵ_{fi} for which a finite transition matrix element exists, with the step

height being proportional to the transition matrix element.

The interaction Hamiltonian H_I between surface spin and tunneling electron spin can be described as

$$H_\mathrm{I} = \frac{1}{2}\hat{\sigma}\hat{S} = \frac{1}{4}\hat{\sigma}_+\hat{S}_- + \frac{1}{4}\hat{\sigma}_-\hat{S}_+ + \frac{1}{2}\hat{\sigma}_\mathrm{z}\hat{S}_\mathrm{z} \tag{1.10}$$

Here the spin operators are defined as

$$\langle\uparrow|\hat{\sigma}_+|\downarrow\rangle = +1 \tag{1.11}$$

$$\langle\downarrow|\hat{\sigma}_-|\uparrow\rangle = +1 \tag{1.12}$$

$$\langle\uparrow|\hat{\sigma}_\mathrm{z}|\uparrow\rangle = +1/2 \tag{1.13}$$

$$\langle\downarrow|\hat{\sigma}_\mathrm{z}|\downarrow\rangle = -1/2 \tag{1.14}$$

Heuristically taking the spin polarization of the electrodes into account [28, 32], we can write the transition matrix elements combined with the spin dependent DOS as

$$\begin{aligned} P^{nm}_{fi}/P^{nm}_{fi,0} = &\|\langle f|\frac{1}{4}\hat{S}_-|i\rangle\|^2\Phi^n_\downarrow\Phi^m_\uparrow + \\ &\|\langle f|\frac{1}{4}\hat{S}_+|i\rangle\|^2\Phi^n_\uparrow\Phi^m_\downarrow + \\ &\|\langle f|\frac{1}{2}\hat{S}_\mathrm{z}|i\rangle\|^2(\Phi^m_\uparrow\Phi^n_\uparrow + \Phi^m_\downarrow\Phi^n_\downarrow) \end{aligned} \tag{1.15}$$

where $\Phi^m_\uparrow$ and $\Phi^m_\downarrow$ denote the relative spin polarized DOS of electrode m for spins parallel and antiparallel w.r.t. the axis of quantization of the surface spin. Throughout this work, we have $\Phi^t_\downarrow = 1+\eta$, $\Phi^t_\uparrow = 1-\eta$ and a non-polarized substrate. This introduced an asymmetry in bias of the differential conductance spectra whereby the step heights at positive and negative bias increase or decrease respectively, depending on the sign and amplitude of η. This leads to the well known result that the spin-polarization in vicinity of the Fermi surface can be probed using spin-flip spectroscopy in a rapid and facile manner [25, 32, 33]. Throughout this work we have used this fact to greatly accelerate experiments by testing tips for sufficient spin polarization before attempting ESR measurements. The normalization constant $P^{nm}_{fi,0}$ is chosen such that every electron taking a spin dependent transport channel must necessarily interact with the surface spin either elastically or inelastically and for a spin-1/2 system is given by $P^{nm}_{fi,0} = 1/16 + 1/32$ for non-polarized electrodes, although varying approaches have been described in literature [28, 31, 34].

1.1.4 Rate equation model

When the applied current becomes large enough such that the scattering with tunneling electrons happens significantly more frequent compared to scattering with intrinsic scattering sources, the surface spin system gets driven out of thermal equilibrium. For a non-polarized current this typically leads to a more uniform occupation of states, as demonstrated for

example in ref. [34]. For a spin polarized current, depending on the sign of the bias, the electric current preferably adds or removes angular momentum from the surface spin, leading to an either more or less polarized spin compared to the case of a non-polarized current. The resulting differential conductance spectra show additional characteristic peaks and dips rather than simple steps. In general, understanding the interaction between surface spins and tunneling electrons will be helpful to understand the results described in this work, which is why it will be discussed in detail in the following.

Following refs.[31, 34], the current can be written as

$$I(V,t) = G_{\mathrm{SD}} \sum_{i,j} \left(\Gamma^{\mathrm{st}}_{ji}(V) - \Gamma^{\mathrm{ts}}_{ji}(V) \right) p_i(V,t) + G_{\mathrm{SI}} V \tag{1.16}$$

where $\Gamma^{\mathrm{st}}_{ji}(V)$ denotes the voltage dependent transition rate from state i to state j induced by electrons tunneling from tip t to sample s, and G_{SD} and G_{SI} the spin dependent and spin independent contributions to the conductance respectively. The occupation of the different quantum states is calculated via the Pauli master rate equation

$$\frac{dp_i}{dt} = \sum_j \left(\Gamma_{ij} p_j - \Gamma_{ji} p_i \right) \tag{1.17}$$

In the following we will assume a spin-1/2 system in the steady state limit. For such a two-level system (TLS) the relative occupations are given by $p_1 = \Gamma_{12}/(\Gamma_{12}+\Gamma_{21})$ and $p_2 = 1 - p_1$. Following refs. [28, 31, 34], the transition rates can be written as

$$\Gamma^{\mathrm{st}}_{ji} = \frac{G_{\mathrm{SD}}}{e^2} P^{\mathrm{st}}_{ji} \int f(E) \left(1 - f(E + eV + \epsilon_{ji}) \right) dE = \frac{G_{\mathrm{SD}}}{e^2} P^{\mathrm{st}}_{ji} g(\epsilon_{ji}, V) \tag{1.18}$$

$$\Gamma^{\mathrm{st}}_{ji} = \frac{G_{\mathrm{SD}}}{e^2} P^{\mathrm{ts}}_{ji} g(\epsilon_{ji}, -V) \tag{1.19}$$

$$\Gamma^{\mathrm{ss}}_{ji} = \frac{G^{\mathrm{ss}}_{\mathrm{SD}}}{e^2} P^{\mathrm{ss}}_{ji} g(\epsilon_{ji}, 0) \tag{1.20}$$

$$\Gamma^{\mathrm{tt}}_{ji} = \frac{G^{\mathrm{tt}}_{\mathrm{SD}}}{e^2} P^{\mathrm{tt}}_{ji} g(\epsilon_{ji}, 0) \tag{1.21}$$

where $f(E)$ is the Fermi distribution and the Fermi integral function g is given by

$$g(\epsilon_{ji}, V) = \frac{\epsilon_{ji} - eV}{\exp((\epsilon_{ji} - eV)/(k_{\mathrm{B}} T)) - 1} \tag{1.22}$$

The sample-sample scattering term drives the sample towards thermal equilibrium and is also present in absence of the STM tip. By assuming $G^{\mathrm{ss}}_{\mathrm{SD}}$ to be equal to the point contact conductance, one can estimate the intrinsic spin lifetime. This lifetime was shown to decrease as a function of insulating film thickness for Fe/MgO [28]. Similarly, by approximating $G^{\mathrm{tt}}_{\mathrm{SD}} G^{\mathrm{ss}}_{\mathrm{SD}} \approx G^2_{\mathrm{SD}}$, it has been shown that due to the quadratic setpoint dependence, for small tip-sample distances this term dominates the scattering [28]. Note that since the tip is spin

polarized, a higher polarization helps to suppress spin flip events in tip-tip scattering due to $P^{\mathrm{tt}}_{ji} \propto (1-\eta^2)$, as can be derived from eq. 1.15, which presents another benefit of using highly spin-polarized tips in ESR-STM. The tip-sample and sample-tip scattering terms are linearly proportional to the spin-dependent part of the setpoint condutance. Therefore, if these terms dominate, at constant voltage one would expect a linear increase of spin scattering events as a function of current, in agreement with experimental data as we will show later. Plugging all the results into eq. 1.16 yields

$$\begin{aligned} I(V) =& G_{\mathrm{SI}} V + \frac{G_{\mathrm{SD}}}{e(\Gamma_{12}(V)+\Gamma_{21}(V))} \times \\ & \Bigg(\Gamma_{21}(V) \Big(g(\epsilon,V)\frac{1+\eta}{16P_0} P^{\mathrm{st}}_{12} - g(\epsilon,-V)\frac{1-\eta}{16P_0} P^{\mathrm{ts}}_{12} + g(0,V)\frac{1}{32P_0} P^{\mathrm{st}}_{11} - g(0,-V)\frac{1}{32P_0} P^{\mathrm{ts}}_{11} \Big) \\ & \Gamma_{12}(V) \Big(g(-\epsilon,V)\frac{1-\eta}{16P_0} P^{\mathrm{st}}_{21} - g(-\epsilon,-V)\frac{1+\eta}{16P_0} P^{\mathrm{ts}}_{21} + g(0,V)\frac{1}{32P_0} P^{\mathrm{st}}_{22} - g(0,-V)\frac{1}{32P_0} P^{\mathrm{ts}}_{22} \Big) \Bigg) \end{aligned} \tag{1.23}$$

The voltage dependent transition rates are given by

$$\begin{aligned} \Gamma_{12} =& \frac{1}{e^2} \Big(G_{\mathrm{SD}} g(\epsilon,V)\frac{1+\eta}{16P_0} + G_{\mathrm{SD}} g(\epsilon,-V)\frac{1-\eta}{16P_0} + \\ & \frac{G^2_{\mathrm{SD}}}{G^{\mathrm{ss}}_{\mathrm{SD}}} g(\epsilon,0)\frac{1-\eta^2}{32P_0} + G^{\mathrm{ss}}_{\mathrm{SD}} g(\epsilon,0)\frac{1}{32P_0} \Big) \\ \Gamma_{21} =& \frac{1}{e^2} \Big(G_{\mathrm{SD}} g(-\epsilon,V)\frac{1-\eta}{16P_0} + G_{\mathrm{SD}} g(-\epsilon,-V)\frac{1+\eta}{16P_0} + \\ & \frac{G^2_{\mathrm{SD}}}{G^{\mathrm{ss}}_{\mathrm{SD}}} g(-\epsilon,0)\frac{1-\eta^2}{32P_0} + G^{\mathrm{ss}}_{\mathrm{SD}} g(-\epsilon,0)\frac{1}{32P_0} \Big) \end{aligned} \tag{1.24}$$

Hereby ϵ represents the (negative) energy difference between states 2 and 1. Note that these rate equations consider purely electronic scattering, which has proven successful to explain the intrinsic lifetime of Fe/MgO [28]. An approach to include spin-phonon coupling will be discussed later for the case of Ho/MgO. *A priori* unknown is the ratio between G_{SD} and G_{SI}. For the case of Fe/MgO, as well as the here presented case of FePc, we find $G \approx G_{\mathrm{SD}}$ and $G_{\mathrm{SI}} \approx 0$. In other words, all tunneling electrons take a spin dependent transport channel and have a finite probability to interact with the surface spin. However, as will be shown later for Dy/MgO, this is not necessarily the case, e.g., due to a weak interaction between itinerant tunneling electrons close to the Fermi level and the angular momentum localized exclusively or predominantly in $4f$ orbitals. A comparison between theoretical and experimental data for FePc in fig. 1.4 shows excellent agreement. Hereby, we used the experimentally determined point contact conductance of $G^{\mathrm{ss}}_{\mathrm{SD}} \approx G^{\mathrm{ss}} = 0.5$ nA/mV.

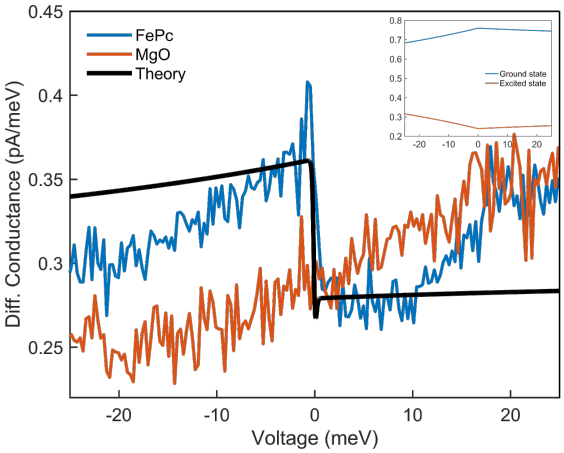

Figure 1.4: **Spin-flip spectroscopy of FePc**: The differential conductance measurement shows a single step at zero bias, corresponding to excitations between the two magnetic states of the spin-1/2 system FePc/MgO. The asymmetry is induced by the external field lifting the degeneracy in combination with a spin-polarized current. The theoretical curve is calculated using eq. 1.23. The deviation from experiment stems predominantly from a non-flat DOS of the tip which leads to an almost linear slope not captured by the model, as can be seen by comparison with the reference spectra on MgO. Inset shows the occupation of the two states as a function of the applied bias. The incoherent scattering with the tunneling electrons drives the system out of thermal equilibrium found at zero bias (I = 12 pA, B = 0.6 T, T = 0.7 K; fit parameters $\eta = 0.7$, $G_{\mathrm{SI}} = 0$).

1.1.5 ESR-STM

ESR-STM combines the energy resolution of spin resonance experiments with the STM's capability of imaging and manipulation of individual spins on surfaces. This opens up a whole new range of physical phenomena for investigation. In their pioneering work, S. Baumann *et al.* [7] carried out ESR experiments on individual Fe atoms on two monolayers of MgO deposited on Ag(100). Apart from being the first ESR-STM work in the sense of how we commonly understand it today, this marks the first time that Rabi rates Ω and coherence times T_2 have been measured in an STM. For this work, the authors used individual Fe adatoms on 2 ML of MgO grown on Ag(100). An external magnetic field with an out-of-plane component B_z of around 180 mT is used to induce a Zeeman splitting of the lowest lying doublet by around 25 GHz ($\approx 100\ \mu$eV). A schematic is shown in fig. 1.5. In addition to the DC voltage, a constant RF voltage is applied to the junction and the frequency is swept. Once the RF frequency matches the energy level splitting between the two opposing spin states, transitions between them are induced. The resulting change in average occupation of ground and excited state can be read out using an SP tip through tunnel magnetoresistance. The signal was fitted using a Lorentzian function and showed amplitudes below 100 fA and linewidths as low as 3.6 Mhz. From fitting the lineshapes using the steady state solution to the Bloch equation:

$$I = I_0 + I_p \frac{\Omega^2 T_1 T_2}{1 + 4\pi^2 (f - f_0)^2 T_2^2 + \Omega^2 T_1 T_2} \tag{1.25}$$

the authors estimate an approximate intrinsic coherence time of $T_2 = 250 \pm 50$ ns and a Rabi flop rate of 1.2 μ s for coherent reversal of the magnetization at an RF voltage of 8 mV and a current of 0.56 pA.

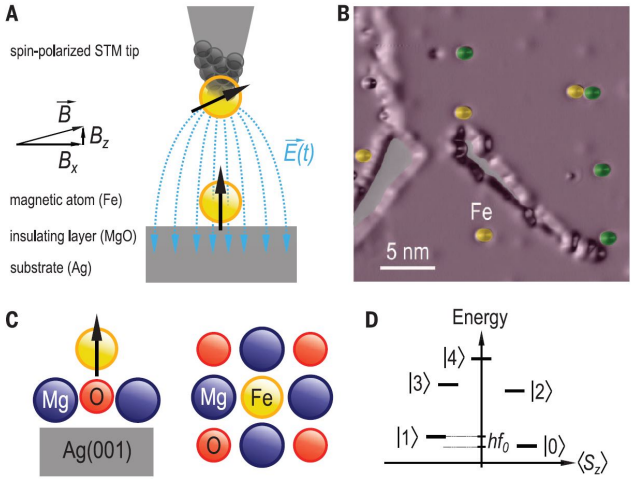

Figure 1.5: **Schematic of ESR-STM applied to Fe/MgO**: **a**, The time dependent voltage leads to a time dependent electric field sensed by the adatom. **b**, Topographic image of Fe/MgO (I = 10 pA, V_{DC} = 100 mV, T = 1.2 K). **c**, Schematic of Fe being adsorbed atop of O in C_{4v} symmetry. **d**, Energy level diagram. Transitions within the ground state doublet occur when the applied radio frequency matches the energy level splitting [7]

In order for ESR-STM to work, the time dependent RF voltage applied to the junction must induce a time dependent magnetic interaction leading to a finite transition matrix element $\langle f|dH/dt|i\rangle$ between initial spin state $|i\rangle$ and final spin state $|f\rangle$, whereby H describes the static properties of the free spin. S. Baumann *et al.* propose a piezoelectric effect, whereby the applied RF voltage slightly displaces the Fe adatom perpendicular to the surface in a time dependent manner. This time dependent displacement leads to a time dependent variation of the crystal field. The transition matrix elements being increased by an in-plane magnetic field [35], this leads to a sufficient transition matrix element and coherent reversal of magnetization can occur at resonance frequency. Later experimental work often additionally considers displacement induced time dependent magnetic interaction with the tip field as proposed by J. L. Lado *et al.* [35] to contribute. Recent work investigates the two most well known systems, Ti and Fe on MgO/Ag(100), in detail experimentally with the goal to determine the mechanisms at work [36]. The authors conclude that the tip interaction drives ESR for the case of the dipolar transition in the spin-1/2 system Ti, whereas the crystal field is dominating in the case of the more complex spin-2 system Fe.

In subsequent ESR-STM work making use of the increased energy resolution, dipolar coupling between individual adatoms was measured for the first time, showing the pure dipolar

coupling between pairs of Fe adatoms at distances larger than approx. 1 nm, with measured energy level splittings as low as 20 MHz (80 neV) [15]. Later work used this mechanism to map out the angular dependence of the dipolar coupling [37] and to remotely sense and thereby further confirm the magnetic stability of Ho [38]. Additional ESR-STM work in this category shows among other things hyperfine (HF) interaction and its isotope and environment dependence on the level of single adatoms and dimers [16], and electron nuclear double resonance [39].

Seminal work by P. Willke *et al.* [40] shows the influence of different measurement parameters on ESR-STM measurements. While it was demonstrated that the signal strength increases monotonically with the RF voltage (up to around 100 mV where, depending on the tip, the signal amplitude eventually starts to saturate [36]) and that even at 4 K a signal can be measured, some limitations of the technique have been displayed as well. The coherence time T_2 depends linearly on the tunneling current, meaning that each electron carries a certain probability (approx. 2/3 in the case of Fe/MgO) for destroying the phase coherence. This results in the phase coherence time being relatively short (max. 40 ns at 1 pA in this study) independent of the system under examination as long as this scattering mechanism is present at a significant probability, although recent work on TiH [8] and our own work show that the coherence time in Hahn echo measurements can be several times longer. Equally, just like we observe that many SP-tips can not drive ESR, those that do drive ESR don't lead to equal measurements. For different tips but equal measurement parameters, the authors observe the coherence time varying by up to a factor of 10. This means that while ESR-STM measurements in general are reproducible, the precise details are hard to reproduce exactly, due to the inability to precisely engineer the magnetic microtip.

Additional research focuses more on the quantum coherent phenomena now accessible through ESR-STM. Y. Bae *et al.* [41] have recently demonstrated enhanced quantum coherence in a singlet-triplet transition. In two coupled spin-1/2 systems of unequal moment, they used the stray field of the tip to tune one of the singlet-triplet transitions into a regime where its energy level splitting at first order does not depend on fluctuating magnetic fields. Consequently, they find the phase coherence time increased by roughly a factor two. Most recently, coherent manipulation of single adatom spins has been demonstrated for the first time [8]. Notably, they find Rabi flop rates as fast as 5 MHz and phase coherence times of up to $T_2^{\text{Rabi}} \approx 40$ ns and $T_2^{\text{Hahn}} \approx 190$ ns on TiH adatoms. Finally, in combination with pump-probe measurements, the research group of A. F. Otte has recently shown coherent population transfer between coupled spin-1/2 systems [42].

Some of the key technical ingredients for modern ESR-STM experiments include:

- Controllable magnetic field

- Low temperature to provide for sufficient spin polarization of the surface spin at the desired energy level splitting

- RF transmission at high enough frequencies compared to the measurement temperature, and ideally broadband transmission to allow for frequency sweeps

- Low noise to prevent exceedingly large tip-sample-distance variations leading to a broad linewidths [40]

The third point represents the main technical breakthrough allowing for ESR-STM the way it is carried out today. While RF-STM has a long history, typical experiments were carried out at frequencies in the MHz to low GHz range. At such energy level splittings, the difference in thermal occupation between ground and excited spin state is too low for detecting an ESR signal the way it is now commonly done. The first ESR-STM work represents the first STM work where well controlled RF-STM experiments were carried out at frequencies up to 30 GHz by compensating frequency-dependent losses in the transfer function. This was made possible by a novel technique allowing for precisely determining the RF voltage in the STM junction across a large frequency range. In their seminal work, W. Paul *et al.* [43] use the broadening of inelastic excitations in differential conductance measurements by an additionally applied RF voltage, see fig. 1.6. The obtained lineshape can be fitted and gives the precise RF voltage in the junction. The difference in applied compared to measured RF voltage gives the transfer function at one specific frequency and one specific RF power. Instead of carrying this procedure out for every frequency, which would take unfeasible amounts of time, they instead apply a DC voltage equal to the energy of the inelastic excitation. Assuming that the I-V-curve is linear above and below the inelastic excitation energy but of unequal slope, an additionally applied RF voltage leads to a rectified current linearly proportional to the RF voltage in the junction. This effect is similar to what is observed in a Schottky diode except that an additional DC voltage offset has to be applied. Knowing the precise RF voltage in the junction at one specific frequency, and knowing the specific rectified current it leads to, now allows to simply adjust the output level of the RF source at each other frequency until the same rectified current is obtained. This allows for very quick measurements of the transfer function and is the fundamental invention allowing for the majority of ESR-STM work carried out. Note that one does not necessarily require an inelastic excitation to gauge the RF voltage in the junction. In principle, any sufficiently strong nonlinearity can work. An alternative approach to sweeping the frequency is sweeping the external field, as was first implemented in ESR-STM as part of this work. Similarly, the effective field can be swept by varying the tip-spin distance, which will be discussed later in detail. In the following subsections we will derive the theoretical formulas used to explain the signal measured in continuous-wave (CW) ESR and pulsed ESR experiments.

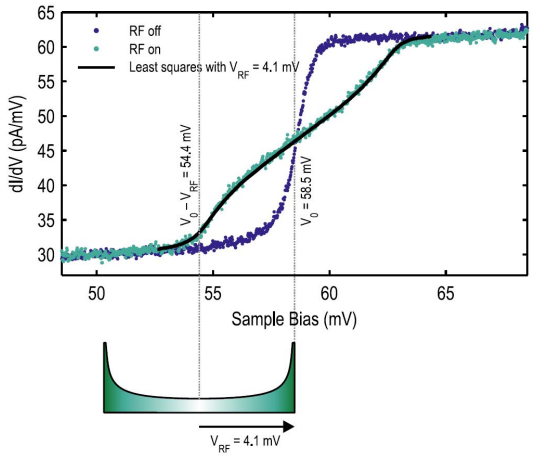

Figure 1.6: **Determining the RF voltage in an STM junction**: By measuring a non-linear dI/dV feature such as an inelastic excitation and comparing results with and without an applied RF voltage, the effective RF voltage in the STM junction can be determined. The curve with applied voltage is equal to the original curve convoluted by an arcsine function of width V_{RF}. Here, an inelastic spin excitation of Co/MgO with an energy of 58.5 meV is used. Upon application of V_{RF} = 4.1 mV, a significant change in the $dIdV$ spectra can be observed within approx. 54.4 and 62.6 meV [43].

1.1.6 Continuous wave ESR-STM

The single spins examined ESR-STM thus far are either transition metal based spin-1/2 systems (Ti, Cu, FePc) or spin-2 in the case of Fe. While the former naturally represent a TLS, Fe can for this purpose also be approximated as such, since the fist excited doublet lies ≈14 meV above the ground state doublet [44]. Thus, the Bloch equations will be used as a starting point to describe CW-ESR and pulsed ESR experiments. Excellent introductions to ESR in paramagnetic transition metal ions and semiconductor nanostructures can be found in refs. [45, 46]. The derivation of the formulas loosely follows ref. [41].

ESR-STM is based on the TMR. The current can be written as a combination of the spin dependent (SD) and spin independent (SI) currents. For simplicity, we consider the conductance of the tunneling junction $G_j = G \times (1 + a\langle S_{\mathrm{s}}(t)\rangle\langle S_{\mathrm{t}}\rangle)$ to be independent of the voltage range, and use a proportionality constant a to account for the TMR. We find

$$I = G \times (V_{\mathrm{DC}} + V_{\mathrm{RF}}(t))(1 + a\langle S_{\mathrm{s}}(t)\rangle\langle S_{\mathrm{t}}\rangle) \tag{1.26}$$

using the DC voltage V_{DC}, the RF voltage $V_{\mathrm{RF}}(t) = V_{\mathrm{RF}}\cos(\omega_{\mathrm{RF}}t + \varphi_{\mathrm{RF}})$, the time-dependent expectation value of the surface spin $\langle S_{\mathrm{s}}\rangle(t)$ and the expectation value of the tip spin $\langle S_{\mathrm{t}}\rangle$. The former is time dependent due to the dynamical evolution of the magnetization in a finite magnetic field and under application of an RF voltage, while the latter is assumed to represent a static magnet.

CW-ESR is carried out by sweeping either the frequency, the external magnetic field or the tip magnetic field. The experiments are carried out slowly with integration times per data point on the order of ~100 ms. This is far slower than other relevant time scales such as T_1, T_2 or the Rabi frequency Ω. Thus the Bloch equations in the steady state limit $d\langle S_s\rangle/dt = 0$ can be used. Using a rotating frame around the out-of-plane axis at frequency ω_{RF} one obtains [46]

$$\langle S_s^x\rangle = -S_s^o \frac{\Omega\Delta\omega T_2^2}{1+\Delta\omega^2 T_2^2+\Omega^2 T_1 T_2} \tag{1.27}$$

$$\langle S_s^y\rangle = S_s^o \frac{\Omega T_2}{1+\Delta\omega^2 T_2^2+\Omega^2 T_1 T_2} \tag{1.28}$$

$$\langle S_s^z\rangle = S_s^o \frac{1+\Delta\omega^2 T_2}{1+\Delta\omega^2 T_2^2+\Omega^2 T_1 T_2} \tag{1.29}$$

Hereby, $\Delta\omega = \omega_L - \omega_{RF}$ is the detuning between the Lamor frequency ω_L and the frequency of the rotating frame ω_{RF}. In this rotating frame we can write the tip spin as

$$\langle S_t^x\rangle = S_t^{xy}\cos(\omega_{RF}t+\varphi_t) \tag{1.30}$$

$$\langle S_t^y\rangle = S_t^{xy}\sin(\omega_{RF}t+\varphi_t) \tag{1.31}$$

$$\langle S_t^z\rangle = S_t^z \tag{1.32}$$

φ_t describes the initial in-plane alignment between tip and surface spin. Using eq. 1.26, we obtain

$$\begin{aligned} I = {} & G(V_{DC}+V_{RF}\cos(\omega_{RF}t+\varphi_{RF})) \\ & \Big(1+a\big(S_t^{xy}S_s^x\cos(\omega_{RF}t+\varphi_t)+S_t^{xy}S_s^y\sin(\omega_{RF}t+\varphi_t)+S_t^zS_s^z\big)\Big) \end{aligned} \tag{1.33}$$

The above equation contains several terms that are oscillating rapidly at angular frequency $\omega_{RF} \sim GHz$. They will be neglected, since they mostly average out at the integration time used (see above) and have negligible contributions. Furthermore, we can use the following geometric identities

$$\cos(\omega_{RF}t+\varphi_{RF})\cos(\omega_{RF}t+\varphi_t) = \frac{1}{2}\big(\cos(2\omega_{RF}t+\varphi_t+\varphi_{RF})+\cos(\varphi_{RF}+\varphi_t)\big) \tag{1.34}$$

$$\cos(\omega_{RF}t+\varphi_{RF})\sin(\omega_{RF}t+\varphi_t) = \frac{1}{2}\big(\sin(2\omega_{RF}t+\varphi_t+\varphi_{RF})+\sin(\varphi_{RF}+\varphi_t)\big) \tag{1.35}$$

Again, the rapidly oscillating terms can be neglected. Finally, one obtains

$$\begin{aligned} I = {} & GV_{DC}\Big(1+aS_t^zS_s^0\frac{1+\Delta\omega^2T_2}{1+\Delta\omega^2T_2^2+\Omega^2T_1T_2}\Big) \\ & + GV_{RF}\frac{a}{2}S_t^{xy}S_s^0\frac{\Omega T_2}{1+\Delta\omega^2T_2^2+\Omega^2T_1T_2}[\cos(\Delta\varphi)\Delta\omega T_2+\sin(\Delta\varphi)] \end{aligned} \tag{1.36}$$

Using phase $\Delta\varphi = \varphi_{RF}+\varphi_t$.

The measurements carried out here were done using amplitude modulation with a 50% duty cycle. For $V_{\mathrm{RF}} = 0$ and consequently $\Omega = 0$ the above equation simplifies to

$$I(V_{\mathrm{RF}} = 0) = GV_{\mathrm{DC}}(1 + aS_{\mathrm{t}}^{\mathrm{z}}S_{\mathrm{s}}^{0}) \tag{1.37}$$

The signal measured is

$$\begin{aligned}\Delta I &= I(V_{\mathrm{RF}} \neq 0) - I(V_{\mathrm{RF}} = 0) \\ &= \frac{GaS_{\mathrm{s}}^{0}\Omega T_2}{1 + \Delta\omega^2 T_2^2 + \Omega^2 T_1 T_2}\Big(V_{\mathrm{DC}}S_{\mathrm{t}}^{\mathrm{z}}\Omega T_1 + V_{\mathrm{RF}}^{0}S_{\mathrm{t}}^{\mathrm{xy}}\frac{1}{2}\big(\cos(\Delta\varphi)\Delta\omega T_2 + \sin(\Delta\varphi)\big)\Big)\end{aligned} \tag{1.38}$$

By adding a constant background $I_0(V_{\mathrm{DC}}, V_{\mathrm{RF}})$ due to the rectified current when the RF is on, the above eq. can conveniently be rewritten as the sum of the rectified, homodyne, and heterodyne contributions:

$$\begin{aligned}\Delta I = {} & I_0(V_{\mathrm{DC}}, V_{\mathrm{RF}}) \\ & + I_{\mathrm{DC}}^{\mathrm{Sat}}\frac{\Omega^2 T_1 T_2}{1 + 4\pi^2\Delta f^2 T_2^2 + \Omega^2 T_1 T_2} \\ & + I_{\mathrm{RF}}^{\mathrm{Sat}}\frac{\Omega T_2}{1 + 4\pi^2\Delta f^2 T_2^2 + \Omega^2 T_1 T_2}\big(2\pi\Delta f T_2\cos(\Delta\varphi) + \sin(\Delta\varphi)\big)\end{aligned} \tag{1.39}$$

$$I_{\mathrm{DC}}^{\mathrm{Sat}} = aGV_{\mathrm{DC}}S_{\mathrm{t}}^{\mathrm{z}}S_{\mathrm{s}}^{0} \tag{1.40}$$

$$I_{\mathrm{RF}}^{\mathrm{Sat}} = \frac{a}{2}GV_{\mathrm{RF}}S_{\mathrm{t}}^{\mathrm{xy}}S_{\mathrm{s}}^{0} \tag{1.41}$$

The first part of eq.1.39 carries no relevant information in our theoretical treatment. While the rectified current is also made up of an SD and an SI part, the I-V characteristics are typically rather linear within the voltage range used, and consequently the SD part of the rectified current carrying useful information will be extremely small. However, one may think of an experiment where strongly non-linear features are exploited to enhance the ESR readout. A good candidate would using the inelastic excitation of Ti, where an extremely pronounced nonlinear feature is found around ±80 meV.

The second part of eq.1.39 has often been referred to as the homodyne contribution in the context of ESR-STM. It is linearly proportional to the DC voltage and out-of-plane component of the STM tip spin. It predicts a Lorentzian lineshape which in practice is usually found for very low RF voltages. In the regime where this term dominates, the full width at half maximum (FWHM) is given by $\Gamma = \frac{1}{\pi T_2}\sqrt{1 + \Omega^2 T_1 T_2}$. The Rabi frequency can be rewritten as $\Omega = \kappa V_{\mathrm{RF}}$, since in our and previous work [8] it was found to be linearly proportional to the RF voltage, at least in the low-voltage regime [40]. Thus, in a regime where this term dominates, it is possible to extract the intrinsic T_2 by measuring the FWHM as a function of RF voltage and extrapolating to zero RF bias.

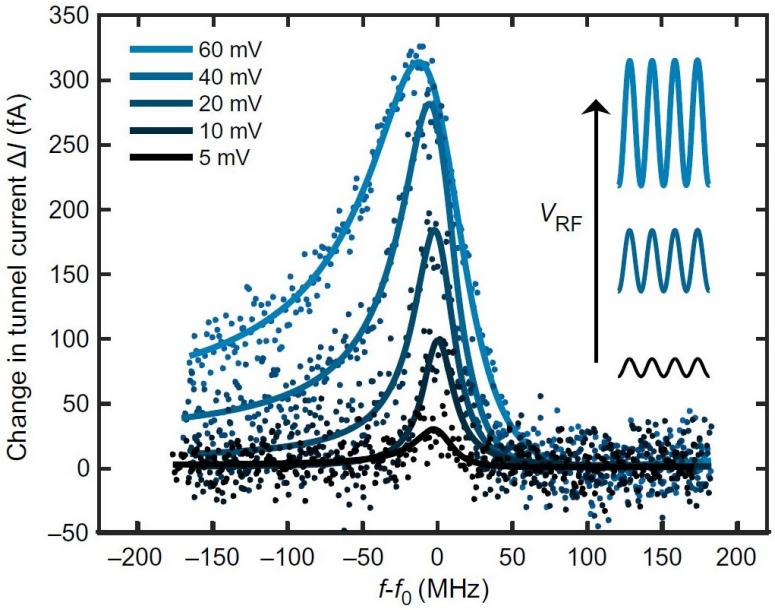

Figure 1.7: **RF voltage dependent CW-ESR**: The measurements carried out on Fe/MgO show a transition from a Lorentzian-like to a Fano-like lineshape (I = 11 pA, V_{DC} = 60 mV, $f_0 \approx$ 21 GHz, T = 1.2 K). Adapted from ref. [40], where a large parameter space in ESR-STM is explored.

The third part of eq.1.39 has often been referred to as the heterodyne contribution. It depends linearly on the RF voltage and out-of-plane component of the tip spin. The predicted lineshape is Fano-like. Figure 1.7 shows CW-ESR measurements of Fe/MgO. In agreement with the theory presented here, upon increased RF voltage, the lineshape transitions from Lorentzian-like to Fano-like. Upon a closer look, and in analogy to common ESR methods, this part of the equation can be further divided into a dispersive line and an absorption line. The dispersion line derives itself from $\langle S_t^x \rangle$ and depends linearly on Δf in the numerator. This leads to the characteristic asymmetry and broadening of the lineshape for larger RF voltages. The absorption line derives itself from $\langle S_t^y \rangle$ and is symmetric. Furthermore, if it was possible to engineer $\Delta\varphi$, the dispersive signal could be cancelled out and sharper linewidths would be achievable for high RF powers. However, in so far published measurements, large RF voltages always lead to a certain asymmetry and broadening. Dropping this third line in equation 1.39, the Lorentzian function from eq. 1.25 is recuperated. Still unclear is the role of $\Delta\varphi = \varphi_{RF} - \varphi_t$. Bae *et al.* measured a singlet-triplet transition with constant $\langle S_s^z \rangle$. The resulting signal stems purely from the homodyne part and was strongly antisymmetric, *i.e.*, dispersive, and indicating $\Delta\varphi \approx 0$.

Also note that many of the variables above are not independent. Exemplary, also mentioned above, it was demonstrated that tunneling electrons decrease T_1 and T_2 in Fe [28, 40], and later we demonstrate the same result for FePc. Thus, increasing V_{DC} or V_{RF} at constant setpoint

conductance G can lead to a decrease in T_2. For a non-linear conductance within the probed range, increasing V_{RF} leads to an increased rectified current and therefore a different setpoint if the measurements are carried out in closed feedback loop, which changes the effective tip field and therefore the resonance frequency. As mentioned before, the Rabi frequency Ω scales linearly in V_{RF}. For tips that couple to the surface spin through the dipolar field (as opposed to exchange interaction), changes in the setpoint conductance may shift some weight between $S_{\mathrm{t}}^{\mathrm{z}}$ and $S_{\mathrm{t}}^{\mathrm{xy}}$. Without going into further details, it can be said that obtaining extensive information based on the line shape can be difficult. However, simply the increased energy resolution by itself is often enough for novel and interesting research, and will be used throughout this work.

Simplified CW-ESR lineshape

Equation 1.39 demonstrates well the different contributions to the signal, but is still very complex. It can be simplified by introducing an angle θ between the tip spin and the out-of-plane axis, such the tip moments can be rewritten as $S_{\mathrm{t}}^{\mathrm{z}} = S_{\mathrm{t}}^{0}\cos(\theta)$ and $S_{\mathrm{t}}^{\mathrm{xy}} = S_{\mathrm{t}}^{0}\sin(\theta)$. Using $G \approx I_{\mathrm{Set}}/V_{\mathrm{DC}}$ and $\Delta\varphi \approx 0$ we find

$$\begin{aligned}
\Delta I &= I_0 + I_{\mathrm{peak}}\frac{1+\alpha\delta(f)}{1+\delta^2(f)} && (1.42)\\
I_{\mathrm{peak}} &= I_{sat}\frac{\Omega^2 T_1 T_2}{1+\Omega^2 T_1 T_2} && (1.43)\\
I_{sat} &= aI_{\mathrm{Set}}S_{\mathrm{s}}^{0}S_{\mathrm{t}}^{0}\cos(\theta) && (1.44)\\
\alpha &= \frac{1}{\Omega T_1}\frac{V_{\mathrm{RF}}}{V_{\mathrm{DC}}}\tan(\theta)\sqrt{1+\Omega^2 T_1 T_2} && (1.45)\\
\delta(f) &= \frac{2\pi\Delta f T_2}{\sqrt{1+\Omega^2 T_1 T_2}} && (1.46)\\
\Omega &= \kappa V_{\mathrm{RF}} && (1.47)
\end{aligned}$$

Note that unlike what was written in some earlier literature, this is not a Fano lineshape. Consider the frequency dependent part derived in eq. 1.42 in comparison to a typical Fano lineshape:

$$\begin{aligned}
Here: \quad \frac{1+\alpha\delta(f)}{1+\delta^2(f)} &= \frac{1}{1+\delta^2(f)} + \frac{\alpha\delta(f)}{1+\delta^2(f)} && (1.48)\\
Fano: \frac{(q+\delta(f))^2}{1+\delta^2(f)} &= \underbrace{\frac{q^2}{1+\delta^2(f)}}_{\text{Lorentz.-like contrib.}} + \underbrace{\frac{2q\delta(f)}{1+\delta^2(f)}}_{\text{asym. Fano-like contrib.}} + \underbrace{\frac{\delta^2(f)}{1+\delta^2(f)}}_{\text{sym. Fano-like contrib.}} && (1.49)
\end{aligned}$$

The symmetric Fano-like contribution is not present in eq. 1.42, *i.e.*, there is no term that scales quadratically with Δf in the numerator. A similar argument was made in a recent publication [36], where the authors argue that the transformation proposed in ref. [41] to bring eq. 1.42 in

agreement with a Fano lineshape requires making parameters such as amplitude, linewidth or asymmetry depend on each other, which already implies that they are unequal, and is a result of the mathematical argument above.

1.1.7 Pulsed ESR-STM

As opposed to CW-ESR, in pulsed ESR we are interested in the dynamical state of the system and quantum coherent control thereof. To understand pulsed ESR-STM experiments, we loosely follow ref. [8] in deriving an approximate formula to explain the measured signal for a Rabi experiment. Approximate theoretical results for other types of pulsed experiments can be derived relatively easily based on the treatment of the Rabi experiment shown here. The Bloch equations for a spin-1/2 system in the laboratory frame for $T_1, T_2 \to \infty$ with an applied resonant RF voltage can be written as

$$\langle S_s^x \rangle = -\frac{1}{2}\sin(\Omega t)\sin(\omega_L t) \tag{1.50}$$

$$\langle S_s^y \rangle = \frac{1}{2}\sin(\Omega t)\cos(\omega_L t) \tag{1.51}$$

$$\langle S_s^z \rangle = -\frac{1}{2}\cos(\Omega t) \tag{1.52}$$

We drop all rapidly oscillating terms at frequencies equal or larger than $\omega_L - \Omega$. Note that the commonly used rotating wave approximation does not apply here due to the low Rabi frequencies ~ 100 MHz compared to the Lamor frequency ~ 10 GHz. Ultimately we obtain

$$I(t) = V_{DC}\big(G^{SI} - \frac{G^{SD}}{2}\langle S_t^z\rangle\cos(\Omega t)\big) + V_0\frac{G^{SD}}{4}\sin(\Omega t)\big(\langle S_t^x\rangle\sin(\phi_{RF}) + \langle S_t^y\rangle\cos(\phi_{RF})\big) \tag{1.53}$$

For a duty cycle of 50%, the measured signal is proportional to the difference in average current between periods with and without initial RF pulse. The average signal during an initial RF pulse is given by

$$\begin{aligned} I_1 &= \int_0^{\tau_1} I(t)\,dt \\ &= V_{DC}\big(G^{SI}\tau_1 + \frac{G^{SD}}{2\Omega}\langle S_t^z\rangle\sin(\Omega\tau_1)\big) + \frac{V_{RF}G^{SD}}{4\Omega}\cos(\Omega\tau_1)\big(\langle S_t^x\rangle\sin(\varphi_{RF}) + \langle S_t^y\rangle\cos(\varphi_{RF})\big) \end{aligned} \tag{1.54}$$

The state of the surface spin immediately after the RF pulse is equally altered. As in ref. [47], we heuristically calculate the signal using the prefactor $\exp(-t/T_1)$ and obtain

$$\begin{aligned} I_2 &= \int_{\tau_1}^{\tau_1+\tau_2} (I_{DC}^{SI} + I_{DC}^{SD}\exp(-t/T_1))\,dt \\ &= V_{DC}\big(G^{SI}\tau_2 - \frac{G^{SD}}{2}\langle S_t^z\rangle\cos(\Omega\tau)\,T_1(1-\exp(-\tau_2/T_1))\big) \end{aligned} \tag{1.55}$$

Ultimately we measure for a well chosen delay time $\tau_2 \gg T_1$ the following equation

$$\begin{aligned}\Delta I_{\mathrm{Rabi}} &= (I_1 + I_2)\Big|_{\mathrm{RF\ on}} - (I_1 + I_2)\Big|_{\mathrm{RF\ off}} \\ &= \frac{G^{\mathrm{SD}}}{2}\Big(V_{\mathrm{DC}}\langle S_z^t\rangle\Big(\frac{\sin(\Omega\tau_1)}{\Omega} + \cos(\Omega\tau_1)T_1\Big) \\ &\qquad + V_{\mathrm{RF}}\frac{\cos(\Omega\tau)}{2\Omega}\Big(\langle S_t^{\mathrm{x}}\rangle\sin(\varphi_{\mathrm{RF}}) + \langle S_t^{\mathrm{y}}\rangle\cos(\varphi_{\mathrm{RF}})\Big)\Big)\end{aligned} \tag{1.56}$$

Again, we find the readout to be a combination of homodyne and heterodyne (V_{DC} and V_{RF} dependent) detection. Their ratio is determined by the relative DC and RF voltage amplitudes as well as the orientation of the tip spin. In ref. [8] the authors estimate the latter by measuring the distance-dependent tip-field. Furthermore taking heuristically the coherence time T_2^* into account, we find

$$\Delta I_{\mathrm{Rabi}}^{\mathrm{eff}} = \Delta I_{\mathrm{Rabi}} e^{\tau/T_2^*} + \kappa_{\mathrm{rec}}\tau \tag{1.57}$$

with κ_{rec} describing the rectified current per unit of RF pulse length added on top of the signal. This formula is now in agreement with the Rabi measurements in ref. [8], see fig. 1.8, and our work shown later. The rectified current increases linearly with the pulse width, and in both works a linear slope was removed prior to displaying the data.

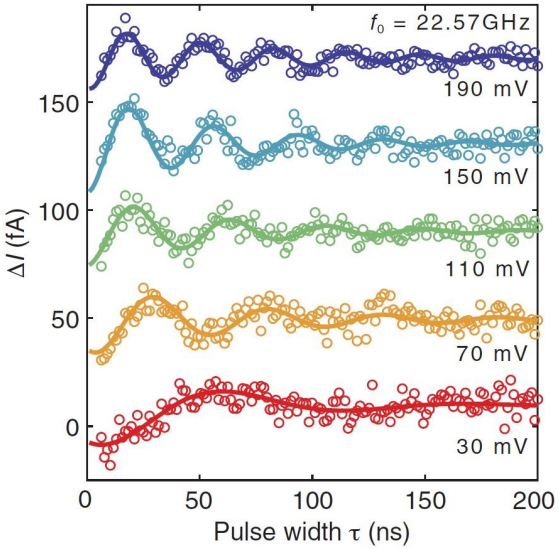

Figure 1.8: **Rabi oscillations in pulsed ESR-STM**: The spectra show Rabi oscillations measured on TiH/MgO, whereby the Rabi frequency grows monotonically with the applied RF voltage (I = 4 pA, V_{DC} = 60 mV, $f_0 \approx$ 22.57 GHz, T = 1.2 K) [8].

It should be highlighted again that this heuristic derivation relies on severe approximations and mostly serves the purpose of illustrating the detection scheme. While not carried out as part of this work, a better treatment could be obtained by numerically solving the full Bloch equation without the use of any approximations. Importantly, since the tunneling electrons strongly reduce both T_1 and T_2, they will both be non-stationary, and periods with applied RF

voltages will show shorter life and coherence times. Such a model should be relatively simple to implement using direct numerical integration and could be used to more meaningfully simulate Rabi, spin echo, and other measurements compared to this heuristic treatment.

1.2 Xray absorption spectroscopy

Apart from STM, X-ray based measurements have been the main tool to characterize magnetic properties of spins on surfaces in the sub-monolayer regime down to a coverage of 0.002 ML [48]. Measurements carried out by collaborators will be used later in this work to analyze Ho/MgO and therefore this technique is briefly explained here. A more detailed introduction can be found e.g. in ref. [49]. Figure 1.9 shows a schematic of the experiment.

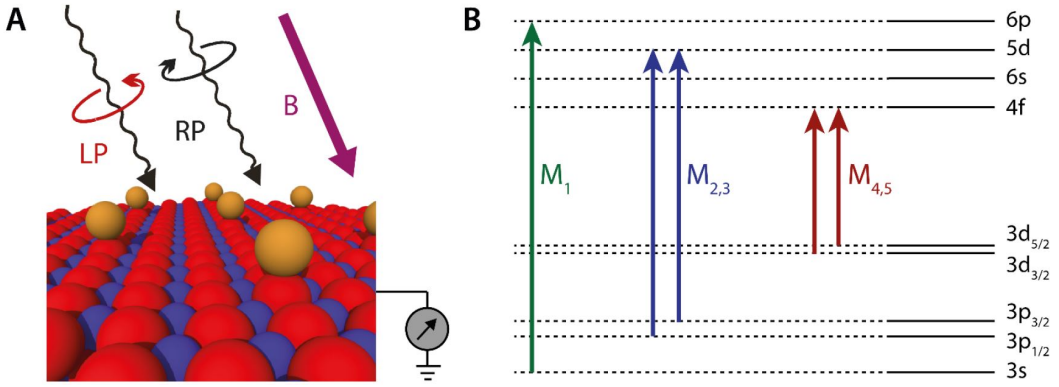

Figure 1.9: **Circularly polarized x-ray absorption in lanthanide adatoms**: **a,** Schematic of the X-ray absorption measurements. The incoming photons in the experiments presented here are circularly polarized, allowing to probe the magnetization. The magnetic field is parallel to the incoming photons. Their orientation can be normal to the surface (normal incidence) or, in the case of some of our measurements, at an angle of 60° with respect to the normal (grazing incidence). **b**, Schematic of the orbitals involved when measuring the M edge. The $M_{4,5}$ edges allow to probe the $4f$ orbital [50].

X-ray absorption measurements rely on photons of well defined energies absorbed by a target sample. Here we make use of the 5_5-edge in Ho, corresponding to transitions form the closed 3d to the open $4f$ orbitals. The absorption intensity is therefore proportional to the occupied 3d and unoccupied $4f$ states. Transition probabilities can be approximated by Fermi's golden rule and follow dipolar selection rules. Calculating final absorption spectra is typically done by using quantum many-body theory based open-source codes such as Quanty [51]. By circularly polarizing the photons, the absorption becomes dependent on the angular momentum of the initial and final electron state. If a net spin polarization of the sample exists, there will be a finite difference between the absorption spectra obtained by left and right polarized photons. Tracking this difference across time allows to analyze magnetization dynamics.

1.3 Sample growth and characterization

All experiments in this thesis were carried out on single adatoms or molecules deposited on thin films of MgO(100) on Ag(100). MgO is particularly suited due to the presence of a large electronic band gap already at ultrathin thicknesses required for tunneling measurements as well as the formation of large islands [52, 53]. It is also frequently used in traditional spintronic experiments [54]. Sample preparation was carried out exclusively in ultra high vacuum (UHV) at base pressures ideally in the range of 10^{-10} mbar.

The Ag(100) single crystals are commercially available. They are either clamped to sample holders using sapphire (in the case of the home built machine used at École polytechnique fédérale de Lausanne, Switzerland) or glued using silver epoxy (in the case of the Unisoku USM1300 machine used at the Center for Quantum Nanoscience, Institute for Basic Science IBS, Korea). The sample temperature is read out either through a thermocouple directly clamped to the sample (EPFL) or through a pyrometer (IBS). Cleaning the surface is very straight forward through cycles of sputtering and annealing, and very different parameters have been used throughout this thesis. For sputtering, the sample is bombarded with Ar^+ ions of energies typically around 1 keV, at a partial pressure of up to 3×10^{-5} mbar, leading to sputter currents of 1 to 10 μA for 20 to 40 minutes. Annealing was carried out using electron-beam heating at temperatures between 400 to 500 °C for 10 minutes. Typically 5 cycles were used to prepare a clean Ag(100) surface for samples that were exposed to air directly prior to the preparation procedure, and 2 to 3 cycles for repreparation of a sample coming from the STM head. At the end of the last cycle, rather than letting the sample cool down, the temperature was kept constant or at similarly high values and MgO growth was started.

MgO thin films were grown through physical vapour deposition. Mg was installed in a Knudsen cell and degased prior to the last sputtering/annealing cycles at temperatures 10 degrees higher than the final temperature used for deposition until the pressure fell back to roughly base pressure. Growth was carried out in an oxygen environment with partial pressures around 1×10^{-6} mbar. Often the onset of MgO growth came with a drop in pressure. Growth rates varied massively due to the very different parameters and instruments used, and could range anywhere from ≈ 1 to < 0.05 ML per minute. After deposition, post annealing was carried out, whereby the sample temperature is reduced slowly by approximately 100 to 200 degrees during typically 5 to 10 minutes. Afterwards, we let the sample cool down rapidly before transferring it to the STM for surface characterization. The film thickness of bare MgO can most easily be characterised in dI/dV or dz/dV measurements [55]. However, since all the STM work here also relied on having Fe on the surface, point contact measurements on top of Fe were used to determine the film thickness whenever possible. Using a voltage of 10 mV, point contact on top of Fe is reached at around 1 μS on 2 ML and decreases by roughly a factor 10 for each additional layer [28]. To scan on films thicker than 4 or 5 ML at reasonable currents ($\geq$ 1 pA) requires operating at voltages making MgO states beyond

the bandgap accessible. However, scanning at voltages of ≥ 1 V often removes adatoms in close proximity to the tip, which prevents working at film thicknesses larger than 4 or 5 ML. A point of ambiguity is the film thickness. In the pioneering work of [52], the authors assume the lowest commonly found film thickness to correspond to one monolayer. In ref. [28], the authors make the argument that this actually corresponds to two monolayers, while single layer MgO supposedly is extremely rare. Here, we will follow the later nomenclature.

The main difficulty in MgO preparation is to obtain low defect densities. These defects lead to slight variations of the properties of different adsorbed atoms and molecules despite being of the same species. Already in first ESR-STM work by S. Baumann *et al.* [7], the authors noted variations in the resonance frequency of up to 3 GHz, or approx. 15 percent, among 5 different Fe atoms studied, whereas relatively defect free MgO was used for our work on Dy/MgO. Since in the end the properties of individual adatoms are still relatively similar, and unlike in ensemble measurements one can simply skip low-quality MgO environments in STM, this issue is typically not given great importance. However, in practice this issue can still make it necessary to study larger numbers of adatoms or molecules in order to make scientifically reliable observations, and observations of certain rare phenomena are highly difficult or impossible. Exemplary, roughly 2 % of FePc molecules were supposed to show a split resonance in ESR-STM due to hyperfine (HF) interaction based on the typical occurance of ^{57}Fe. In our studies, the share of molecules showing a split resonance was several times higher, and with varying splitting magnitudes. This is likely a sign of coupling to defects and strongly complicates a scientifically reliable study of such rare phenomena.

Evaporation of adatoms was always carried out onto a cold sample, with surface temperatures ranging from a few Kelvin (EPFL) to > 35 Kelvin (IBS), using effusion cells. The cold temperature is necessary to prevent diffusion. At EPFL, the adatoms can be evaporated directly into the STM, albeit with opened thermal shutters. At IBS, using the Unisoku USM1300 machine, the sample has to be moved out of the cryostat for adatom evaporation. This requires pre-cooling the manipulator used to transfer the sample into the STM by putting it into thermal contact with the STM head inside the cryostat. In equilibrium, the STM head has a temperature of 30 to 35 K. Afterwards, the sample has to be removed from the cryostat using the partially cold manipulator for adatom evaporation. While neither for Fe or Ti adatoms this had a notably negative effect, this can be a problem for adatoms that start to diffuse at comparably low temperatures. It has been observed before that Ho adsorbed on top sites change to bridge sites at around 40 K [56], and in our work all of the as-deposited Dy adatoms on 2 ML MgO adsorbed on bridge sites. This made the development of an atom manipulation scheme necessary in order to study the top-site Dy adatoms on 2 ML. In contrast to adatoms, FePc was evaporated onto the room temperature sample and was found distributed across both Ag and MgO when analyzed using STM. Evaporation was carried out using commercially available FePc powder and a home built Knudsen cell mounted on a sample holder heated through direct current.

1.4 Multiplet calculations

Magnetism in single adatoms and molecules typically stems from partially filled d- or f-orbitals. The precise properties depend on the exact adatom-substrate combination under investigation. Since atoms on different surfaces interact differently with the environment, and additionally can have different charge states, it has been hard to predict *a priori* or even just explain *a posteriori* the precise properties of on-surface single spins. This makes in-depth experiments necessary. Nonetheless there exists a valuable body of theoretical work that allows to describe and to a certain degree predict magnetic properties of spins on surfaces.
In the most simple case, one can use toy Hamiltonians to describe the systems, such as [30]:

$$H = D \cdot S_z^2 + E \cdot (S_-^N + S_+^N) + g_z m_z \mu_B \cdot B_z \tag{1.58}$$

In this simple model, the D-term describes the uniaxial anisotropy, while the E-term describes the off-diagonal mixing term that mixes spin angular momentum states N quantum numbers apart and reflects the symmetry of the underlying substrate. Together, they represent the crystal field, *i.e.*, an externally induced anisotropy that favours certain spin orientations over others. S_- and S_+ represent the spin ladder operators. The last term represents the Zeeman energy with gyromagnetic ratio g, magnetic quantum number m, Bohr magneton μ_B and external magnetic field B.
This model is a simplification of the full set of Stevens operators which in principle allow to describe the crystal field in arbitrary symmetries [57]. The precise values of the Stevens parameters often are obtained through simple fitting of experimental data. However, due to the large amount of free parameters in combination with limited experimental information, this method is prone to overfitting. In the section on single atom magnets, we try to estimate the crystal field based on density functional theory (DFT) derived point charge models. Figuratively speaking, the surrounding charges perturb the orbital movement of the electrons through electrostatic repulsion and leads to preferred orbital and spin angular momentum configurations.
The toy Hamiltonian formulation in eq. 1.58 allows to deduce some of the ingredients necessary for achieving magnetic stability in SMMs and SAMs: The $D \cdot S_z$ term must be sufficiently large to prevent reversal of magnetization through thermal Orbach-processes, whereby the spin gets excited from lower to higher energy levels in a spin-ladder-like fashion until it can pass across the top of the energy barrier [58]. Equally, the off-diagonal terms of the Hamiltonian need to be weak or of specific symmetry such that within the lower lying multiplets, efficient scatterer assisted tunneling of magnetization in direct-phonon and two-phonon Raman processes, quantum tunneling of magnetization (QTM), and thermally assisted (TA) tunneling of magnetization are prevented. While half-integer spins are robust against single phonon relaxation due to Kramer's theorem, in the static picture presented above, one can not draw further conclusions on how to engineer more stable spins. However, it is possible to consider the effect of phonon induced lattice distortions on the crystal field parameters, *e.g.*, in the above model by replacing D and E by D(q) and E(q), with q being the phonon wave number. This in principle allows for calculations of the transition matrix elements between

different spin states $\langle i|dH(q)/dq|f\rangle$ between initial and final states i and f, and gives an idea on how effective different phonon induced relaxation pathways are [59]. Equally, one may try to reduce the phonon density of states in the relevant energy ranges to avoid phonon-assisted magnetization reversal.
A more complete picture is used in the chapter on SAMs. We consider the full Hamiltonian:

$$H = H_C + H_{LS} + H_{CF} + H_Z \tag{1.59}$$

Hereby H_C describes the Coulomb electron-electron interaction, H_{LS} describes the spin orbit coupling, H_{CF} the crystal field, and H_Z the Zeeman energy. The first two terms are obtained from atomic calculations based on the isolated atom using a Hartree-Fock approach. The third term represents the crystal field and is the chief distinction of magnetic atoms on surfaces compared to isolated atoms. Here we use a point-charge approach [57], whereby the effective charges and atomic positions are calculated in DFT. In order to fully describe Xray absorption spectra, one has to consider both ground and excited state individually, whereby in the latter case an electron is removed from the $3d$ and added to the $4f$ orbital in the case of the experimental Ho data presented as part of this thesis. These calculations are carried out using the Quanty code [51]. A significant role is played by the charge state of the $4f$ orbitals, which leads to specific angular momentum dependent orbital shapes, see fig. 1.10. Lanthanides in bulk configurations often lose a $4f$ electron compared to the gas phase, and dynamical charge fluctuations are also frequently observed [60]. For different charge states, different crystal field arrangements are required for magnetic stability. Qualitatively speaking, in lanthanides adsorbed on top-sites on MgO, the electrostatic repulsion of the negatively charged oxygen atom underneath the lanthanide leads to oblate $4f$ orbitals being more favourable. For $4f^9$ and $4f^{10}$ charge states (both are found in Dy/MgO, $4f^{10}$ also in Ho), this leads to a ground state of large angular momentum being more favourable. For top-site $4f^{11}$ Ho/MgO, this leads to a state of low angular momentum being more favourable, as will be shown later.

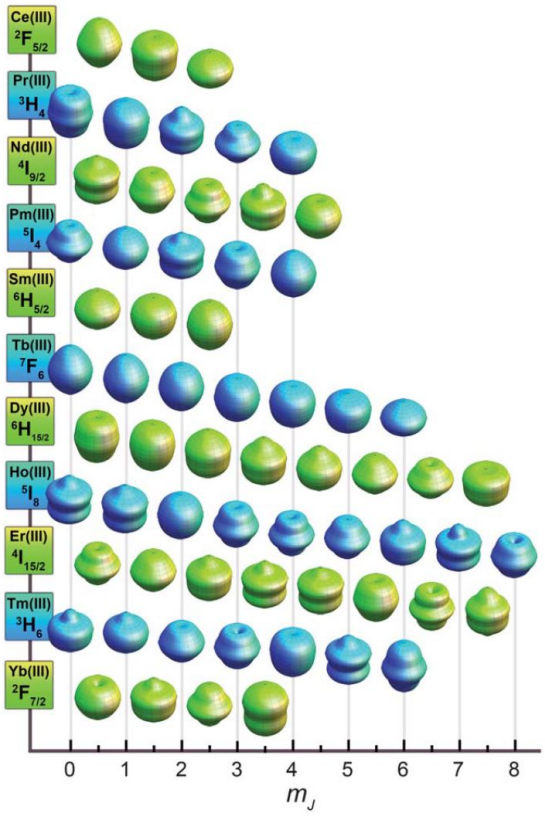

Figure 1.10: **Approximate 4f orbital shape**: Depending on the precise charge and angular momentum state, the orbitals can have a more prolate or oblate shape. Ligand fields lift the degeneracy between different angular momentum states [61].

2 Upgrading a conventional STM for ESR-STM

This chapter deals with upgrading a conventional low-temperature STM with variable magnetic field for ESR-STM. The initial part is based on our work published in Rev. Sci. Instr. [62], which shows the first ESR-STM data measured outside of the original machine at IBM Almaden Research Center [7]. The pros and cons of our setup will be discussed in detail. Due to several shortcomings both related to the ESR implementation as well as the STM itself, several technical improvements have been made afterwards, as will be discussed. Ultimately, the technical implementation of pulsed ESR experiments carried out in Korea at the Center for Quantum Nanoscience will be discussed.

2.1 Initial ESR-STM upgrades and field-sweep based ESR

The STM used at EPFL is home-made and is discussed in detail elsewhere [63, 64]. It allows measurements down to 0.4 K and at magnetic fields up to 8 T out-of-plane and 1 T and in-plane. Implementing ESR-STM required first and foremost physical installation of radio-frequency compatible cabling and creation of measurement software. The project was led by Dr. F. D. Natterer, who was also chief responsible for assembling the RF line. The author first and foremost wrote the measurement software and carried out most of the STM experiments.

Figure 2.1 shows a schematic of the electronic setup. The main difference compared to a standard STM setup is the RF generator (Keithley N5183B), which is joined with the standard bias line through a pick-off tee here. Alternatively, during later work at QNS, bias-tees and diplexers were used instead. These components can be chosen according to the specific needs at hand, although in any case the RF generator should be protected against DC pulses of the STM controller. The connection between the electronics and the vacuum feed-through leading towards the STM was implemented using flexible RF compatible cables in order to allow the whole machine to move freely and not provide a vibrational bridge across the vibration isolation. While in principle both the electronic lines leading up to the sample, as well as to the tip, can be made RF-compatible, the contact with the STM tip has a simpler geometry and

was therefore chosen to ideally avoid unnecessary spurious reflections.
Figure 2.2 shows the RF wiring inside the STM. RF compatibility is achieved by using stainless

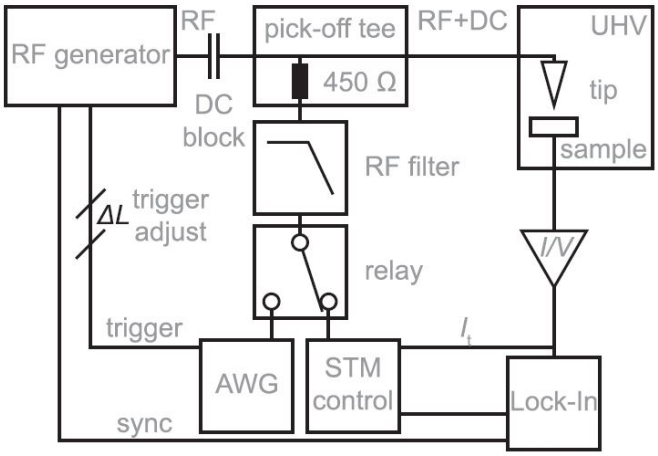

Figure 2.1: **Electronic Setup**: The diagram shows the fundamental electronic setup used during the first ESR-STM experiments at EPFL, which in similar fashion has also been used at QNS. The main difference compared to a traditional setup as displayed in fig. 1.1 is the addition of an RF generator and an AWG for pulsed experiments [62].

steel cables with silver coated center conductors (Coax Co. SC-119/50-SSS-SS). Thermal contact to the ^{4}He-stage is obtained by using 0 dB attenuators (XMA Corp. 2782) and clamping them into metallic holders. A flexible silver coated copper coax cable (Elspec Gefl AWG 38) is used to go from the mK-stage to the STM tip. While this cable is not suited for RF transmission up to the initially desired range (around 20 to 25 GHz), it was chosen for its flexibility in order to not block the movement of the piezoelectric motors at low temperatures. Equally, it is non-magnetic, and therefore should not perturb the tip in presence of a dynamic magnetic field. All connectors used are of SMA type.
Figure 2.3 shows the resulting RF transmission. Unfortunately, no broadband transmission as at IBM [43] was achieved. Several factors may play important roles. First, the STM tip is connected to the flexible cable in a rectangular geometry using silver epoxy in a relatively uncontrolled manner, which likely leads to strong RF losses. Equally, the flexible cable is connected to the semi-rigid stainless steel cable using a rectangular SMA connector. On top of the fact that rectangular connectors typically have smaller frequency ranges where they work well, the flexible cable is much too thin in order to be properly soldered to the connecter, and basically is held in place by solder of undefined shape. Standing waves within the flexible cable likely are responsible for the ≈686 MHz peak repetition pattern. In between a few well defined peaks, practically no RF transmission is found. Note that the RF voltages mentioned throughout this work denotes the zero-to-peak amplitude, as is commonly done in the ESR-STM community [43, 65]. In combination with the DC voltage, the zero-to-peak RF voltage allows to directly infer the expected energy range of the tunneling electrons.
In order to circumvent the absence of broadband RF transmission, magnetic field sweep based ESR-STM was carried out. Figure 2.4 shows a schematic of the implemented measure-

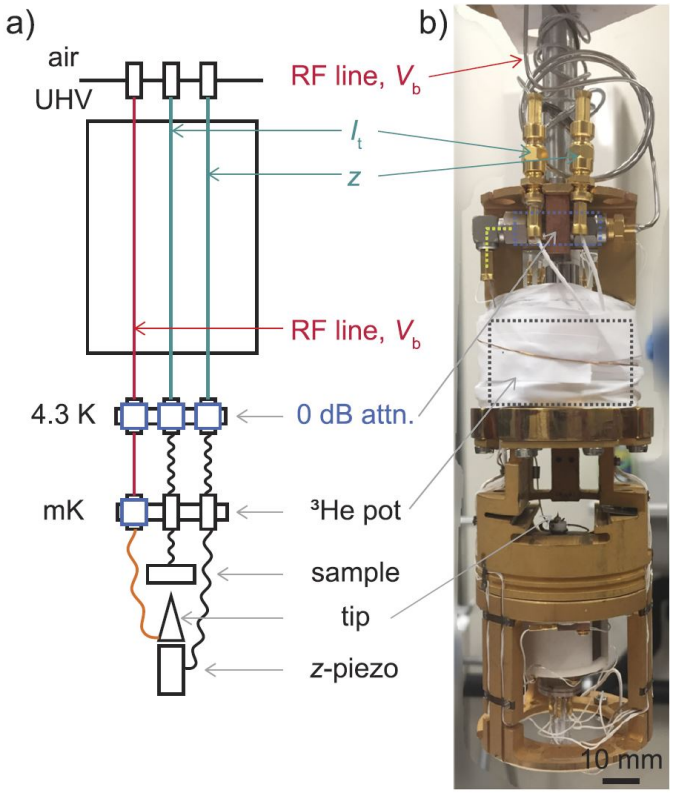

Figure 2.2: **RF wiring towards the STM head**: **a,** Schematic of the RF wiring from the room temperature vacuum feed-through down to the STM tip. **b,** Photo of the STM head prior to insertion into the cryostat [62].

ment scheme together with ESR-STM data acquired on TiH. The magnetic field was changed iteratively in discrete steps. At each field, an RF voltage was applied iteratively at different frequencies. The discrete frequencies were chosen such that significant RF transmission can occur. This allows for performing ESR-STM even if frequency sweeps are prevented due to the absence of broadband RF transmission. Equally, for applications where the precise line shape is unimportant, it is also not necessary to compensate the RF losses and have a specific RF voltage in the junction, which speeds up the measurement processes. This may be the case for example when simply extracting the Zeeman splitting of a surface spin or when extracting coupling constants between several spins. Another advantage of magnetic field sweeps is that unlike in frequency sweeps, imperfect knowledge of the frequency-dependent losses does not lead to additional noise. This commonly found transfer function dependent noise stems from frequency-dependent variations in the rectified background current. Note that effective magnetic field sweeps can also be carried out by varying the tip-sample distance, as will be demonstrated in a later chapter. While varying the magnetic field leads to mechanical instability and unintended tip indentions in some STM systems, for magnetic fields below 1 T and slow sweep rates, no significant instability was ever observed in both machines used throughout this work. Tracing the resonance frequency as a function of field allows to extract

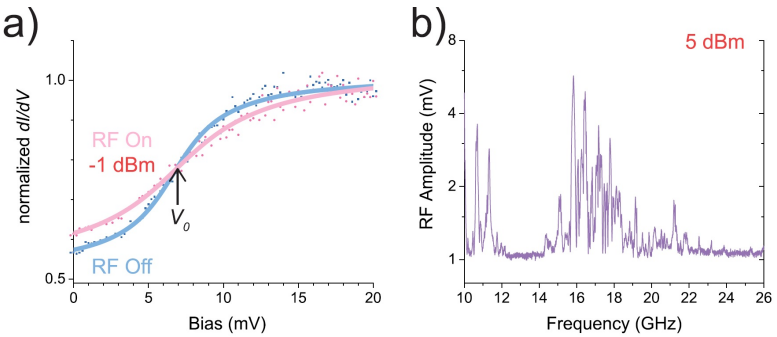

Figure 2.3: **In-Situ RF transmission**: **a,** Broadening of a non-linear dI/dV feature. For a source power of −1 dBm at 16.4 GHz, a step broadening of 2 mV was recorded. The solid line in blue represents a sigmoid function fitted to the differential conductance spectra obtained without an applied RF voltage. The solid line in pink is obtained by convoluting the blue line with an arcsine distribution whose width depends on the RF voltage in the tunneling junction, whose value is fitted to the experimental data. **b,** RF amplitude measured within the STM junction as a function of frequency when applying 5 dBm at the source. Note that the data is most likely spuriously offset by approx. 1 mV (V = 6.7 mV, I = 100 pA, T = 4.3 K) [62].

a magnetic moment of 1.00 ± 0.04 μ_B, in good agreement with previous studies [37].

In conclusion, we were able to set up the world's 2nd ESR-STM and provide an in-depth guide

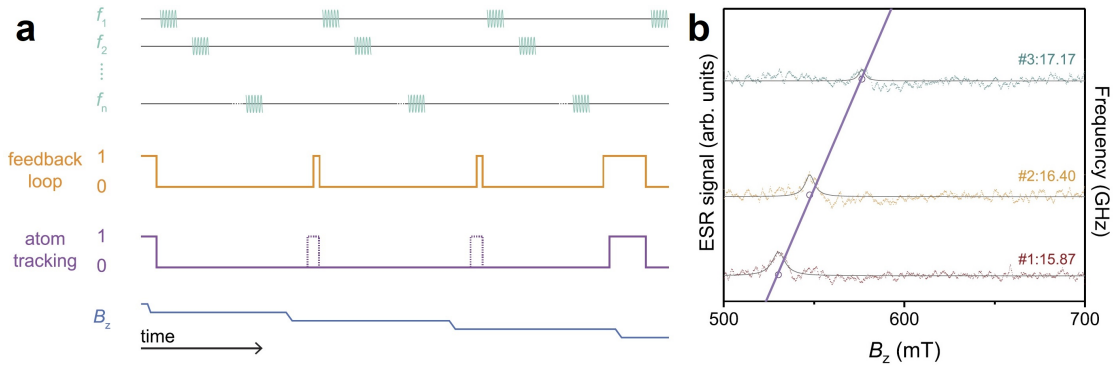

Figure 2.4: **Magnetic field sweep based ESR-STM**: **a,** The schematic shows the measurement scheme used during the initial work at EPFL. For a given magnetic field, and in open feedback loop, iteratively at different frequencies an RF voltage was applied. When changing the magnetic field, the feedback loop was engaged and occasionally an atom tracing to center the STM tip was performed. **b,** ESR-STM trace on top-site TiH (V = 60 mV, I = 30 pA, $P_{\mathrm{Src}}^{\mathrm{RF}}$ = 20 dBM, T = 2 K) [62].

on how it was achieved. However, the measurements were almost impossible to reproduce, in large parts due to reasons not related to the actual ESR setup. The STM as a whole proved to be highly unstable and many of its mechanical and electronic parts were worn-out. In the end, a majority of time was spent on fixing issues related to malfunctioning equipment. Ultimately, it was decided that the whole laboratory will receive a makeover. A majority of parts, including the whole STM frame, vacuum pumps and gauges, gas lines, vibration isolation, etc., were

replaced. This makeover took up more time than any other project presented in this work, but was relatively low-level work and will not be described any further. As part of this task, however, the whole RF wiring was replaced. Excellent broadband RF-transmission was achieved in the end, as is described in the next section.

2.2 Later changes to the ESR setup

Upgrading the RF wiring served several goals. First, by using adequate components and designing a suitable cable-tip connection, spurious oscillations in the transfer function were to be eliminated. By using RF components with lower broadband losses, a minimal broadband attenuation was achieved. To enable longer measurement times and enhance mechanical stability, the thermal load was reduced. Finally, since the RF generator works up to 31.8 GHz, the SMA components were replaced in order to be able to use the whole frequency range with minimal losses. This work was carried out predominantly by the author, Dr. J. Schwenk, and C. M. Soulard.

First, all SMA connectors were replaced by SMK and SMPM connectors. SMA connectors are typically designed to function well up to 26.5 GHz or less. On the other hand, SMK connectors typically work well up to 40 GHz, while SMPM connectors work well in some cases up to 65 GHz. The advantage of SMA connectors is their widespread use and cheap price. Switching to SMK, however, is relatively simple since they have almost the same geometry and can be easily installed by anyone able to work with SMA connectors. Due to this, we installed SMK based components starting from the RF generator all the way down to the mK-stage. SMPM connectors are extremely narrow with a maximum diameter of 3.23 mm in our case (Amphenol RF 925-124P-51S), and therefore can be used in tight spaces. Here, they were used at the mK-stage. The Amphenol RF 925-124P-51S connectors, although not specifically rated, do not use the frequently found nickel plating, and therefore are practically non-magnetic and can be used safely in vicinity of the STM tip even in presence of a large and dynamic magnetic field. While significantly more expensive, these components certainly played a role in allowing for broadband frequency transmission up to the maximum frequency of the RF generator. In order to achieve even fewer losses, a superconducting cable (Coax Co. SC-119/50-NbTi-NbTi) was installed between the ^{4}He and mK-stage. With an attenuation of less than 0.4 dB/m compared to the 5.2 dB/m of the stainless steel cable at 4.2 K and 20 GHz, the RF attenuation and consequently the thermal load on the cryostat, especially at the mK stage, should be significantly reduced. Equally, the superconducting cable has a thermal conductivity of 7.54×10^{-6} W×cm/K at 4 K, more than a factor 10 less than the stainless steel based cable. While we do have an improved holding time when using for example the ^{3}He reservoir in one-shot mode, the amount of ^{3}He in the system has been increased in the meantime and therefore an objective comparison is not possible. Nonetheless, on top of the increased hold time, the temporary heating observed when temporarily applying a large RF voltage has significantly decreased, which reduces thermal drift during ESR-STM

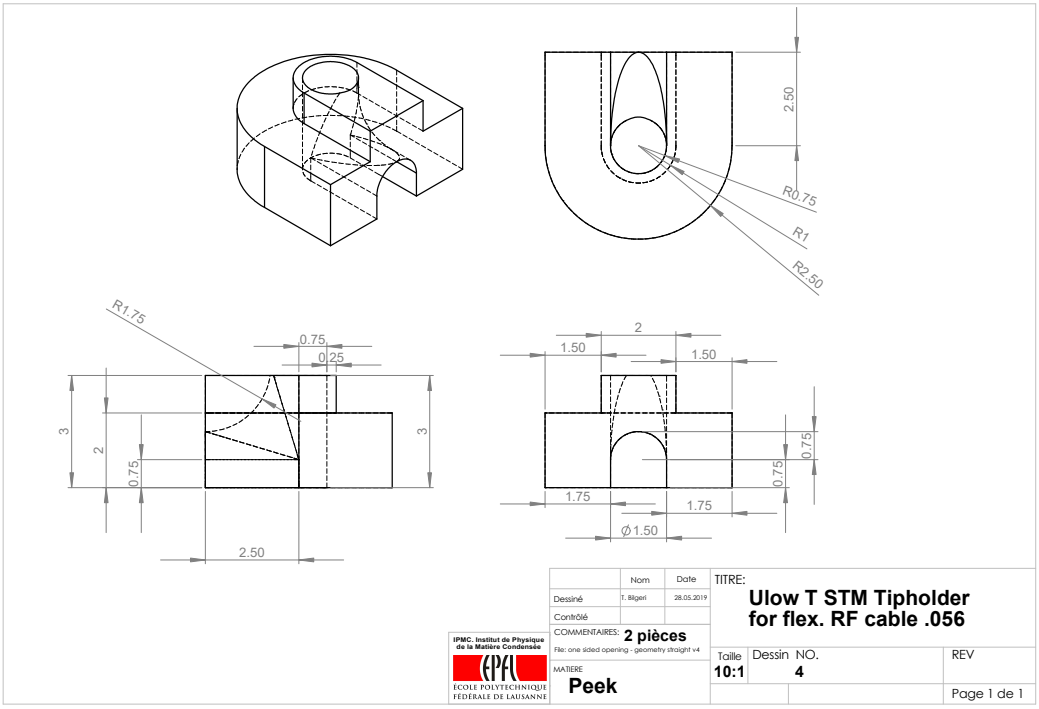

Figure 2.5: **Technical drawing of the novel tip holder**: Rather than having the tip glued to the bias line at a rectangular angle and with the outer conductor ending several millimetres before the tip apex, this tip holder allows to insert a flexible cable at a smooth curvature. The cable comes in from the side and is curved upwards. The outer conductor is removed only at the top end of the tip holder. An additional isolation ring is added to protect the center conductor beyond the tip holder (not drawn here). Within the through-hole of the isolation ring, the STM tip is directly glued atop of the center conductor.

measurements. In order to achieve a low effective electron temperature, the superconducting cable is thermally grounded to the mK-stage by being glued to a piece of copper across several centimeters, which in return is attached to the mK-stage. Finally, the previously used flexible cable was replaced by a flexible cable generously provided for free by Dynawave. While the precise specifications are confidential, we have found excellent broadband RF transmission, no mechanical blocking of the piezo motors even at 0.4 K, and no mechanical instability in magnetic fields up to 8 T.

Lastly, we have designed a new custom tip holder. The goal was to avoid rectangular angles and an ill-defined contact in the transmission line. Figure 2.5 shows a technical drawing of the newly designed tip holder. The cable enters from the lower side and is bended upwards within the tip holder. At the upper end, the cable is cut, with only the center conductor sticking out by approx. 1 mm. The extended center conductor is shielded using a standard isolating ceramic ring as is typically delivered with RF connectors. On top of the center conductor, we directly glued the STM tip. Figure 2.6 shows the STM tip-holder installed in the

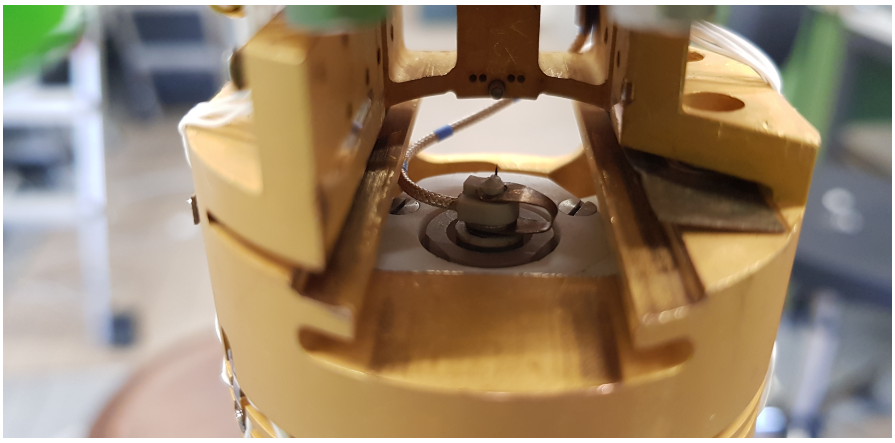

Figure 2.6: **Novel tip holder installed in the STM head**: The tip holder (white) is held in place by a metallic spring, which had equally been used before in conjunction with the old tip holder. In the background, the flexible RF cable leading up to the STM tip can be seen.

STM. Despite undercutting the minimum bending radius of the Dynawave RF cable, the RF transmission turned out to be excellent. The resulting RF transmission in the STM junction and a comparison with the RF transmission of the STM used at QNS is displayed in fig. 2.7. To the best knowledge of the author, and within the measured frequency range, this represents the best RF transmission to an STM junction published to date[43, 65, 66], beating out the RF antenna based approach in ref. [65]. The losses are very close to the intrinsic limitation given by the sum over the expected losses of all parts used, as can be found in the spec sheets of the respective parts. The frequency dependent losses are hereby characterised using the unitless transfer function which has been defined differently in the work by W. Paul. *et al.* [43] and T. Seifert *et al.* [65] as

$$TF_{\text{Seifert}} = 10 \times \log\left(\frac{V_{\text{J,0-p}}}{V_{\text{S,0-p}}}\right) \tag{2.1}$$

$$TF_{\text{Paul}} = V_{\text{J,dBmV}} - P_{\text{S,dBm}} \tag{2.2}$$

$V_{\text{J,0-p}}$ and $V_{\text{S,0-p}}$ denote the zero-to-peak RF voltages in the STM junction and at the RF source respectively, $V_{\text{J,dBmV}}$ the RF voltage in the STM junction in decibels relative to one millivolt (dBmV) and $P_{\text{S,dBm}}$ the RF power applied at the source. Using the relations given in ref. [43]

$$P_{\text{S,RMS}} = \frac{V_{\text{S,0-p}}^2}{2 \times 50\Omega} \tag{2.3}$$

$$P_{\text{S,dBm}} = 10 \times \log\left(\frac{P_{\text{S,RMS}}}{1\ \text{mW}}\right) \tag{2.4}$$

$$V_{\text{J,dBmV}} = 20 \times \log\left(\frac{V_{\text{J,0-p}}}{1\ \text{mV}}\right) \tag{2.5}$$

where $P_{\text{S,RMS}}$ denotes the root-mean-square power assuming an impedance of 50 Ω, it can be

verified that [65]

$$TF_{\text{Seifert}} = \frac{TF_{\text{Paul}} - 50}{2} \tag{2.6}$$

The transfer function shown in fig. 2.7 is based on TF_{Seifert} due to its more intuitive properties (*e.g.*, zero losses lead to a transfer function of zero, finite losses lead to a negative transfer function). Most of the software used throughout this work is based on the original definition TF_{Paul}.

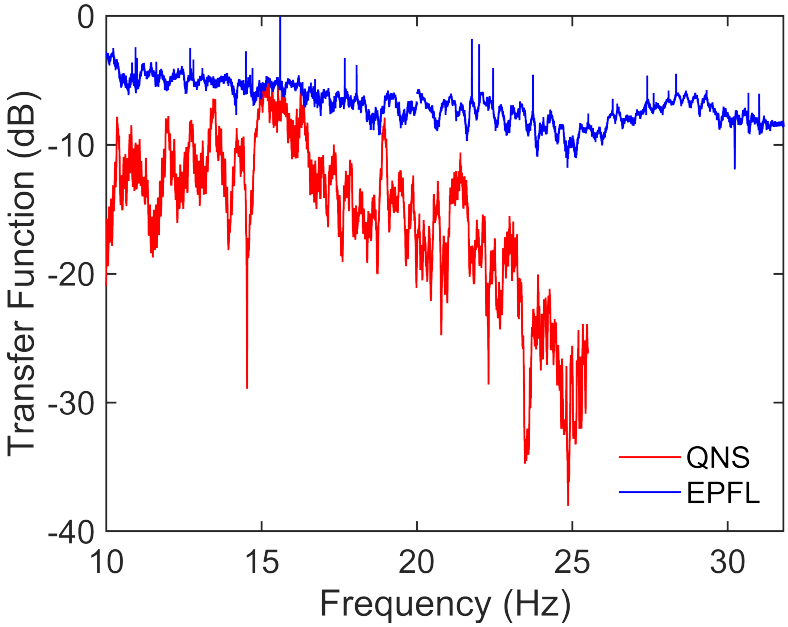

Figure 2.7: **Transfer function**: The transfer function, in this case defined as 10 times the decadic logarithm of the ratio between the zero-to-peak RF voltages in the junction and at the signal generator (TF_{Seifert}), shows strongly non-linear frequency dependent losses. By knowing these losses precisely using the methods introduced by W. Paul *et al.* [43], ESR-STM based on frequency sweeps at approximately constant RF voltage can be carried out. Pulsed experiments at QNS, where relatively high RF voltages around 100 mV where commonly used, were typically carried out in a frequency window between 15 and 16.6 GHz due to particularly small losses within that range. The target RF voltages in the junction for these traces were 7 and 5.2 mV zero-to-peak at EPFL and QNS, respectively. Note that some individual spikes in the EPFL transfer function were due to pinging noise and do not reflect the actual transfer function. These transfer functions were obtained using non-linearities found in Fe/MgO and surface states on Ag(111) at QNS and EPFL, respectively.

2.3 Pulsed ESR

The electronic setup used at QNS for pulsed ESR-STM is in principle equivalent to the one shown in fig. 2.1. The Arbitrary Waveform Generator (AWG, Tektronix 70002A) is used to gate

the output of the RF generator (Keysight E8257D) using pulse trains of square waves. This leads to the RF generator sending out pulses of sinusoidal waves with well defined widths required for example for direct observation of Rabi oscillations and Hahn spin echos. Empirically, we have measured meaningful signals in pulsed ESR starting at pulse widths of 5 ns, in line with the specifications of the RF generator. The electronic devices were synchronized through the lock-in (Stanford Research Systems SR860). In this work, in order to enhance the signal-to-noise ratio, amplitude modulation controlled by the lock-in was carried out. Here, using a 50% duty cycle, RF pulses were only applied during the first half of the cycle, and were absent during the second part of the cycle. The desired signal is then obtained by subtracting the second cycle from the first. All electric devices were controlled using Matlab software developed by Dr. P. W. Willke, the author and Prof. M. Hervé, which is now used by several research groups around the world. Importantly, in this software implementation, the Nanonis control electronics of the STM is accessed through Matlab by interfacing it with the Labview libraries provided by Nanonis, allowing for fully automated measurements lasting several hours or days. This represented a massive increase in productivity compared to the previously very labour intensive STM work for the groups involved. Lastly, note that in order to combine an RF-STM setup with all-electric traditional pump-probe experiments possessing temporal resolution down to the nanosecond range as recently used by L. M. Veldman *et al.* [42], the path between the AWG and RF line also has to allow for sufficient broadband RF transmission in order to create square waves with fast rise times.

3 Coherent spin control of single magnetic molecules on surfaces

Previous ESR-STM experiments focused on individual or hydrogenated transition metal adatoms and nanostructures thereof, using either Fe, TiH or Cu. The goal of this work was to extend this technique to magnetic molecules beyond TiH. A first study with this goal in mind was carried out at QNS by X. Zhang *et al.* [67] using the organic molecule tetracyanoethylene (TCNE) on MgO. However, the organic molecule itself did not show any spin signature. Artificially created Fe-TCNE complexes showed almost no interaction between the 3d orbitals of the Fe adatom and the molecule, with the magnetic properties of the Fe staying almost the same compared to the isolated case. In a second attempt, the metal-organic complex iron phthalocyanine (FePc) was chosen. FePc was found to form a spin-1/2 system on MgO/Ag(100) and both CW and pulsed ESR experiments were carried out. These measurements represent the first ESR-STM measurements of a metal-organic molecule. Two manuscripts are currently in preparation for publication. The first, by X. Zhang *et al.* [68], deals with the anisotropic magnetic exchange interaction found between FePc and neighbouring spins. It also includes detailed DFT calculations. The second, with equal authorship being shared between Dr. P. Willke and the author, deals with coherent manipulation of the FePc spin [69]. The latter work will be presented in detail. The author was involved in all experiments and analysis thereof presented in the following, unless explicitly mentioned otherwise.

3.1 Characterization and coherent control of FePc/MgO

Phthalocyanine molecules have a planar geometry and are thus well suited for STM studies of its magnetic properties [70, 71]. They form a spin-1 system in bulk and on several surfaces [72, 73]. On MgO/Ag(100), we find it to form a spin-1/2 system based on differential conductance measurements, which results from a charge transfer to the Ag substrate according to DFT calculations [68]. Figure 3.1 shows a schematic of the ESR-STM experimental setup, a ball-and-stick model of FePc, STM topograhic images of FePc/MgO, and initial CW-ESR-STM measurements. In the topographic images, the molecule can be easily identified by its characteristic cross-like shape. The CW-ESR measurements at different fields show a

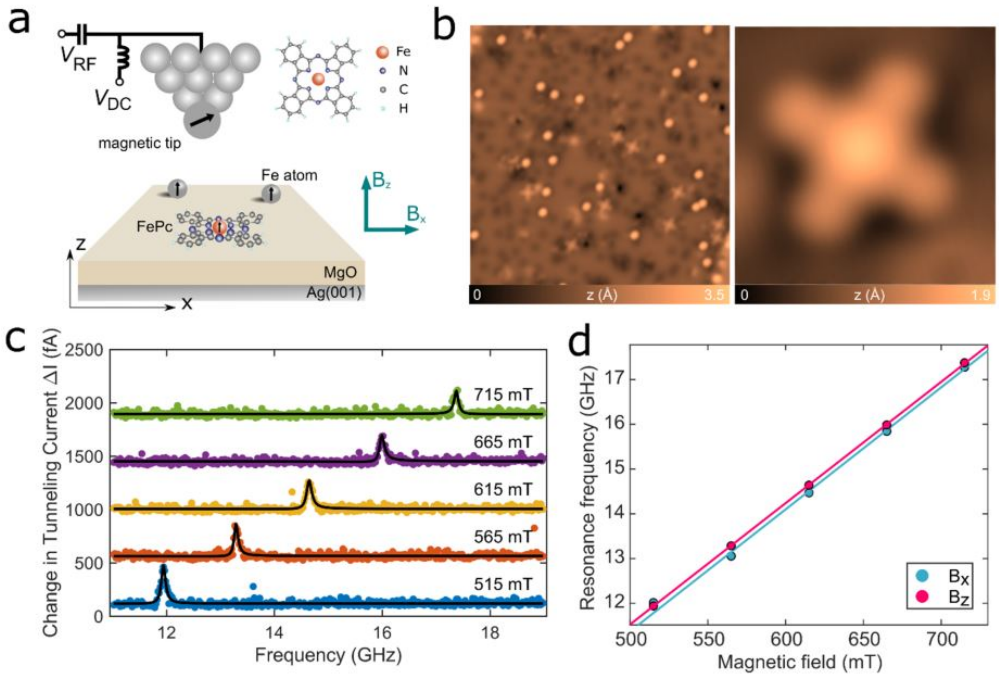

Figure 3.1: **Experimental setup and CW-ESR on a surface adsorbed metal-organic molecule**: **a,** Schematic of the experimental setup. The FePc molecules have a planar geometry with the central Fe atom being surrounded by organic ligands. Fe adatoms are used to prepare spin-polarized tips. **b**, Topographic image of MgO/Ag(100) with Fe adatoms and FePc molecules. The molecules have a typical apparent height of approx. 60 pm and are therefore significantly smaller than the Fe atoms that appear at approx. 180 pm apparent height (I = 20 pA, V_{DC} = 100 mV, image size 32.5 × 32.5 nm). On the right, a close-up view of FePc is displayed (I = 50 pA, V_{DC} = −5 mV, image size 2.4 × 2.4 nm). **c**, CW-ESR spectra of FePc at varying out-of-plane magnetic field (I = 27.5 pA, V_{DC} = −50 mV, V_{RF} = 6 mV, T = 0.95 K). **d**, Resonance frequency as a function of the out-of-plane and in-plane magnetic field acquired with the same tip and molecule [69].

Zeeman splitting indicating a magnetic moment of approximately 1 μ_B. Note that the precise moments unfortunately vary due to the high defect density in the MgO used for this study, as well as the method used (dI/dV, CW-ESR with varying tip field, and CW-ESR with varying external field). Averaging over 14 different molecules in an out-of-plane magnetic field we find 1.028±0.023 μ_B, and an approximately 5% reduced moment in an in-plane magnetic field [68].

Next, pulsed ESR-STM experiments were attempted. From an empirical point of view, just like picking up a set number of Fe atoms does not always lead to a spin polarized tip, and not every spin polarized tip is capable of CW-ESR-STM, not every tip capable of CW-ESR-STM shows a signal in pulsed ESR-STM experiments. Typically, about 10 to 20 CW-ESR-active tips had to be tested until a tip suitable for pulsed ESR-STM experiments was found. Potentially, this results from the fact that the coherence time at equal experimental parameters but with different

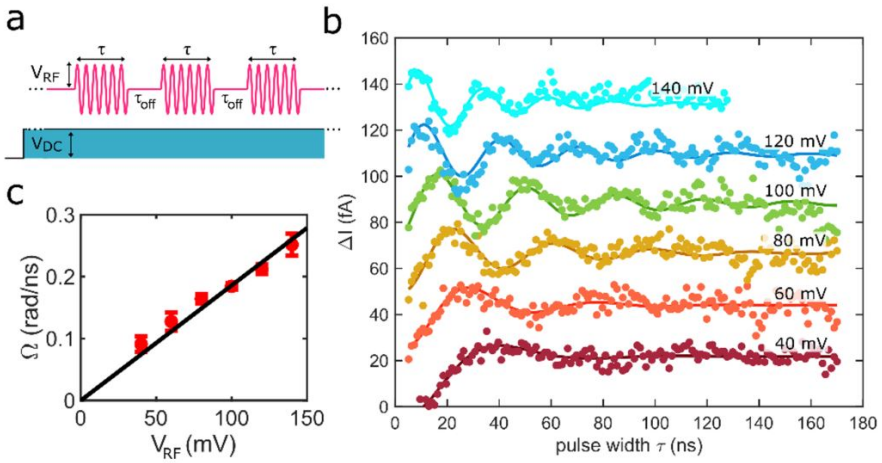

Figure 3.2: **Rabi oscillations**: **a**, Schematic of the pulse sequence. **b**, Measured Rabi oscillations at different applied RF voltages (I = 5.2 pA, V_{DC} = 70 mV, f = 16.227 GHz, B_z = 574 mT, T = 390 mK, τ_{off} = 500 ns). Lines are fitted following $I_0 \times \sin(\omega\tau + \alpha) \times \exp(-\tau/T_2^*)$. A linear slope resulting from the rectified current proportional to V_{RF} was removed prior to fitting and displaying the data. All traces are offset for clarity. **c**, Rabi rate as a function of the RF voltage. A linear fit yields (1.86 ± 0.13) rad/(μs$\cdot$ mV) [69].

magnetic microtips can vary up to a factor 10, as was determined in earlier work using CW-ESR measurements [40]. Strongly reduced coherence times, potentially in combination with a weak Rabi force, would render measurements impossible. Figure 3.2 shows Rabi oscillations measured on individual FePc molecules. Just like for TiH [8], we find a linear dependence of the Rabi rate on the RF voltage. Typically we found Rabi frequencies of around 20 MHz at RF voltages of around 100 meV, similar to what was found for TiH. For the data shown in fig. 3.2, we find a coherence time T_2^* = (42 ± 15) ns, again similar to the values found for TiH.

Next, in order to study the quantum coherent properties of FePc in greater detail, Hahn spin echo measurements were performed. These measurements have the advantage of partially cancelling out dephasing noise. The coherence time T_2^* can be written as [46]

$$(T_2^*)^{-1} = (T_2)^{-1} + (T_2')^{-1} \tag{3.1}$$

T_2^* represents the effective decoherence rate as measured in Rabi experiments, T_2 the intrinsic and irreversible decoherence rate, and T_2' the dephasing due to slowly fluctuating magnetic fields (angular frequency $\ll \omega_{\mathrm{L}}$). The last term arises for example due to nuclear spins in the environment such as the ones found in ^{14}N surrounding the central Fe ion in FePc. Specifically found in ESR-STM is the fluctuating magnetic field induced by the magnetic STM tip in combination with mechanical vibrations leading to a dynamically varying tip-molecule distance and thus a dynamically varying tip magnetic field [40]. Hahn spin echo measurements, as well as more complex schemes for dynamical decoupling, allow to partially eliminate this dephasing, resulting in the effectively measured coherence time being close to the intrinsic

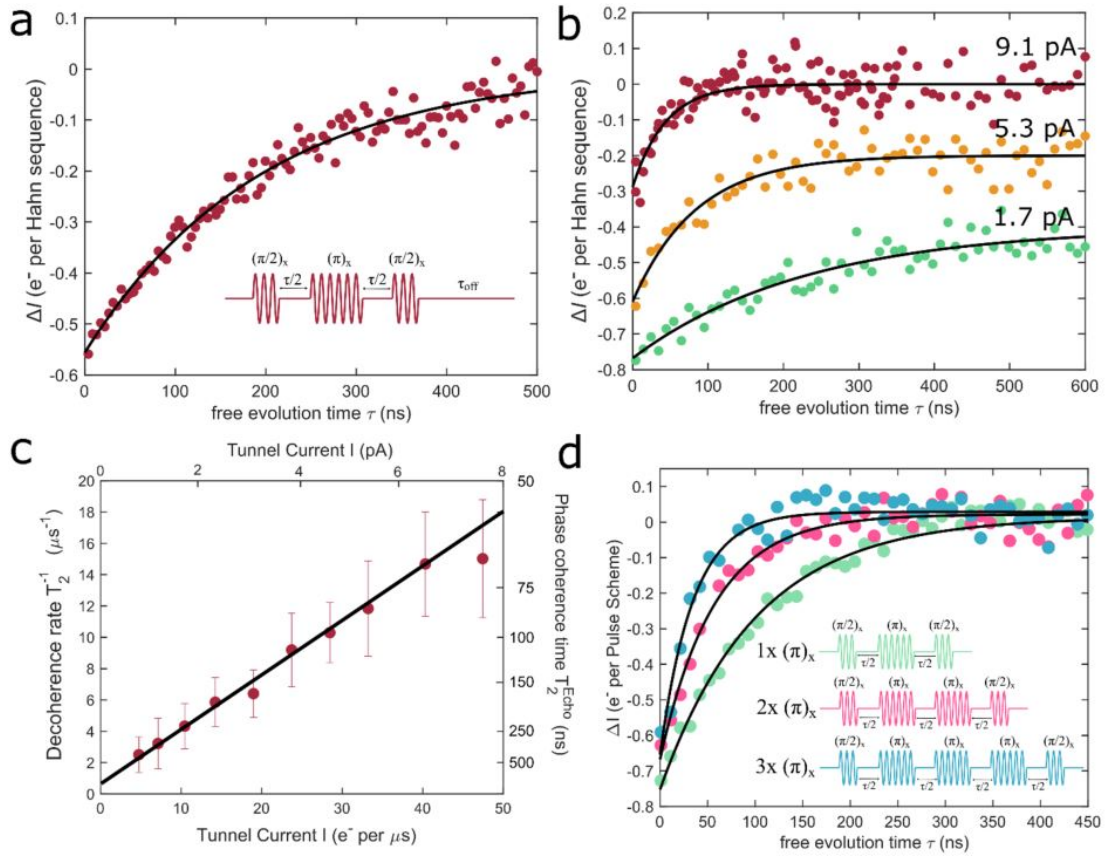

Figure 3.3: **Hahn spin echo measurements of FePc/MgO**: **a,** Representative measurement (red) with fit (black) following $I_0 \times \exp(-\tau / T_2^{\mathrm{Echo}})$, which yields T_2^{Echo} = (196 ± 26) ns and I_0 = (0.56 ± 0.03) e$^-$ per pulse sequence. Inset shows the pulse scheme (I = 2.2 pA, V_{DC} = 30 mV, V_{RF} = 100 mV, f = 16.179 GHz, B_z = 574 mT, T = 390 mK, τ_{off} = 500 ns). **b,** Hahn echo at different tunneling currents (V_{RF} = 100 mV, f = 16.179 GHz, B_z = 574 mT, T = 430 mK). The tunneling current was varied by disengaging the feedback loop and then changing the DC voltage. **c,** Decoherence rate as a function of the tunneling current. Black line represents a fit based on eq. 3.2. **d,** Effective coherence time for a varying number of Pi-pulses (I = 5.3 pA, V_{DC} = 70 mV, V_{RF} = 100 mV, B_z= 574 mT, f = 16.169 GHz, T = 380 mK) [69].

decoherence rate T_2.

Figure 3.3a shows a Hahn echo measurement of FePc together with the pulse sequence. We find a resulting coherence time of T_2^{Echo} = (196 ± 26) ns at a tunnel current of 2.2 pA, again similar to the values found for TiH at a tunnel current of 3 pA. Next, we probed the coherence time as a function of the tunnel current setpoint. Previously, it had been shown in Fe/MgO, using CW-ESR, that the decoherence rate scales linearly as a function of the current [40]. Figure 3.3b shows the Hahn spin echo as a function of the tunnel current. At 1.7 pA, the coherence time T_2^{Echo} is significantly enhanced compared to higher currents. However, the signal decreases due to the reduction of the DC current, and therefore a reduction in the

homodyne signal. At 5.3 pA, the signal is much stronger, but the coherence time is significantly reduced. For larger currents, the signal starts to vanish due an excessive and irreversible decoherence induced by the tunneling electrons.

Assuming a perfect cancellation of the dephasing noise, we can model the measured decoherence rate T_2^{Echo} as

$$(T_2^{\mathrm{Echo}})^{-1} = (T_2)^{-1} + (T_2^{\mathrm{e}^-})^{-1} \tag{3.2}$$

The term $T_2^{\mathrm{e}^-}$ represents the tunneling electron induced decoherence. It can be written as

$$T_2^{\mathrm{e}^-} = \frac{P_{T_2}}{e} \times I \tag{3.3}$$

where P_{T_2} denotes the probability per tunneling electron to induce a decoherence event. Figure 3.3c shows the decoherence rate $(T_2^{\mathrm{Echo}})^{-1}$ as a function of current. Based on this linear trend, we find P_{T_2} = (32±3)%, *i.e.*, approximately every third tunneling electron induces a decoherence event. By linearly extrapolating to zero current, we expect T_2 = (1.02±0.52) μs, which represents an upper limit for the intrinsic irreversible coherence time. Figure 3.3d shows an initial attempt to use a more complex pulse scheme. However, due to the tunneling electrons being by far the most dominant source of decoherence at typical measurement parameters, extended dynamical coupling schemes in ESR-STM can potentially decrease the measured coherence time due to the additional tunneling electrons passing through the spin. More complex dynamical decoupling schemes such as Carr-Purcell-Meiboom-Gill require a vector signal generator, which was not used as part of the work presented here.

Ultimately, we applied ESR-STM to magnetically coupled FePc molecules. Figure 3.4a shows CW-ESR spectra of molecules at the onset of lattice formation. The distance between the Fe atoms in two neighbouring molecules is 5 MgO lattice constants, *i.e.*, 1.44 nm. Based on dipolar coupling between the two neighbouring spin centers [15] and assuming a magnetic moment of 1 μ_{B}, one would expect two resonances split by 17 MHz for an FePc molecule with a single nearest neighbour. In practice, however, this coupling is significantly enhanced due to a ligand mediated exchange coupling, as demonstrated in our work in ref. [68]. For the measurements displayed here, we find the resonances to be split by (62±5) MHz. Figure 3.4b shows Hahn spin echo measurements on FePc molecules with 1 to 3 neighbours. For each measurement, the applied frequency was chosen equal to the resonance frequency at the most intense peak, which is determined by the effective spin temperature of the nearby molecules [15]. As expected, the coherence time tends to decrease with an increasing number of neighbours. In order to simulate this trend, Monte-Carlo calculations were carried out, whereby the nearby molecules were simulated as fluctuating magnetic moments with characteristic fluctuations rates given by their inverse lifetime $(T_1)^{-1}$. Figure 3.4c shows exemplary simulated spectra, and fig. 3.4d a comparison between the experimentally determined coherence times and simulated values for different assumed T_1. Among the displayed traces, the best agreement is

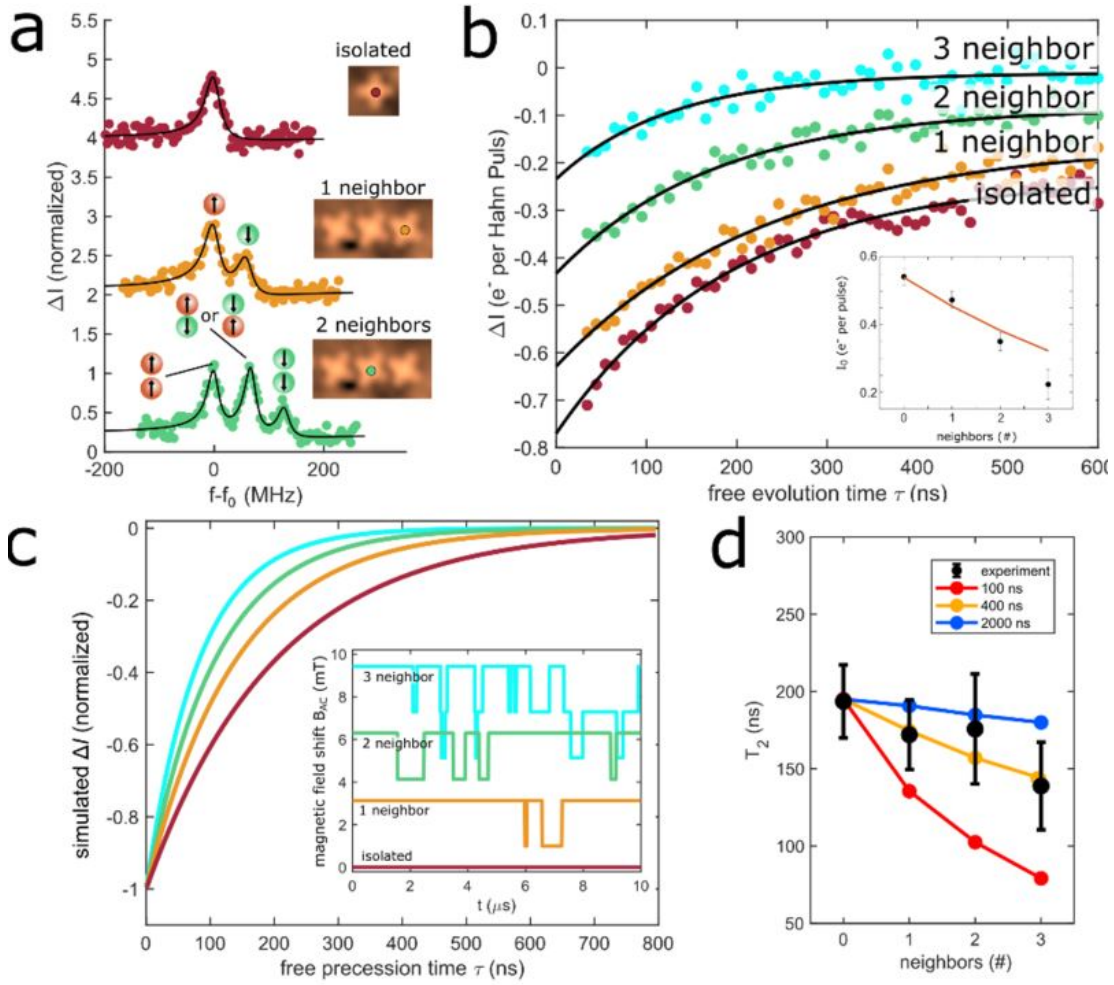

Figure 3.4: **Hahn spin echo measurements of FePc/MgO in self-assembled molecular nanostructures**: **a,** CW-ESR of molecules with different numbers of nearest neighbours (I = 3.0 pA, V_{DC} = 60 mV, V_{RF} = 20 mV, B_z= 574 mT, f = 16.0 - 16.2 GHz, T = 1 K). **b,** Hahn spin echo measurements as a function of the number of nearest neighbours. Spectra are offset for clarity. Inset shows the signal obtained per pulse (I = 2.3 pA , V_{DC} = 30 mV, V_{RF} = 100 mV, B_z= 574 mT, f = 16.188 GHz, T = 460 mK). **c,** Exemplary simulated spectra for FePc molecules with different numbers of nearest neighbours. Inset shows exemplary traces of the effective magnetic field fluctuations as sensed by the FePc molecule under investigations. Due to the low temperature, the neighbouring FePc molecules spend most of the time in the ground state. **d,** Coherence time as a function of the number of nearest neighbours. The simulated traces assume different lifetimes [69].

found for T_1 = 400 ns, similar to the lifetime found for bridge site TiH [41].

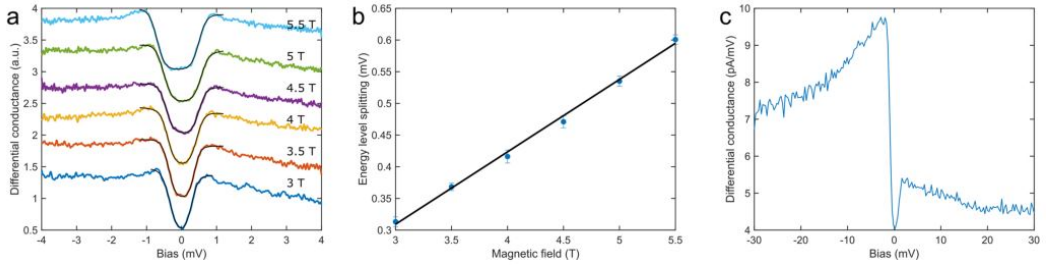

Figure 3.5: **Spin-flip spectroscopy**: **a,** Differential conductance spectra at different magnetic fields ($I_{\text{setp.}}$ = 120 pA, $V_{\text{Setp.}}$ = 4 mV, T = 0.85 K, $V_{\text{mod.}}$ = 0.08 mV). **b,** Energy level splitting as a function of the external out-of-plane field. The slope of the fitted line (black) indicates a magnetic moment of 0.99 ± 0.04 μ_B. **c,** Differential conductance spectra measured with a spin-polarized tip ($I_{\text{setp.}}$ = 550 pA, $V_{\text{Setp.}}$ = 4 mV, B_z = 600 mT, T = 0.6 K, $V_{\text{mod.}}$ = 0.5 mV) [69].

3.2 Supplementary Information

Figure 3.5 shows differential conductance spectra of FePc. When applying a magnetic field, we find a single inelastic excitation corresponding to a spin excitation within the spin doublet. The energy splitting is linear in magnetic field and the spectral shape strongly changes when using a spin-polarized tip, both demonstrating the magnetic origin of the excitation. Large scale differential conductance measurements showing the highest occupied and lowest unoccupied molecular orbitals and comparison with DFT calculations can be found in ref. [68].

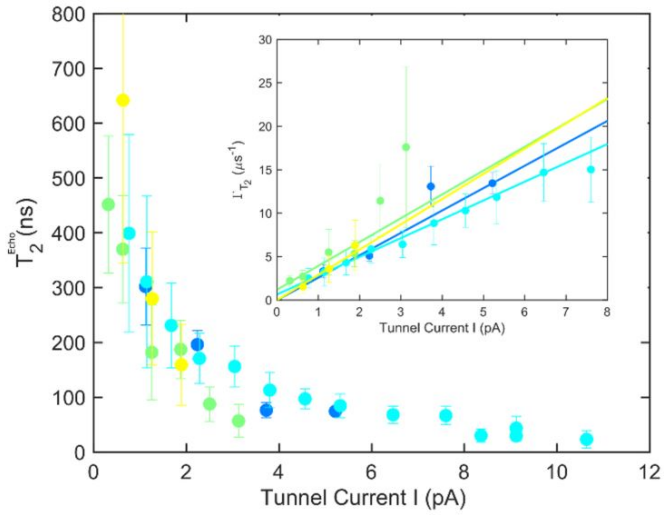

Figure 3.6: **Hahn spin echo with varying tips and molecules**: Different colors denote different data sets. All spectra were taken on different molecules. Blue and Cyan were taken on different molecules but with the same microtip. All experiments were taken at approx 0.5 K and 575 mT. Fitting with eq. 3.2 yields scattering probabilities and intrinsic coherence times of (32±3)% and (1018±524) ns (cyan), (44±29)% and (836±976) ns (green), (41±32)% (blue), and (47±179)% (yellow). If not stated, the decoherence time was too uncertain to yield a reasonable value [69].

Figure 3.6 shows additional current dependent Hahn echo measurements with different tips and on different molecules. The precise current dependent coherence rate varies with the STM tip, as has also been found earlier for Fe [40] and TiH[8]. However, the overall trend is very similar for all tips and molecules, demonstrating reproducibility of our measurement.

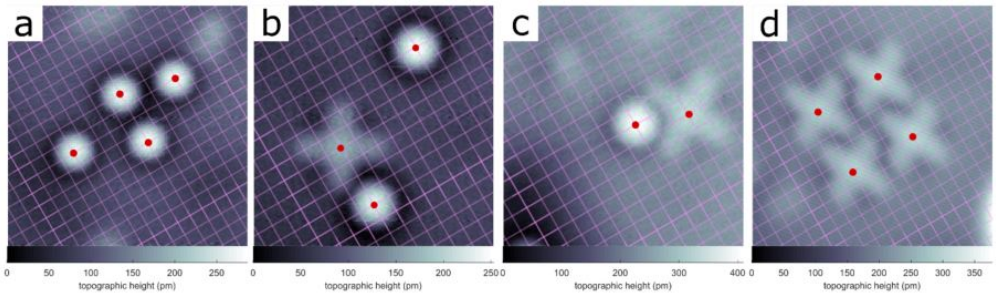

Figure 3.7: **Lattice site determination**: **a,** Fe only, for the purpose of calibration. **b,** FePc sitting next to Fe, at an angle of −30° w.r.t. the MgO lattice. **c,** FePc with a different angular orientation, at an angle of +30° w.r.t. the MgO lattice. **d,** Onset of a self-assembled molecular lattice. The distance between the nearest neighbours corresponds to 5 MgO lattice constants ($I = 20$ pA, $V_{DC} = -100$ mV) [69].

Figure 3.7 shows a more detailed analysis of the binding site of FePc and of molecular lattices. Here, individual Fe atoms are used to calibrate the piezos in-plane, and mark the O sites of the underneath MgO. Using their well known adsorption site, it is then possible to identify the adsorption configuration of FePc. It can be seen that the central Fe ion sits atop of O, while its ligands are rotated by approximately ± 30 degrees with respect to the underlying MgO lattice. The minimal spacing between neighbouring FePc molecules corresponds to 5 lattice constants, as measured between the central Fe ions.

In the Monte Carlo simulations, carried out by Dr. Willke and used to simulate the additional decoherence in coupled spin systems, we simulate the effective stray field caused by a neighbouring FePc molecule as

$$B_{\mathrm{FePc}}(t) = \frac{h\Delta f}{2\mu_{\mathrm{FePc}}} \cdot \Phi(t) \tag{3.4}$$

Here, $\Phi(t) \in \{-1, +1\}$ accounts for a random magnetic two-state switching of the nearby FePc molecule. This approach should be valid in the case where the spin states can be in good approximation described as Zeeman basis states $|00\rangle$, $|01\rangle$, $|10\rangle$, and $|11\rangle$ [68]. In this notation, $|0\rangle$ corresponds to the ground state, and $|1\rangle$ to the excited spin state, of either one of the two molecules respectively. In this approximation, we are coherently inducing transitions between states $|0\rangle$ and $|1\rangle$ of the molecular spin underneath the tip, while the nearby spin fluctuates randomly between the two states. The switching probability of the excited spin state of the nearby spins is given by$1/T_1$ per unit of time, and the switching rate in the ground state follows

from a Boltzmann distribution. The phase aquired during a Hahn echo measured inbetween the pulses is given by [74]

$$\phi_1 = \gamma \int_0^{\tau/2} B_{\mathrm{FePc}}(t)\,dt \tag{3.5}$$

$$\phi_2 = \gamma \int_{\tau/2}^{\tau} B_{\mathrm{FePc}}(t)\,dt \tag{3.6}$$

using the gyromagnetic ratio γ=$\mu_{\mathrm{FePc}}/\hbar$. The phase difference ($\phi_2$-$\phi_1$) determines how much of the spin is projected into the ground and excited state.

$$P_0 = \cos^2(\frac{\phi_2 - \phi_1}{2}) \tag{3.7}$$

$$P_1 = \sin^2(\frac{\phi_2 - \phi_1}{2}) \tag{3.8}$$

The measured current is proportional to the population difference δP=P_1-P_0 between the excited and ground state, which ultimately can be compared to the experimental spectra in order to approximate the intrinsic lifetimes.

3.3 Conclusion and Outlook

In summary, we were able to carry out first ESR-STM experiments using an extended molecule beyond TiH. We characterized the system using different STM techniques and ultimately were able to quantum coherently manipulate the spin. We have found tunneling electrons to be the dominant source of decoherence and have shown coherent spin control of single molecules in molecular lattices. In other work not detailed here [68], we use ESR-STM and atomic manipulation to map out an anisotropic exchange coupling between an FePc molecule and surrounding spins mediated via the ligands. While many of the properties found in our work are not specific to molecules, and phthalocyanines may represent a class of molecules particularly suited for STM research compared to most others, our work nonetheless opens the door towards analysis of extended magnetic molecules, molecular lattices, and their quantum properties using ESR-STM.

For future research on FePc/MgO and similar systems, it may be interesting to measure the precise lifetime of the molecule through pump-probe experiments [14] and compare it to our analysis. Unfortunately, this was not carried as part of this work out due to a lack of time to implement the experimental setup. Similarly, it may be interesting to measure and compare the molecular spin dynamics in two or more coupled molecules close to and further away from an avoided level crossing (*i.e.*, compare the Zeeman and singlet-triplet regime in the case of two molecules), which can be achieved by varying the setpoint and thus the effective tip magnetic field applied to the molecule underneath the magnetic tip [41, 42, 68]. Equally, it

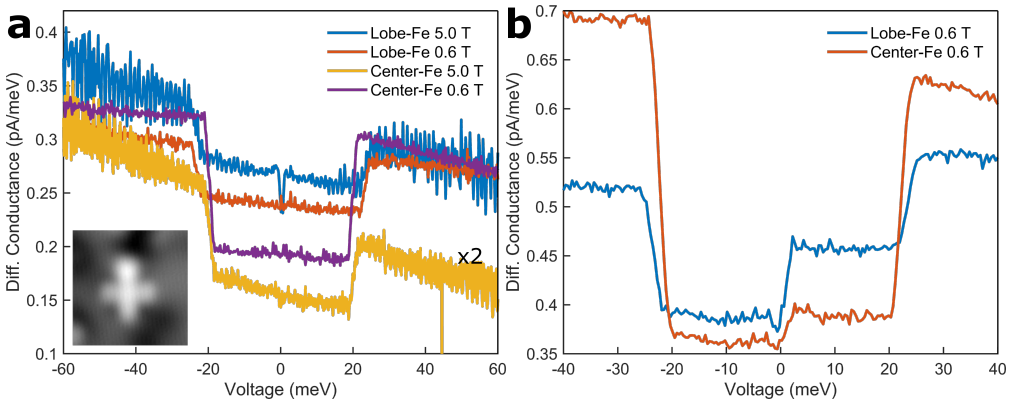

Figure 3.8: **On-surface synthesized Fe-FePc complex**: **a,** Differential conductance spectra measured on top of the Fe atom appearing within the FePc lobe (blue, orange with $I_{\text{setp.}}$ = 1 nA), and the Fe atom at the center of the FePc (yellow, purple with $I_{\text{setp.}}$ = 0.5 and 1 nA, respectively; the former spectra is multiplied by a factor 2 for ease of comparison) at 5 T and 0.6 T ($V_{\text{Setp.}}$ = 60 mV, B_z = 600 mT, $T \approx 0.7$ K, $V_{\text{mod.}}$ = 0.3 mV). Inset: Topographic image of the Fe-FePc complex. The initially isolated Fe atom can be seen towards to top end of the molecular structure (I = 20 pA, $V_{\text{DC}} = -100$ mV). **b,** Differential conductance spectra of the Fe-FePc complex with a spin polarized tip demonstrating the magnetic origin of the excitations ($I_{\text{setp.}}$ = 200 pA, $V_{\text{Setp.}}$ = 40 mV, B_z = 600 mT, T = 0.9 K, $V_{\text{mod.}}$ = 1 mV).

should be interesting to investigate and compare FePc made of ^{56}Fe and ^{57}Fe, whereby the latter possesses a nuclear spin of 1/2 [16] and makes up approximately 2% of the naturally occurring Fe. Unfortunately, due to the high defect density in the MgO sample used as part of this work, much more than 2% of the FePc molecules showed two ESR resonance peaks (which ideally would indicate hyperfine coupling) even in absence of nearby spins, and with varying splitting amplitudes, making it impossible to tell apart molecules containing ^{57}Fe from molecules coupled to magnetic defects. Ultimately, we also briefly investigated creating novel molecular magnetic structures by means of local manipulation *via* the STM tip, similar to ref. [67]. Figure 3.8 shows one exemplary outcome. Hereby, we picked up an FePc molecule with the STM tip, and subsequently dropped it off next to an Fe adatom by approaching the tip beyond point contact towards the Fe. This reproducibly leads to a structure where the Fe adatom appears to reside within a carbon ring of the ligand. The resulting Fe-FePc structure shows strongly altered magnetic properties compared to individual species, and the observed differential conductance spectra can with some level of accuracy be described by a spin-1/2 antiferromagnetically coupled to the Fe spin with altered crystal field parameters. This demonstrates the potential to on-surface synthesize novel molecular spin structures using FePc or similar molecules, with potentially novel and interesting quantum magnetic properties.

4 Dysprosium single atom magnets and engineered nanomagnets

ESR-STM so far has relied on studying systems with relatively low lifetimes, which ideally facilitates having a large Rabi force to make ESR-STM studies feasible. Another branch of research on single adatom magnetism has dealt with achieving long magnetic lifetimes, culminating in the discovery of Ho/MgO in 2016 [3]. Combining these two fields of research, Natterer *et al.* [38] applied CW-ESR to Fe atoms as sensors to sense the stray field of Ho/MgO and thereby further demonstrate its stability. Building onto these results, we used a mix of inelastic transport measurements, ESR-based sensing and single atom manipulation to investigate top-site Dy/MgO. The study was partially motivated by unpublished X-ray measurements showing complex magnetic behaviour and long magnetic lifetimes. Furthermore, unlike for Ho, several different common isotopes of Dy with different nuclear spins I exist (natural abundances are approximately 2% ^{160}Dy with $I = 0$, 19% ^{161}Dy with $I = 5/2$, 25% ^{162}Dy with $I = 0$, 25% ^{163}Dy with $I = 5/2$, and 28% ^{164}Dy with $I = 0$), potentially allowing for finding isotope dependent magnetization dynamics. Lastly, although not presented in detail here, we briefly tried to investigate the magnetic properties of Dy/MgO in adsorption configurations beyond top-site, and briefly attempted without success to drive ESR on Dy/MgO.

In our experiments, we discover top-site Dy to be a single adatom magnet. It has several remarkable properties compared to Ho/MgO, making it by multiple metrics the most stable SAM found thus far. This chapter is based on a publication with equal authorship shared between Dr. A. Singha, Dr. P. Willke and the author [75]. The author was involved in all experiments and analysis thereof displayed in the following, unless explicitly mentioned otherwise.

4.1 Sample preparation and atomic manipulation

Experiments were carried out using a customized Unisoku USM1300 STM. In-situ deposition of adatoms and molecules is not possible. For FePc, this presented no problem, since the molecules could be evaporated onto a room temperature MgO/Ag(100) sample and would

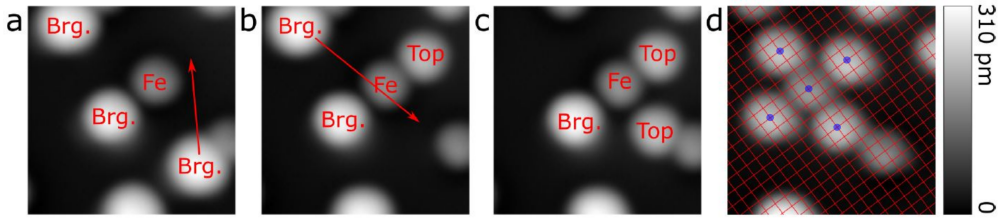

Figure 4.1: **Atom manipulation sequence**: **a,** Topographic images showing Dy and Fe adatoms as deposited on 2 ML MgO/Ag(100). **b-d,** The bridge-site Dy atoms were picked up and dropped off at a distance of 4 lattice sites towards the central Fe adatom, resulting in an atomically precise nanostructure (I = 20 pA, V_{DC} = 100 mV) [75].

readily stick to the MgO surfaces. Adatoms typically diffuse at elevated temperatures and form clusters or stick to step edges and defects, making the study of single adatoms impossible. However, a work-around exists on this machine. One can precool the transfer arm used for installation and removal of the tip and sample in the STM head, and for a short period of time (typically a few seconds only) move the cold sample to a preparation chamber and expose it to a Knudsen cell where atoms are being evaporated. The sample temperature hereby is at least 35 K, although possibly much higher. Nonetheless, when evaporating Dy, Fe and Ti adatoms, this procedure allowed creating samples of isolated adatoms on MgO.

When analyzing the Dy adatoms as deposited on 2 ML of MgO, practically all adatoms found are bridge-site Dy. They do not show any obvious magnetic signature when analyzed in direct spin transport measurements. In order to analyze top-site Dy, atom manipulation had to be carried out. Figure 4.1 shows a sequence of images where atom manipulation was carried out to create an atomically precise top-site Dy nanostructure starting from isolated bridge-site Dy adatoms. Dy atoms could be picked up under application of a negative bias voltage of a few hundred meV when approaching a relatively sharp tip beyond point contact. Dropoff was carried out by approaching the tip towards bare MgO under application of little to no bias voltage. In order to create well defined nanostructures with specific atom separations, the tip was centered atop of an atom (for example Fe), and then moved a chosen number of lattice sites away to the targeted dropoff position. Picking up Dy adatoms turned out to be highly efficient, with a success rate of almost 100%. Dropoff was slightly less efficient, but the whole sequence could simply be repeated if the resulting nanostructure did not meet the initial requirements. Hence, it became possible to create top-site Dy and well defined nanostructures thereof.

4.2 Spin-flip spectroscopy and multiplet calculations

Similar to Ho/MgO [38], using a spin-polarized STM tip, the magnetic state of top-site Dy (in following labelled simply as Dy) can be read out using an SP tip, and can be manipulated using tunneling electrons of sufficiently high energy. Figure 4.2 shows magnetic two-state

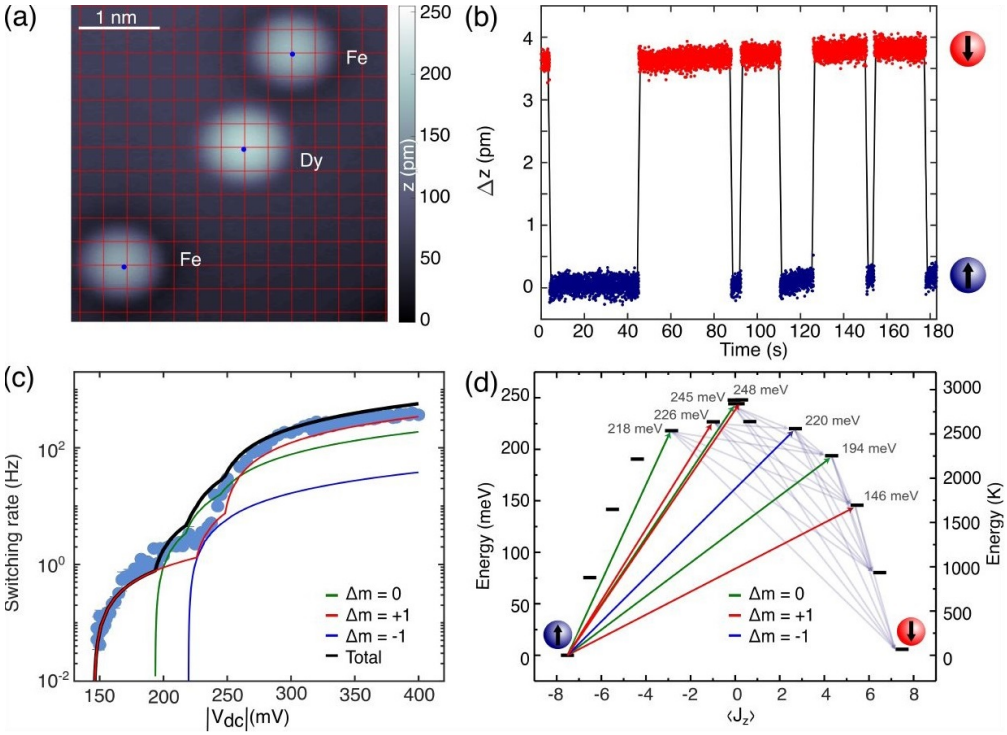

Figure 4.2: **STM induced magnetization reversal and multiplet structure**: **a,** Topographic image of a 2 ML MgO surface with individual Fe and Dy atoms atop (I = 20 pA, V_{DC} = 100 mV, T = 0.7 K). **b,** Magnetic two-state switching observed on top-site Dy (I = 1.5 nA, V_{DC} = −156 mV, T = 1.8 K, B_z = 5 T). **c,** Switching rate as a function of the DC voltage. The displayed switching rate spans four orders of magnitude and was acquired at 1.5 nA (150-250 mV), 0.15 nA (250-320 mV), and 0.015 nA (315-400 mV), and for comparability rescaled by factors 1, 10, and 100, respectively. The solid lines represent calculated switching rates based on the multiplet calculations and the heuristic two-step switching model (T = 1.8 K, B_z = 5 T). **d,** Calculated multiplet structure. Green, red and blue arrows mark excitation processes followed deexcitation processes (in grey) leading to the magnetization reversals. The Δm refers to the change in angular momentum of the tunneling electron [75].

switching and the calculated multiplet structure to explain the observed behaviour. The magnetic contrast is relatively low compared to Dy on graphene/Ir(111) [76] and switching amplitudes of a few picometers are observed, similar to Ho/MgO. The voltage dependence shows discrete switching thresholds as for Ho/MgO, and no switching below these thresholds. First switching is observed around 150 meV, and the final threshold lies around 250 meV. Both these values are about twice as high compared to the equivalent values in Ho/MgO, indicating an effective anisotropy barrier (as measured in inelastic transport experiments) twice as high as in the case of Ho.

In order to rationalize the observed behaviour, multiplet calculations and a heuristic switching rate model were employed by Prof. F. Donati. Details can be found directly in ref. [75].

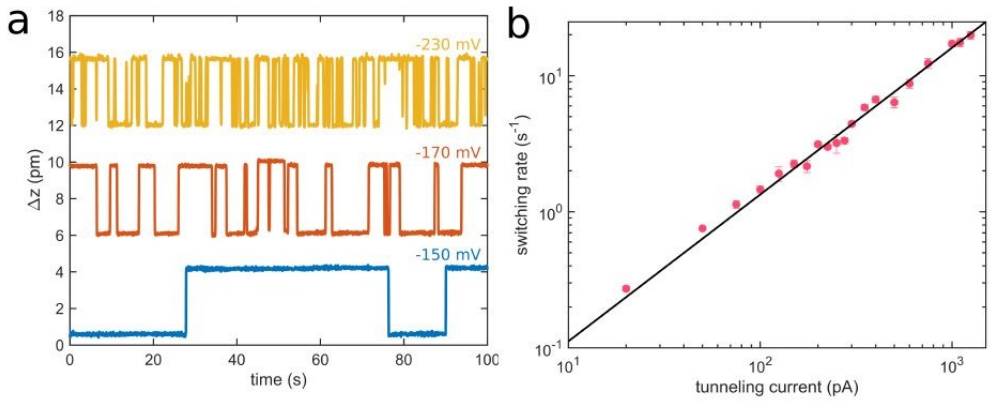

Figure 4.3: **Exemplary two-state switching traces and current dependence**: **a,** Time traces showing the two-state switching at different bias voltages (I = 1.5 nA, T = 1.8 K, B_z = 5 T). **b,** Switching rate as a function of current showing an (almost) linear dependence. The fit (black) follows eq. 4.1 (V_{DC} = −230 mV, T = 1.8 K, B_z = 5 T) [75].

The switching rate model is fundamentally a single-excitation two-step model, where the Dy angular momentum starts out in the ground state doublet and is excited by a tunneling electron. After the initial excitation, the angular momentum relaxes to a lower state with transition probabilities being based on the transition matrix elements obtained from the multiplet calculations. If, after this second step, the angular momentum has opposite sign compared to the initial step, a switching is recorded. This model naturally leads to the switching rates being linearly dependent on the current and will show discrete thresholds whenever the energy of the tunneling electrons allows for excitation towards angular momentum states where subsequent sub-barrier tunneling of magnetization or reversal across the top of the barrier is likely. The multiplet calculations use as an input the DFT derived atomic positions for Gd/MgO [50], although the atomic positions were later adjusted manually to lead to a better agreement with the observed data. The calculated multiplet structure shows an energy barrier of 248 meV, again confirming the significantly increased energy barrier compared to Ho/MgO. It also indicates a 9-fold charge occupancy of the $4f$ orbital, since for comparable atomic positions, the energy barrier of a $4f^{10}$ occupation is approximately a factor 2 lower due to the smaller expected radii of the $4f$ orbitals leading to a weakened interaction with the surrounding charges, and hence a weaker crystal field. Due to the strong uniaxial crystal field terms and the minor off-diagonal terms, top-site Dy with $4f^9$ charge occupancy has an almost pure half-integer $J_z = \pm 15/2$ ground state doublet with suppressed quantum tunneling of magnetization, which again is not the case for Ho/MgO [77]. Figure 4.3 takes a more detailed look at the switching rates observed in SP transport measurements, which was analyzed by Dr. P. Willke. Specifically, we find the switching rate to be approximately linear in current, in agreement with the single-electron process assumption of the model explained above. The current dependent switching rates are fitted according to

$$\Gamma = a \times (I/I_0)^N \tag{4.1}$$

	5 T (−230 mV)	5 T (+230 mV)	0 T (+230 mV)
a (Hz)	$(9 \pm 4)\cdot 10^3$	$(14 \pm 12)\cdot 10^3$	$(1.2 \pm 1.4)\cdot 10^3$
N	1.08 ± 0.07	1.17 ± 0.12	1.11 ± 0.17

Table 4.1: Evaluation of the current dependent switching rates based on eq. 4.1.

using $I_0 = 1$ pA. The precise results are displayed in table 4.1. Upon closer inspection, however, we find the scaling to be slightly superlinear (N > 1), indicating the presence of multi-electron processes. These type of processes will be discussed in greater detail in the next chapter on Ho/MgO, where, upon closer inspection of the data available in ref. [38], a non-linear trend can equally be found.

4.3 Low- and zero-field ESR sensing

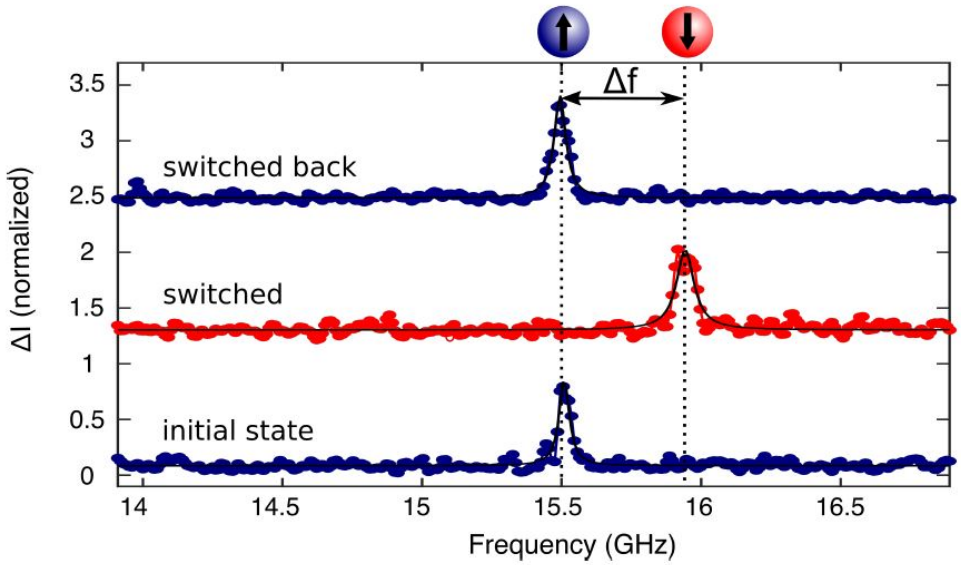

Figure 4.4: **Frequency sweep based sensing of the Dy magnetization**: The three traces are taken on an Fe atom separated by 1.82 nm from a nearby Dy atom. Voltages pulses with amplitudes larger than 150 mV were used to switch the Dy atom inbetween traces. Spectra are offset for clarity (T = 1.8 K, B_z = 0.125 T, B_x = 1.4 T, I = 20 pA, V_{DC} = 100 mV, V_{RF} = 15 mV) [75].

ESR-STM based sensing experiments used Fe adatoms to sense the magnetic stray field of nearby Dy atoms. Figure 4.4 shows frequency sweep based ESR measurements to sense the stray field of Dy atoms. Writing the effective magnetic field created by the Dy atoms as [15]

$$B_{Dy} = \frac{\mu_0 \mu_{Dy}}{4\pi} \times d^{-3} \tag{4.2}$$

where d denotes the distance between Fe and Dy, we find $\mu_{Dy} = 9.9\ \mu_B$, in agreement with the multiplet calculations. This type of measurement is equivalent to previous experiments

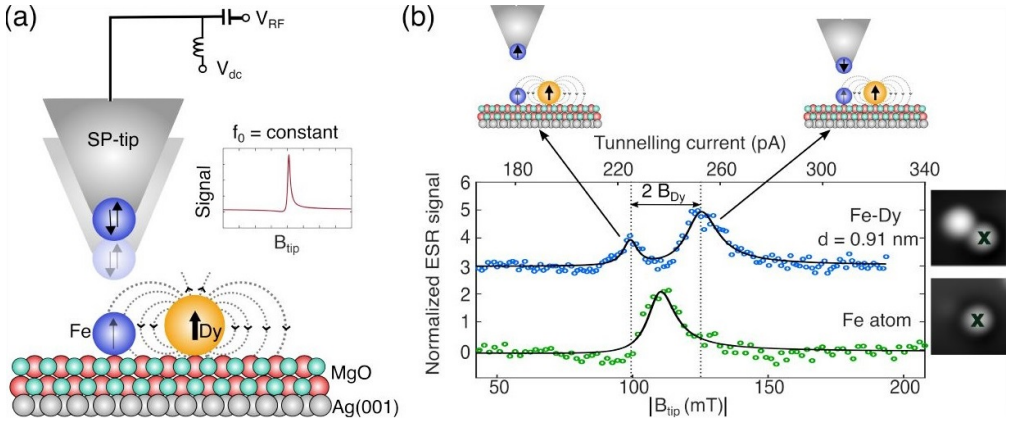

Figure 4.5: **ESR-STM based zero-field sensing**: **a,** Schematic of the ESR-STM based sensing experiments. **b,** Magnetic tip-field sweeps on an isolated Fe atom and on an Fe-Dy pair (ESR spectra: $B_{\text{ext}} = 0$ T, $T = 0.4$ K, $V_{\text{DC}} = -50$ mV, $V_{\text{RF}} = 27.5$ mV, $f = 16.38$ GHz; Topographic image: $T = 0.4$ K, $V_{\text{DC}} = 100$ mV, $I = 20$ pA, 2.5×2.5 nm^2) [75].

involving sensing of Ho [38] and Fe [15] using nearby Fe atoms. However, such experiments have been typically carried out at larger out-of-plane fields of ≈ 50 mT and above. Since, according to the multiplet analysis, Dy on the oxygen adsorption site on MgO should be significantly more stable than Ho/MgO even at low and zero external field, we extended this type of sensing experiment to the low- and zero-field regime. Zero-external-field ESR-STM based on tip field sweeps have been carried out before by Willke *et al.* [78]. However, no sensing experiments at low-to-zero external field have been reported.

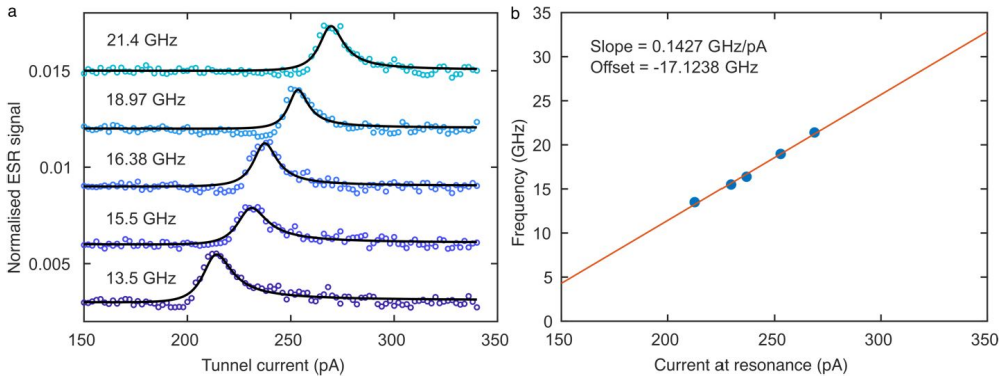

Figure 4.6: **Tip magnetic field calibration**: **a,** ESR spectra as a function of the tunneling current for different applied frequencies ($B_{\text{ext}} = 0$ T, $T = 0.6$ K, $V_{\text{DC}} = -50$ mV, $V_{\text{RF}} = 27.5$ mV, $f = 16.38$ GHz). **b,** Extracted resonance frequencies as a function of current (blue) and linear fit thereof (red) [75].

Figure 4.5 shows a schematic of the experiment as well as tip-field-sweep based zero-field ESR-STM sensing experiments. Tip-sweeps are more convenient in this context since it is fairly simple to sweep large parameter spaces, especially in light of the strong RF losses in the STM

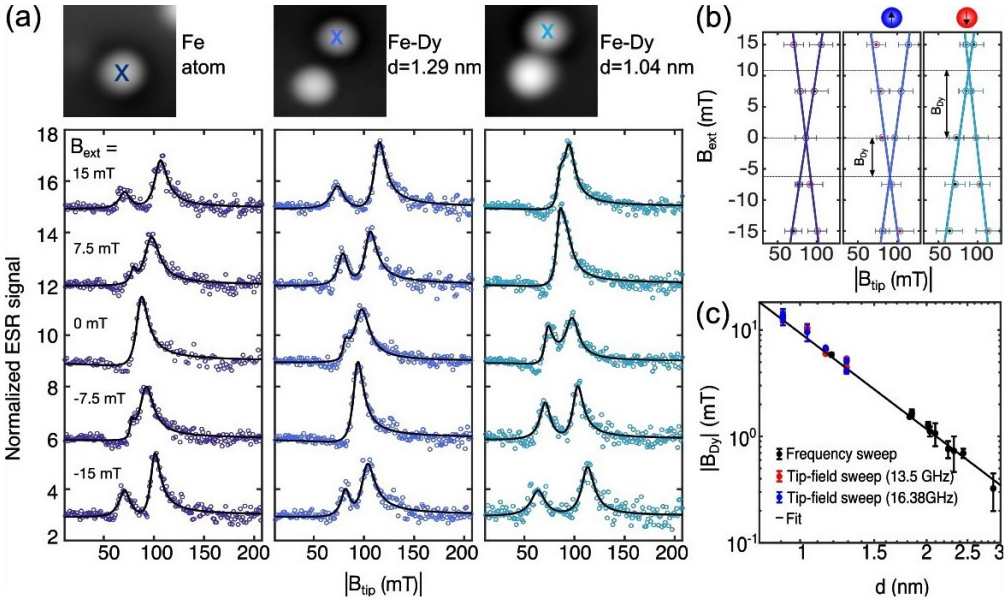

Figure 4.7: **Low field ESR measurements on isolated Fe atoms and Fe-Dy dimers**: **a,** Tip magnetic field sweep based ESR measurements within $B_{\text{ext}} = \pm$ 15 mT. The isolated Fe atom shows a single resonance at $B_{\text{ext}} = 0$ mT and two resonance of increasing peak seperation at finite fields. The Fe-Dy structures equally show a single peak but at a finite field due to the additional field generated by the nearby Dy atom (ESR spectra: $T = 0.5$ K, $V_{\text{DC}} = -50$ mV, $V_{\text{RF}} = 27.5$ mV, $f = 13.5$ GHz; Topographic images: $V_{\text{DC}} = 100$ mV, $I = 20$ pA, $T = 0.5$ K, 3×3 nm^2). **b,** Extracted resonance conditions as a function of the external and tip field. **c,** Effective Dy induced magnetic field as a function of the Fe-Dy separation as measured using frequency sweep based as well as tip field based ESR sensing [75].

used, as shown earlier in chapter 2. Calibration of the tip field is carried out by monitoring the resonance current as a function of the applied frequency as displayed in fig. 4.6 and assuming that the tip field varies linearly with current [79]. At zero field, we see a single resonance on isolated Fe atoms, but two resonances for an Fe atom with Dy nearby. Figure 4.7 shows the same measurements but at 0, ± 7.5, and ± 15 mT. It can be seen that Fe-Dy structures also show single resonances, but only in a specific finite external field. We explain the resulting ESR-spectra on Fe using

$$\frac{h f_{\text{res.}}}{2\mu_{\text{Fe}}} = |B_{\text{tip}} + B_{\text{NN}} + B_{\text{ext}}| \tag{4.3}$$

B_{tip} denotes the tip magnetic field, B_{NN} the stray field of nearby magnetic adatoms following eq. 4.2, and B_{ext} the externally applied magnetic field.

First, the eq. 4.3 is applied to the well known case of an individual Fe atom ($B_{\text{NN}} = 0$). At zero external field ($B_{\text{ext}} = 0$), only a single resonance is found. Empirically, we typically find two resonances at finite magnetic fields below approx. 30 mT. This can be explained by assuming superparamagnetic bistability in the tip. In this case, there are two possible resulting values

for $|B_{tip} + B_{ext}|$ with opposite signs of B_{tip}, each leading to a distinct resonance. Hence, we expect a single resonance at zero field, and two resonances at finite (but low) fields. When increasing the external field, we typically find one of the two peaks starting to vanish, most likely due to an increased energy level splitting and therefore a depopulation of one of the two tip states. Note that some tips show extended magnetic lifetimes, as can be seen in fig. 4.8. In this case, the ESR-spectra can be acquired for each tip state individually. When averaging over the two different tip states, the result is again in agreement with the results found for a more rapidly switching STM tip.

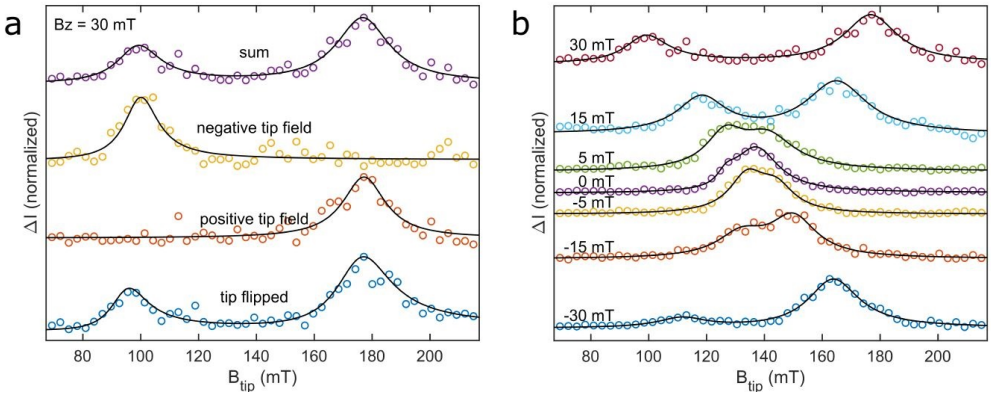

Figure 4.8: **Case of a slowly switching magnetic tip**: ESR-STM spectra on an Fe-Dy nanostructure with an atomic seperation of 1.15 nm. **a,** ESR spectra acquired at B_z = 30 mT. Most spectra for this microtip showed either only a positive or negative tip field relative to the external field, although in some cases the tip flipped during the experiment and both resulting peaks are visible. **b,** When averaging over all spectra, the same result is found as for a more rapidly switching tip. All traces are normalized and offset for clarity (T = 1.3 K, $V_{DC} = -50$ mV, V_{RF} = 15 mV, f = 21.4 GHz) [75].

Next, we look at the case where we have a nearby magnetic adatom such that $B_{NN} \neq 0$. If the nearby adatom shows a stable magnetic stray field, we expect a single resonance if and only if $B_{NN} = B_{ext}$. This is again in agreement with the data displayed in 4.5, where Fe-Dy structures in both cases show a single resonance at a finite field where this condition is met. At any other field, we find two resonances, similar to the case of the isolated Fe atom. Figure 4.9 shows the case where the nearby atom generating the stray field is given by another Fe atom. The lifetime of Fe/MgO ($\approx \mu$s to ms [7, 28]) is well below the timescale of the measurement ($\approx$ s), and hence B_{NN} takes on two different values of opposing sign. Therefore, one would expect four resonances at most fields, three resonances when $|B_{NN}| = |B_{ext}|$, and two resonances at zero field according to eq. 4.3. Again, this is in good agreement with the experiment.

The above mentioned results already demonstrate the magnetic stability of Dy in low- and zero field. Despite sweeping the magnetic field across zero, we have never observed any switching of the Dy atom. The proof is fundamentally given by the sign of the offset of

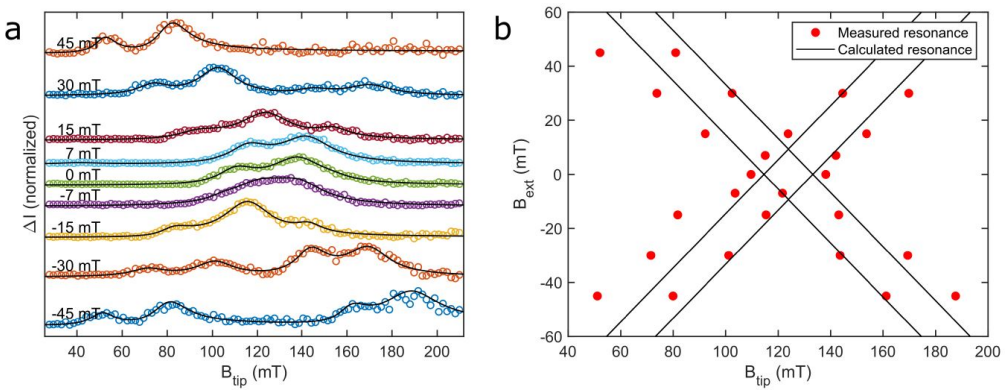

Figure 4.9: **Low-field sensing on an Fe-Fe dimer**: The magnetic lifetime of Fe at the given measurement condition is much faster ($\approx \mu$s) than the time scale of measurement. Hence, the effective magnetic field induced by the nearest neighbour atom can take on two discrete values of opposing sign and is given by $B_{\mathrm{NN}} = \pm|B_{\mathrm{Fe}}|$. **a,** Low-field sensing experiment in $\pm$ 45 mT. Due to the unstable neighbouring atom, up to four peaks are visible. As a side note, the depopulation of one of the two tip magnetic states at 45 mT is clearly visible, and one recuperates the well known high-field sensing result of seeing only two peaks [15] (T = 1.7 K, $V_{\mathrm{DC}} = -50$ mV, V_{RF} = 15 mV, f = 16.25 GHz). **b,** Extracted resonance conditions as a function of the external field. The calculated resonance condition (black) is based on equation 4.2 and assumes μ_{Fe} = 5.44 μ_{B} and uses the Fe-Fe separation of 0.81 nm found in this dimer [75].

the single-resonance condition, whereby the offset in this case stands for the external field required to compensate the Dy field. If the Dy atom switches, we would equally expect the sign of the offset to switch, which has never been observed. However, at exactly zero external field, we would for both signs of the nearby Dy atom expect the same result. In order to test the long-term low- to zero-field stability of Dy, as well as to demonstrate the capability to engineer atomically precise nanomagnets using Dy even in the absence of an external field, larger Fe-Dy nanostructures have been prepared. Figure 4.10 shows zero-field ESR sensing experiments on Fe atoms with up to 4 Dy neighbours. In this case, all Dy atoms were separated from the Fe by 4 MgO lattice sites (1.15 nm). If Dy was unstable at zero field, we would expect $N+1$ resonances for $N > 1$ nearest neighbour Dy atoms. However, in all measurements with nearby Dy atoms, we find exactly two resonances, underlying the extraordinary stability of Dy SAMs. The state of the Dy atoms can be controlled through voltages pulses, yielding the possibility to use Dy atoms to engineer nanoscale scale magnetic field with atomic precision.

Ultimately, we briefly investigated the thermal stability of Dy SAMs. We monitored the magnetic state of 6 Dy atoms before and after heating the sample to 10 K and 15 K, respectively, in an applied field of 5 T. Applying a large magnetic field typically facilitates direct phonon and Orbach relaxation. In both cases, we found no switching of the Dy atoms, further underlying the extraordinary magnetic stability of Dy.

A downside of this type of study is that due to the fact that these experiments only monitor a small amount of Dy atoms at the same time, and in combination with the very long lifetimes of Dy atoms, obtaining quantitative results on the temperature and magnetic field dependent magnetization dynamics is extremely tedious and has not been carried out here. A future study, possible in combination with X-ray based ensemble measurements, could shed further light on these properties in a more quantitative fashion.

4.4 Conclusion and outlook

In summary, we have found Dy/MgO to be a SAM. Compared to Ho/MgO, we have found several remarkable properties, such as zero-field stability and the two-fold increased anisotropy barrier. We were able to carry out atomic manipulation and create atomically precise nanostructures. The combination of the fact that Dy/MgO is a stable magnet, and that we can position these atoms onto adsorption sites of our choice, enables us to create atomically controlled local magnetic fields. Such fields could be used for example in ESR-measurements to add another degree of freedom allowing to investigate subspaces with reduced decoherence in coupled spin systems [41]. Having understood the fundamental properties of Dy/MgO, future work may take a more quantitative look at the intrinsic thermal and magnetic field stability of Dy/MgO. Equally, in our study we have not observed any fingerprint of the nuclear spin. A larger study of Dy with a greater number of atoms monitored and across larger time spans could potentially uncover hyperfine induced magnetization dynamics.

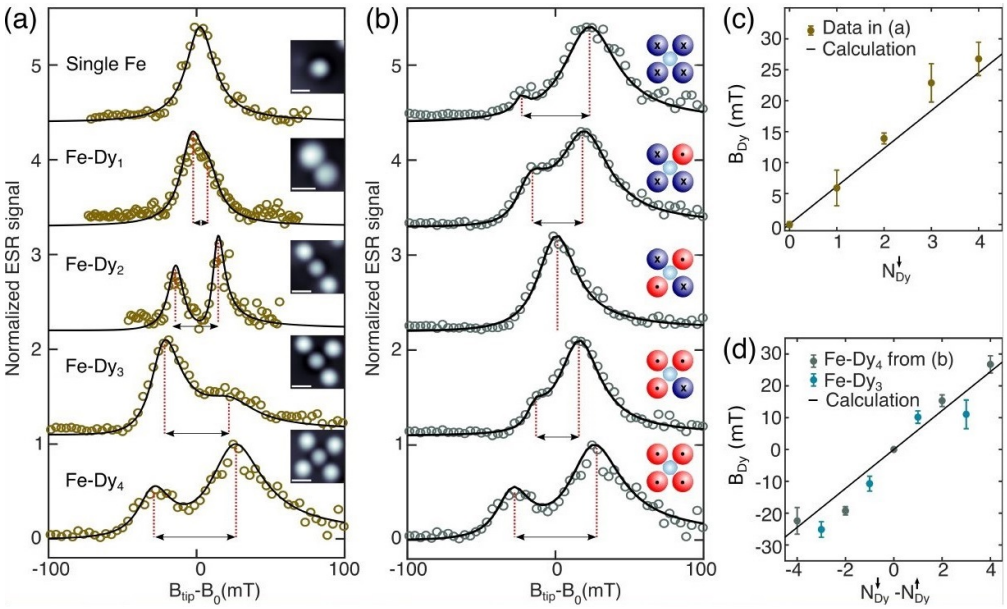

Figure 4.10: **Atomic scale engineering of local magnetic fields**: Using atomic manipulation and the magnetic stability of Dy, atomically precise Fe-Dy nanostructures with controllable local magnetic fields can be created. **a,** Zero-field ESR spectra on Fe with zero to four Dy neighbours separated by four O lattice sites (1.15 nm). The magnetic orientation of all Dy atoms was aligned, and therefore the peak separation increases with increasing number of neighbouring Dy atoms. Note that these measurements were taken with three different STM microtips. This leads to different linewidths and resolutions in some of the spectra (Fe-$Dy_{N=0,1,3,4}$: T = 1.3 K, V_{DC} = −50 mV, V_{RF} = 15 mV, f = 21.4 GHz; Fe-Dy_2: T = 0.8 K, V_{DC} = −50 mV, V_{RF} = 10 mV, f = 16.25 GHz). Insets show topographic images (scale bar: 1 nm; Fe-$Dy_{N=0,1,2,3}$: T = 1.3 K, V_{DC} = −100 mV, I = 20 pA; Fe-Dy_4: T = 1.3 K, V_{DC} = −80 mV, I = 20 pA). **b,** Zero-field ESR spectra of Fe-Dy_4, whereby iteratively the magnetic orientation of one Dy atom at a time was flipped (T = 1.3 K, V_{DC} = −50 mV, V_{RF} = 15 mV, f = 21.4 GHz). The inset shows a schematic indicating the relative orientations of the Dy atoms in each measurement. **c,** Effective magnetic fields induced by the neighbouring atoms shown in subfig. a. The calculation assumes a magnetic moment of 9.9 μ_B for Dy as determined in the high-field measurements. **d,** Effective magnetic fields found in Fe-Dy_3 and Fe-Dy_4 nanostructures when iteratively flipping one atom at a time [75].

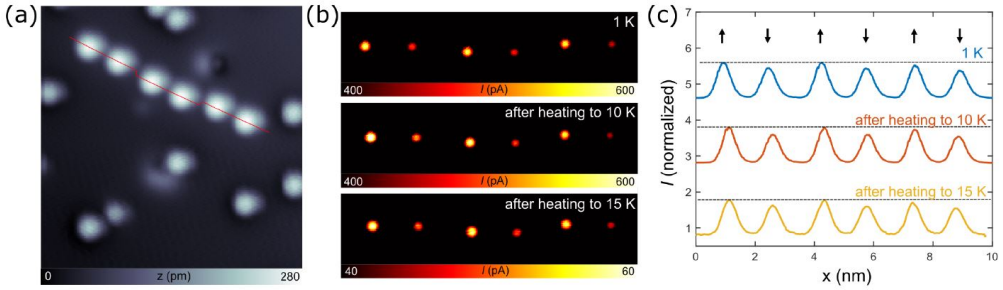

Figure 4.11: **Thermal stability at 5 T**: **a,** Topographic image showing a nanostructure of 6 top-site Dy atoms (T = 1.0 K, B_{ext} = 5 T, I = 20 pA, V_{DC} = −100 mV). **b,** Topographic images of the structure acquired using an SP tip after subsequently heating the sample to 10 and 15 K, respectively. **c,** Line profiles across the nanostructure. The apparent atomic height indicates the magnetic orientation of the Dy atom due to tunnel magnetoresistance. Despite the heating, no magnetic switching was observed [75].

5 Magnetization dynamics in Ho/MgO

This section is based on the following manuscript currently in preparation for publication:

- **Title**: Non-equilibrium magnetization dynamics in mixed-symmetry Ho spin ensembles
- **Authors**: Tobias Bilgeri, Stefano Rusponi, Christoph Wolf, Aparajita Singha, Denis Krylov, Safa L. Ahmed, Marina Pivetta, Alessandro Barla, Andreas Heinrich, Harald Brune, Fabio Donati
- **Author contributions**: F.D., H.B., and S.R. conceived the experiment. F.D., S.R., A.S., D.K., S.A., M.P., and A.B. carried out the measurements. F.D. and T.B. developed the model. C.W. carried out the DFT calculations. T.B. carried out all further calculations, analyzed the data and wrote the manuscript. H.B. and A.J.H. supervised the project. All authors discussed the results and contributed to the manuscript.

The manuscript fully reproduced below. Therein, we use a novel theoretical approach to explain the behaviour of Ho/MgO in previous STM and X-ray based measurements. Apart from re-evaluating some older measurements of top-site Ho, we also investigate the magnetic properties of bridge-site Ho, and specifically highlight the difference in their respective magnetization dynamics. We furthermore investigate in detail the influence of the experimental probe on the magnetization dynamics.

5.1 Abstract

Atomic and molecular spins provide promising building blocks for spintronic and quantum computing devices. Information processing requires controlling the internal dynamics via the chemical environment as well as ensuring addressability for external control. Here, we report on X-ray induced magnetization dynamics in ensembles of Ho atoms on MgO with different adsorption configurations. Depending on the ligand field symmetry, we find either single atom magnet behavior or short lifetimes due to efficient sub-barrier relaxation. In

particular, we find a non-equilibrium spin configuration resulting from X-ray absorption and subsequent scattering with secondary electrons. Spin dynamics invoking elevated spin states in the THz range lead to symmetry dependent spin temperatures up to more than 70 K higher than the environment. Our work demonstrates a novel approach for controlling the magnetic properties of spin ensembles and investigating non-equilibrium properties of quantum matter.

5.2 Main Text

Single lanthanide ions are a promising platform for classical [3, 38, 80, 81] and quantum information processing [82, 83]. Long lifetimes result from large uniaxial anisotropies in combination with a suppression of sub-barrier relaxation mechanisms [84–86], while quantum coherent operation often benefits from transversal crystal field and sub-barrier tunneling gaps [82, 87]. In recent years, single molecular magnets (SMM) with effective barriers up to 80 K [4] have been found, while some of the longest lifetimes to date were demonstrated in the single atom magnets (SAM) of Ho and Dy on ultrathin MgO films grown on Ag(100) [3, 38, 75]. The seminal SAM, oxygen top-site Ho/MgO (Ho^T), has been experimentally studied using a combination of X-ray absorption spectroscopy (XAS) and X-ray circular dichroism (XMCD) [3, 50, 88], as well as electron spin resonance (ESR) dipolar field sensing and spin polarized transport combined with scanning tunneling microscopy (STM) [27, 38, 56, 77]. At the same time, topographic STM studies show that bridge-site Ho (Ho^B) coexists on the same surface [55, 89]. Unlike Ho^T, the magnetic properties of Ho^B are unknown thus far. While the ligand field of Ho^T has C_{4v} symmetry, the low-symmetry environment of Ho^B leads to a C_{2v} crystal field. A low-symmetry environment is expected to lead to strongly superposed quantum states even at large magnetic fields and should result in low magnetic lifetimes. Concomitantly, it has been observed that magnetic systems with long intrinsic lifetimes show significantly increased relaxation rates under the influence of X-ray radiation [3, 90–92]. While it has been shown that this results from scattering with secondary electrons [90], no detailed analysis of the resulting spin dynamics has been shown to-date. Due to the existence of both high- and low-symmetry spin species, Ho/MgO presents an ideal platform to study the symmetry dependent magnetization dynamics of lanthanide ions in presence of multiple scattering mechanisms.

In this work, we study the magnetization dynamics in individual Ho adatoms in different ligand field symmetry configurations under the effect of an X-ray probe. X-rays generate secondary electrons scattering with the adatoms leading to non-equilibrium spin dynamics. By varying the sample temperature during Ho deposition, we create samples with majority spins in either top-site C_{4v} or bridge-site C_{2v} adsorption configurations. This allows investigating their respective symmetry dependent dynamical magnetization in detail. Our calculations combining density functional theory (DFT) derived crystal fields and facile quantum many body calculations [51], together with a master equation to model the dynamical magnetization

under the influence of different scattering mechanisms, explain the dynamical magnetic properties of Ho in different symmetry configurations in excellent agreement with the experimental data. We find rich out-of-equilibrium physics induced by scattering with Ho^T secondary electrons [90], which are similarly present in transport studies [38, 56]. The high-energy probe induces magnetization reversal via high-energy spin states both through classical over-barrier as well as quantum physical sub-barrier processes. The spin dependent relaxation pathways lead to a non-equilibrium quantum state population and the spin degree of freedom of the Ho species are driven out of thermal equilibrium by up to more than 70 K.

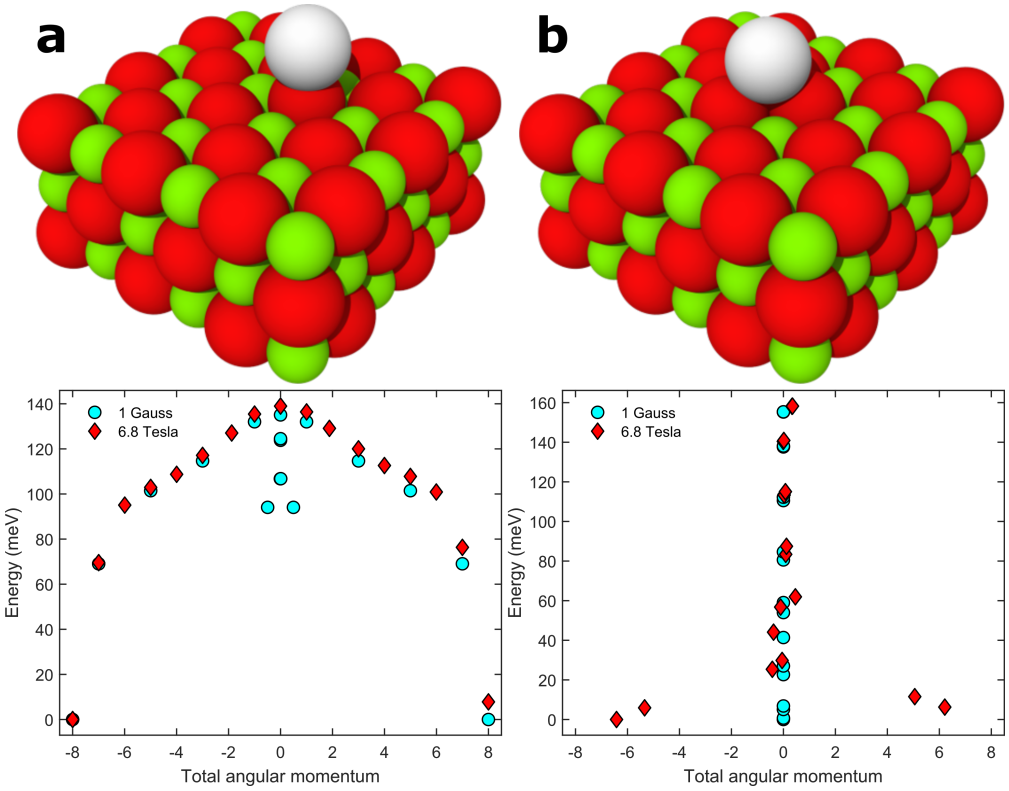

Figure 5.1: **Ho adatoms on MgO**: **a**, Schematic of the adsorption configuration and calculated anisotropy barrier of top-site Ho in high-symmetry C_{4v} on MgO/Ag(100). Most magnetic states are close to pure J_z states already at 1 Gauss due to the large uniaxial crystal field with only minor transversal terms, thereby preventing efficient sub-barrier relaxation. **b**, Bridge-site Ho in low-symmetry C_{2v} configuration shows strongly superposed angular momentum states even at large magnetic fields of 6.8 T allowing for substantial phonon-assisted tunneling of magnetization. Both energy diagrams assume $4f^{10}$ charge configuration.

Fig 1 shows schematics of Ho atoms adsorbed on an MgO thin film in two different symmetry configurations. The atomic lattice and charge states were calculated using DFT (see subsection 5.3.1). The relative atomic positions and effective Born charges of +2 e^- for O and -2 e^- for Mg directly yield the crystal field implemented through a point charge model [50, 57]. The

occupation of Ho valence states was recently determined as $5d^0 6s^2 6p^0$ [50]. For ultrathin MgO films on Ag(100), we find a charge transfer from the $4f$-orbitals to the silver resulting in a $4f^{10}$ configuration for the core states [50]. Based on this information, the X-ray spectra, energy level scheme, and the associated level transition probabilities can be calculated in Quanty [51] considering electron-electron correlations, spin-orbit coupling, the crystal field, and the Zeeman energy (see subsection 5.3.2) for magnetic fields up to 6.8 T as used in experiments.

Top-site Ho in C_{4v} symmetry corresponds to the well-known SAM [3]. The underneath O is displaced upwards by 60 pm following its strong chemical bond to Ho. This local reconstruction of the first MgO plane has also been found in earlier DFT calculations [3]. It increase the distance to the four next nearest Mg and O atoms, which lessens its electrostatic interaction with the other surface atoms and thereby leads to vanishing off-diagonal crystal field terms. This is reflected in the corresponding energy level diagram where, already at external fields of 1 Gauss, the ground state doublet is composed of $m_j = \pm 8$ states by more than 99%, leading to a suppression of direct sub-barrier relaxation. The calculated excited state energies and magnetic moment of 10 μB are in good agreement with previous STM measurements [27, 38, 56, 77] (see subsection 5.3.6).

Bridge-site Ho in C_{2v} symmetry resides between two O atoms. Due to the weak out-of-plane anisotropy and low symmetry, the angular momentum states are strongly mixed across the barrier allowing for efficient sub-barrier relaxation at all magnetic fields. While at 1 G we exclusively find singlet states with vanishing angular momentum, at 6.8 T we find $< m_j >$ = +6.41 and −6.21 within the ground state doublet. Hence, Ho^T and Ho^B serve as excellent model systems to study the influence of ligand field symmetry on the spin dynamics in the presence of low- and high-energy scatterers.

The X-ray measurements focus on the M5 edge involving electric dipole transitions from the closed 3d shell to the open $4f$ shell. Circularly polarized photons and angular momentum conservation allow for direct probing of the degree of spin polarization in the $4f$ orbital. Previous X-ray studies focused on Ho^T and disregarded the presence of other species in the spectral analysis, leading to discrepancies between X-ray and STM based result [3, 38, 56]. Experiments were carried out at the EPFL/PSI X-Treme beamline of the Swiss Light Source [93] at a base temperature of 2.5 K and at the Hector beamline of the ALBA synchrotron [94] at 6 K, using circularly polarized photons in both cases. The magnetic field was parallel to the incoming photons beam, either in normal incidence (NI) or grazing incidence (GI) at an angle of 60° with respect to the normal. Samples were prepared in UHV at a base pressure of 3×10^{-11} mbar and Ho atoms evaporated directly onto the cold sample. Figure 5.2 shows X-ray absorption spectra using right-polarized (RP) and left-polarized (LP) photons in NI and GI, as well as the circular dichroism, defined as the difference between the RP and LP spectra, for a sample grown at 10 K giving a majority of Ho^T. The fitted curves take into account different

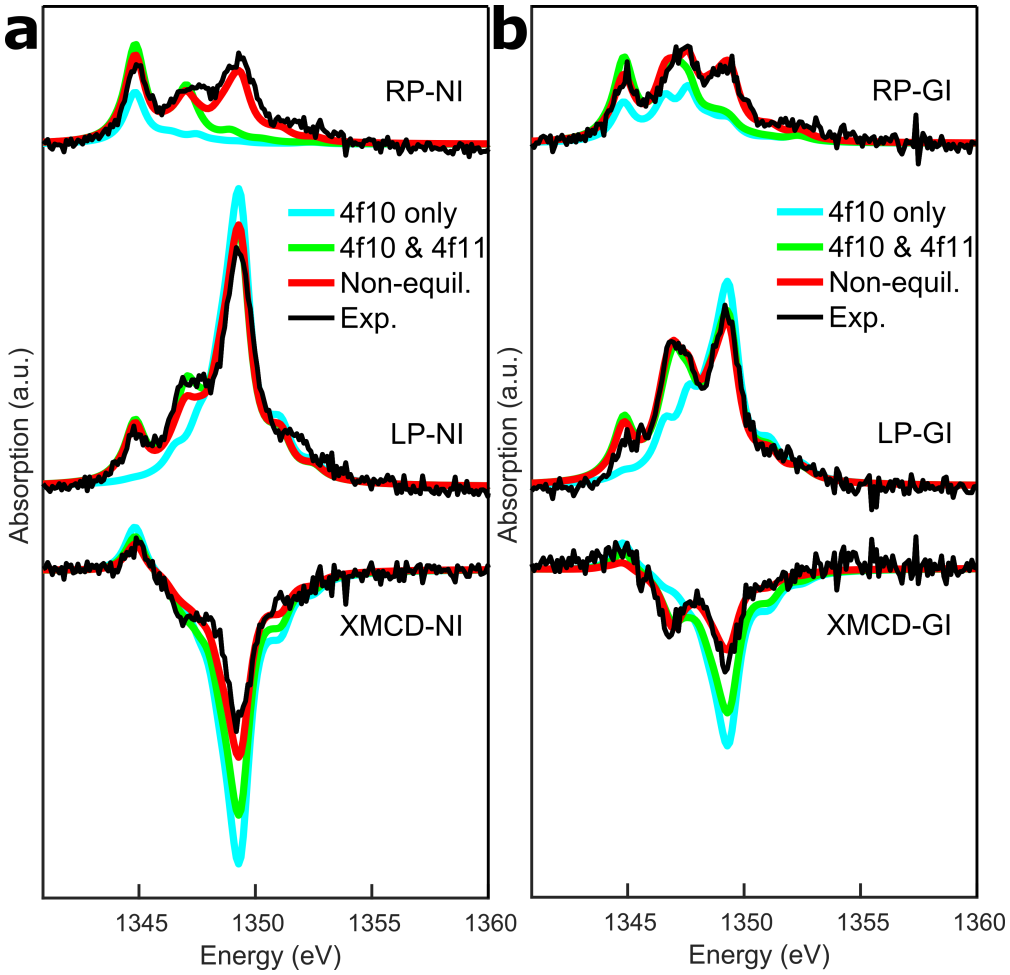

Figure 5.2: **Circularly polarized X-ray absorption of a majority Ho^{T} sample**: Spectra at the M5 edge at **a**, NI and **b**, GI for RP (top) and LP (bottom) photons. The XMCD shows the difference between RP and LP spectra and its peak area is proportional to the ensemble magnetization. Experimental data are plotted in black. Simulated curves consider different Ho adsorption sites and electronic configurations: (cyan) $4f^{10}$ Ho^{T} and Ho^{B} only, (green) $4f^{10}$ Ho^{T} and Ho^{B}, as well as $4f^{11}$ Ho^{T} and Ho^{B}, and (red) $4f^{10}$ and $4f^{11}$ species, and including the out-of-equilibrium spin temperature of the $4f^{10}$ species (relative occurrences in table 1; T = 2.5 K, B = 6.8 T, $\phi = 2.15\times10^{-2}$ photons nm^{-2}s^{-1}, T_{growth} = 10 K, Ho coverage Θ_{Ho} = 0.009 ML).

compositions of the Ho ensemble. Hereby the spectra per species φ_i are calculated using the DFT input and we fit the relative occurrence c_i resulting in the final spectra $\varphi_{\mathrm{tot}} = \sum_i c_i\varphi_i$. The cyan curves consider Ho^{T} and Ho^{B} in bulk-like $4f^{10}$ configurations. The relative occurrences are given in table 5.1.

It is evident that several peaks are not captured by this fit. The difference between NI and GI is too pronounced. The XMCD signal is strongly overestimated in both NI and GI, indicating a vast overestimation of the degree of magnetic polarization present in the sample. Since in par-

	$4f^{10}$ Top	$4f^{10}$ Bridge	$4f^{11}$ Top	$4f^{11}$ Bridge
Sample 1 (equilibrium, $4f^{10}$ only)	70 ± 19 %	30 ± 19 %		
Sample 1 (equilibrium)	46 ± 9 %	12 ± 9 %	10 ± 6 %	32 ± 7 %
Sample 1 (non-equilibrium)	61 ± 4 %	9 ± 3 %	15 ± 4 %	15 ± 4 %
Sample 2 (non-equilibrium)	36 ± 5 %	47 ± 4 %	2 ± 5 %	15 ± 5 %

Table 5.1: Composition of the spectra displayed in figs. 5.2 and 5.3. Sample 1 and 2 refer to the majority top-site and majority bridge-site samples, respectively.

ticular the spectral weight at 1347 eV in the signal can not be reproduced for any combination of $4f^{10}$ Ho^{T} and Ho^{B}, the green curve now considers additionally a free-atom-like $4f^{11}$ charge configuration on both adsorpon sites. Energetically, their main peaks in XMCD lie 2 eV below the main peak of the $4f^{10}$ species, which was also recently observed experimentally on metal surfaces and graphene [49, 95], and as is particularly visible in GI. Such a configuration can be expected on thicker MgO slabs, where a charge transfer to the Ag is less likely, and was equally found for Dy [96]. Variations in MgO thickness are expected within the X-ray spot size (≈ 1 mm2) due to the known coexistence of several thicknesses in MgO films [53]. Note that this approach is similar to including dynamic charge fluctuations observed in bulk systems containing lanthanide ions [60] albeit in a static fashion. For $4f^{11}$ spins we find no out-of-plane anisotropy in both adsorption site configurations (see subsection 5.3.3). They make up roughly 30% of the ensemble and including them leads to a much better agreement with the experiment. However, the dichroism and thus the degree of spin polarization is still overestimated, as in the RP spectra the experimental peak at 1349 eV can not be reproduced. One possible explanation would be a bad estimate of the spin multiplet of the $4f^{11}$ species. This seems unlikely, however, due to the good agreement between calculated and experimental STM results for Ho^{T} (see subsection 5.3.6).

These discrepancies can be removed by assuming an increased effective spin temperature due to scattering with secondary electrons, which reduces the equilibrium magnetization. Previously, it has been shown that the Ho^{T} secondary electrons produced through core hole Auger decay upon X-ray absorption reduced magnetic state lifetimes in systems with suppressed sub-barrier relaxation [90–92]. This effect manifests itself in photons flux ϕ dependent lifetimes of magnetic quantum states and has also been observed in $4f^{10}$ Ho^{T} [3]. In our experiments, ϕ was on the order of $\approx 10^{-2}$ photons $nm^{-2}s^{-1}$ and thus deep within the regime where the lifetime of the Ho SAM is flux limited [3, 88]. Such photons fluxes are necessary to resolve sub-monolayer spin ensembles at a density of ≈ 0.1 atom/nm^{-2}. In order to analyze the influence of X-ray induced scattering on different $4f^{11}$ Ho species, we model the occupation of magnetic quantum states using the Pauli master rate equation with two competing scattering processes:

$$\frac{dp_i}{dt} = \sum_{j=1}^{17} \left((\Gamma_{ij}^{\mathrm{ph}} + \Gamma_{ij}^{\mathrm{se}}) p_j - ((\Gamma_{ji}^{\mathrm{ph}} + \Gamma_{ji}^{\mathrm{se}}) p_i \right) \tag{5.1}$$

Hereby p_i represents the occupation of angular momentum state i, while $\Gamma_{ij}^{\mathrm{ph}}$ and $\Gamma_{ij}^{\mathrm{se}}$ denote the phonon and secondary electron induced transition rates. Eq. 5.1 introduces magnetization reversal pathways trough classical Orbach processes across the top of the anisotropy barrier, as well as through quantum mechanical sub-barrier transitions via scatterer assisted tunneling of magnetization [97–99]. We model the effect of secondary electrons as scattering with a high energy scatterer and direct phonon scattering using a Debye model [97] (see subsection 5.3.4). The quantum mechanical transition probabilities are derived using the quantum many body calculations described above. For $4f^{10}$ $\mathrm{Ho^T}$ at 6.8 T we have previously measured magnetization reversal rates $(\Gamma^{\mathrm{ph,T}})^{-1} \gtrsim 3690$ s and $(\Gamma^{\mathrm{ph,se}})^{-1} \approx (0.5nm^2 \times \phi)^{-1}$ at a given photons flux ϕ ($\mathrm{nm^{-2}s^{-1}}$) [3]. While we find the spin-phonon scattering to be much more frequent by a factor $\approx 10^3$ at typical experimental parameters, the efficient suppression of sub-barrier magnetization reversal via low-energy scattering processes very quickly leads to a regime where the secondary electron induced scattering dominates. This effect was found to be particularly prominent at MgO film thicknesses $\lesssim 4$ ML [3], which in future could be used as an additional degree of freedom to probe SAMs and SMMs on insulating thin films. Assuming the spin-scatter couplings for $\mathrm{Ho^B}$ to be on a similar scale, we find for this species an intrinsic lifetime on the order of nanoseconds and a negligible effect of the secondary electrons on the reversal rate at typical fluxes close to 10^{-2} $\mathrm{nm^{-2}s^{-1}}$. This is a straight forward result of the strongly superposed angular momentum states allowing for efficient sub-barrier tunneling via low-energy spin-phonon scattering. Therefore, as opposed to $\mathrm{Ho^T}$, intrinsic relaxation dominates for the low-symmetry $\mathrm{Ho^B}$. Consequently, $\mathrm{Ho^B}$ tends to be close to the thermal equilibrium. In order to find the effective temperature, we compare the average occupation of the ground state doublet in the steady-state limit to a Boltzmann distribution $p_2/p_1 = \exp((E_1 - E_2)/(k_{\mathrm{B}} T_{\mathrm{eff}}))$. We find an effective temperature of 75.6 K for $\mathrm{Ho^T}$ at a photons flux of 2.15×10^{-2} $\mathrm{nm^{-2}s^{-1}}$, while for $\mathrm{Ho^B}$ we find 6.2 K. Revisiting the experimental data by taking into account the effective temperatures leads to the red curve in fig. 5.2. The theoretical curve is in excellent agreement with the experimental data since the previously observed excess magnetic polarization is now compensated by the photons induced spin heating. The sample is composed of 61% $4f^{10}$ $\mathrm{Ho^T}$, 9% $4f^{10}$ $\mathrm{Ho^B}$, 15% $4f^{11}$ $\mathrm{Ho^T}$ and 15% $4f^{11}$ $\mathrm{Ho^B}$. This immediately removes the discrepancy between previously determined magnetic moments. While for individual $4f^{10}$ $\mathrm{Ho^T}$ we find a magnetic moment of 10 μB in agreement with previous ESR-STM results [38], we find a fitted average ensemble angular momentum $< m_j > = 3.1$ close to values found in previous XMCD measurements [3]. The non-equilibrium approach also holds true for spectra obtained at elevated temperatures (see subsection 5.3.5).

To further investigate the adsorption site symmetry dependent magnetic behavior, we have prepared samples with different majority spin species. Figure 5.3a shows again the sample with dominant high symmetry contribution. Here, the Ho atoms were evaporated onto the cold sample at a temperature of 10 K which lead to a majority top-site sample. For the sample displayed in fig. 5.3b, this temperature was raised to 80 K. Based on a previous topographical STM study, this is expected to significantly increase the fraction of low-symmetry $\mathrm{Ho^B}$ [55].

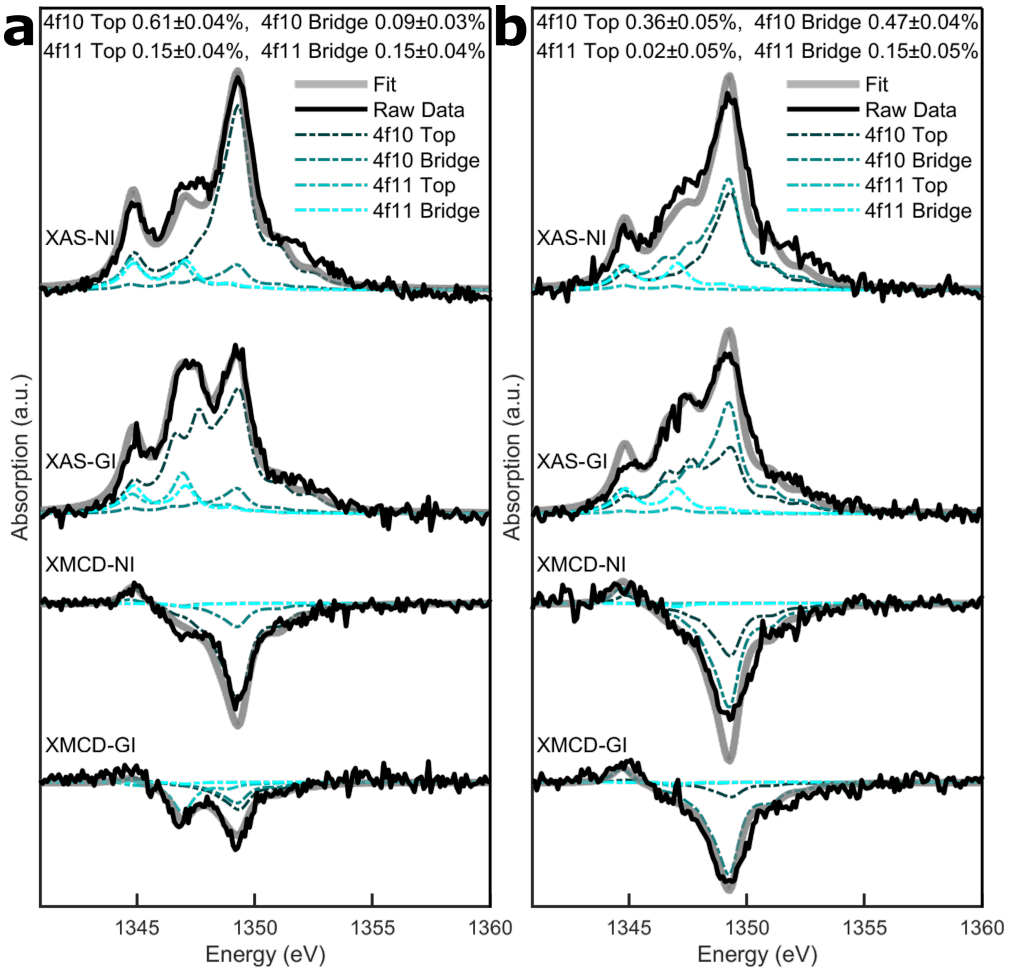

Figure 5.3: **Two samples with varying adsorption site populations**: **a**, $4f^{10}$ Ho^{T} majority sample (T = 2.5 K, B = 6.8 T, $\phi = 2.15\times10^{-2}$ nm^{-2}s^{-1}, T_{growth} = 10 K, Θ_{Ho} = 0.009 ML). **b**, $4f^{10}$ Ho^{B} majority sample ($\phi = 1.1\times10^{-2}$ nm^{-2}s^{-1}, T_{growth} = 80 K, Θ_{Ho} = 0.013 ML). Displayed on the top are the relative occurrences of different adsorption sites and electronic configurations.

The displayed XAS spectra sum over both LP and RP contributions and, together with the XMCD spectra, allow disentangling magnetic and non-magnetic contributions to the photons absorption. Notably the difference between NI and GI is now strongly reduced due to the small anisotropy in $4f^{10}$ Ho^{B} compared to Ho^{T}. The $4f^{11}$-population also shrank, likely due to an increased clustering and degradation of the sample leading to higher coordination, which favors the $4f^{10}$ configuration [100], and likely also explains the slight overestimation of the XMCD signal (see subsection 5.3.5). We now find 36% $4f^{10}$ Ho^{T} and 47% $4f^{10}$ Ho^{B}, and our simulated spectra are again in good agreement with the experimental data.

To further corroborate our analysis, we measure the field-dependent non-equilibrium magnetization dynamics of the $4f^{10}$ species by probing the main XMCD peak at 1349 eV and sweeping the external magnetic field. Note that the $4f^{11}$ species have almost no amplitude at

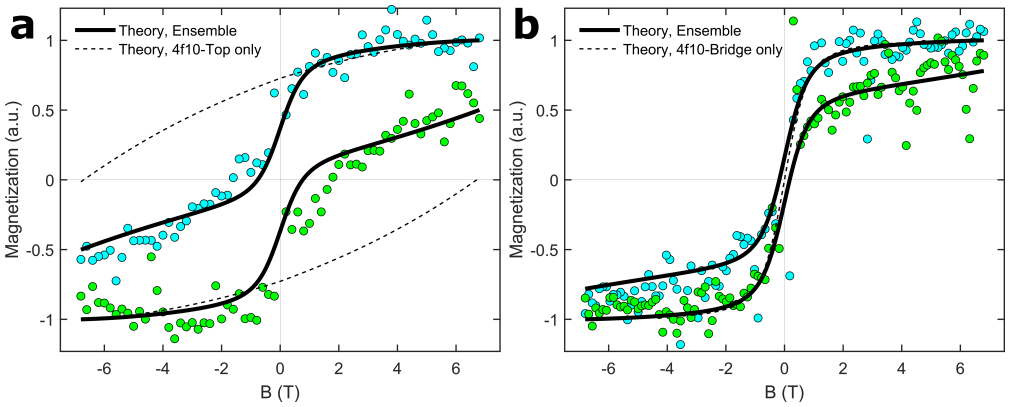

Figure 5.4: **Adsorption site dependent magnetization dynamics**: **a**, Majority high-symmetry $4f^{10}$ Ho^{T} sample (Θ_{Ho} = 0.009 ML). **b**, Majority low-symmetry $4f^{10}$ Ho^{B} sample (T = 2.5 K, dB/dT = 33 mT/s, $\phi = 1.1\times10^{-2}$ nm^{-2}s^{-1}, Θ_{Ho} = 0.013 ML).

1349 eV and play no role here. Figs. 5.4a and 5.4b show the resulting hysteresis loops of the previously analyzed $4f^{10}$ Ho^{T} and Ho^{B} majority samples. As expected, the former shows a giant and persistent hysteresis, while the latter consists mostly of rapidly relaxing Ho^{B} atoms with a finite hysteresis remaining due to the presence of Ho^{T}. The theoretical curves are in good agreement with the experimental data. The magnetization curves were calculated using eq. 5.1 for a non-stationary field and separately per Ho species (see subsection 5.3.4). The magnetization is calculated using the product of the time and field dependent population and angular momentum across all quantum states. The final hysteresis loop uses the sample composition determined earlier, although in both measurements we find a reduction of the Ho^{T} species by ≈ 18%. We expect this change in adsorption site abundance to result from the lengthy exposure of the surface during extended measurements, as was also observed in subsection 5.3.5. Temperature dependent XAS, XMCD and magnetization spectra also show a good agreement between theoretical and experimental curves (see subsection 5.3.1).

Finally, we analyze which relaxation paths lead to the observed non-equilibrium behaviour (see subsection 5.3.6). For Ho^{T}, this corresponds to climbing up the spin ladder in a multi-electron process and ultimately phonon-assisted tunneling via states approximately 100 to 120 meV above the ground state doublet, which we also find present in previous STM experiments [38, 56]. These states can only be reached in the presence of a high-energy scatterer, which in consequence leads to the elevated spin temperature. In Ho^{B}, the most important mechanism of reversal is the direct phonon transition within the ground state doublet independent of the secondary electrons, which leads to the observed ultrafast relaxation even at low temperatures.

In summary, we have introduced novel approaches to tune and analyze the magnetic properties of single magnetic atom ensembles. We identify a novel spin scattering mechanism leading to varying spin temperatures of the Ho species depending on the symmetry of their adsorption

site. The strongly selective relaxation pathways of certain excited angular momentum states, in combination with relatively large excitation energy, may allow for efficient spin initialization using THz sources and potential quantum coherent measurements at elevated temperatures [101–103]. Equally, we believe that studying non-equilibrium dynamics and thermalization in a similar fashion via resonant X-ray absorption should be possible in a larger class of materials with long lived metastable states or in combination with faster probes [104, 105]. Regarding the seminal SAM Ho^T, our heterogeneous ensemble approach is able to relieve the discrepancies between local (STM) and ensemble-averaging (X-ray) experimental studies. All calculations were carried out using a relatively straightforward theoretical approach without the need for extensive tuning of a large set of parameters. We have recently used a similar approach for Dy/MgO [75] and achieved similarly good agreement with experiment. Therefore, we believe that easy, predictive modeling for lanthanide SAMs guiding future experiments will be possible.

5.3 Supplementary Information

5.3.1 Details of Density Functional Theory calculations

All calculations were performed with version 6.6 of Quantum Espresso [106] which implements density functional theory (DFT) using pseudopotentials and plane-wave basis. The pseudopotentials were chosen according to the SSSP precision table and use the generalized gradient approximation (GGA) [107, 108]. Integration of the Brillouin zone was performed on a 3×3×1 Monkhorts-Pack grid with a cutoff of 60 Ry for the kinetic energy and 600 Ry for the charge density. To model the system we placed a single Ho atom on 4 ML of Ag (100) and 2 monolayer of MgO, fixed at the lattice constant of bulk silver (a = 4.16) expanded in 3×3 surface cell and padded by 10 Å of vacuum in z-direction. This leads to roughly 1 Ho atom per 1 nm2 surface area. The system was then relaxed until all forces were less than 0.02 eV/Å.

To account for limitations of GGA to accurately describe the highly localized $4f$ and $5d$ shells we applied a Hubbard U correction of 9 eV to both states [109]. We note that applying a Hubbard correction to the empty 5d states is not technically necessary but it removes spurious interactions between the 5d and 6s shells making it easier to analyze the final charge state. The final charge state of Ho on Ag/MgO is similar to a nominally singly charged Ho atom (Ho+1), indicating a charge transfer from Ho to the silver substrate. To obtain the geometry of the neutral species (Ho+0) we removed the silver from the system before relaxation thereby suppressing the charge transfer.

For the adsorption energies we find a preference for O-top site absorption of around 30 meV (for details see table 5.2).

Species/substrate	ΔE (meV) (Top-Bridge)
Ho^{+0}/MgO	-320
Ho^{+1}/MgO	-350
Ho/Ag/MgO	-440

Table 5.2: Energy difference between top and bridge site adsorption of Ho and Ho^{+1} calculated for the indicated substrate.

Ion	Charge	$d_\perp$	$d_\parallel$
O (underneath)	-2e	213, 221	0, 0
Mg	+2e	276, 273, 248, 251	213, 213, 157, 157
O	-2e	275, 273, 173, 203	294, 294, 139, 139

Table 5.3: Point charges and their spatial distribution. The distances are given in pm for top-site Ho $4f^{10}$, $4f^{11}$, bridge-site Ho $4f^{10}$, and $4f^{11}$.

Born effective charges for MgO were obtained from a density functional perturbation theory (DFPT) calculation as implemented in Quantum Espresso.

5.3.2 Details of multiplet calculations

The electron-electron interactions has been calculated using Cowan's atomic structure code [110] and have been rescaled by 0.76 to fit the experimentally observed spread of the peaks within the M4 edge. The spin-orbit coupling has been rescaled by 0.98 to fit the observed M4-M5 edge splitting. The crystal field has been calculated based on the methods outlined in [50, 57, 75] and using the point charge distribution calculated via DFT, see table 5.3, in Quanty [51]. The final X-ray spectra is given by a weighted sum over the spectra of the individual species. Since the orientation of the sample is in general not known, we use an azimuthal angle of 45° with respect to the MgO lattice for all calculations.

5.3.3 Magnetic ground state of $4f^{11}$ Ho

As mentioned in the main text, $4f^{11}$ Ho shows no out-of-plane anisotropy and favors a low angular momentum ground state for both symmetry configurations. While the adsorption configuration and hence the crystal fields are very similar compared to the $4f^{10}$ cases as described in table 5.3, the orbital shapes and therefore the favored total angular momentum change upon addition of another electron to the 4f orbital [61]. $4f^{11}$ Ho^{T} shows a finite in-plane anisotropy, as can be seen in the XMCD-GI spectra in fig. 5.3. The calculated energy barriers in an out-of-plane magnetic field are displayed in fig. 5.5.

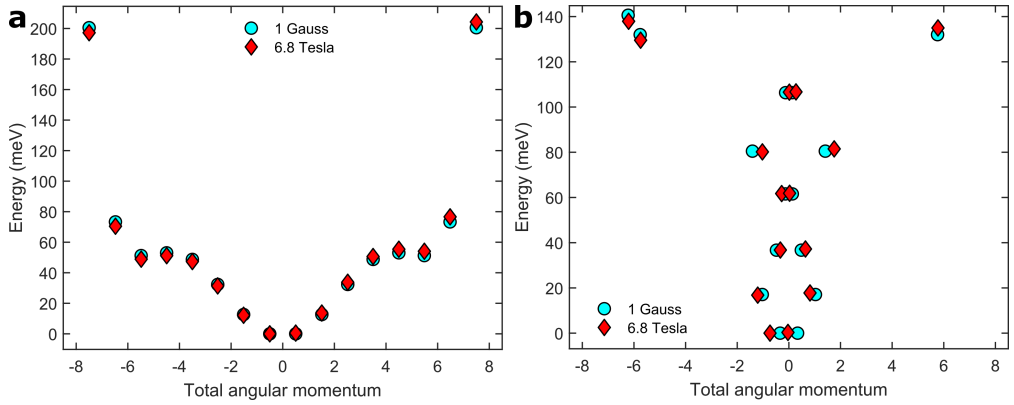

Figure 5.5: **Anisotropy barriers in 4f^{11} Ho**: **a**, Top-site Ho **b**, Bridge-site Ho. The magnetic fields are oriented perpendicular to the surface.

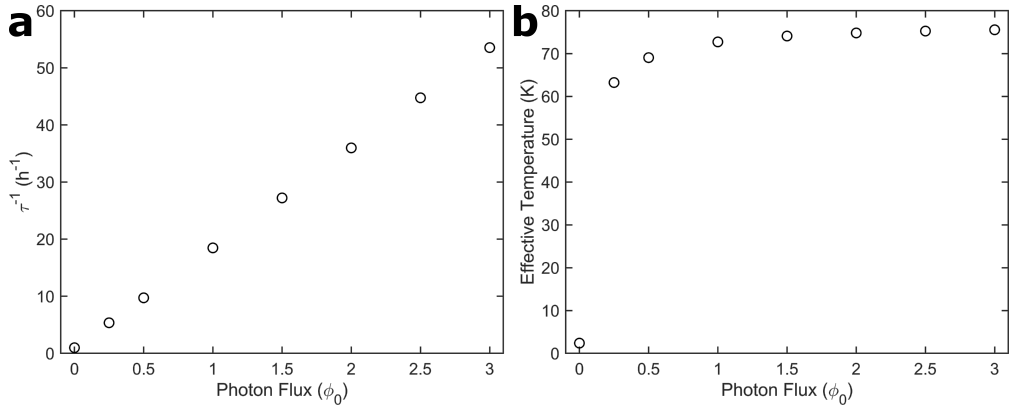

Figure 5.6: **Flux dependence of 4f^{10} Ho$^{\mathrm{T}}$ properties**: **a**, Magnetization reversal rate **b**, Effective temperature (simulation parameters T = 2.5K, B = 6.8T).

5.3.4 Details on spin dynamics calculations

As mentioned in the main text, we calculate the spin dynamics using the Pauli Master rate equation with two competing scattering processes:

$$\frac{dp_i}{dt} = \sum_{j=1}^{17} \left((\Gamma_{ij}^{\mathrm{ph}} + \Gamma_{ij}^{\mathrm{se}}) p_j - ((\Gamma_{ji}^{\mathrm{ph}} + \Gamma_{ji}^{\mathrm{se}}) p_i \right) \tag{5.2}$$

The intrinsic spin-phonon scattering is simulated using [97]:

$$\Gamma_{ij}^{\mathrm{ph}} = \Gamma_0^{\mathrm{ph}} \frac{(E_i - E_j)^3}{\exp((E_i - E_j)/(k_{\mathrm{B}} T)) - 1} |M_{ij}|^2 \tag{5.3}$$

Other intrinsic relaxation mechanisms include a two-phonon Raman process as well as quantum tunneling of magnetization (QTM). While the former leads to an observable effect at low magnetic fields and elevated temperatures, for a sample temperature of 2.5 K it practically

plays no role [88]. Similarly, the effect of QTM is too weak to be observed in our measurements and therefore neglected. In Ho^T, this stems from the weak off-diagonal crystal field terms, whereas in Ho^B transitions between resonant and almost resonant states are already too fast to be measured taking into account only spin-phonon coupling. The X-ray induced scattering is simulated as scattering with a high-energy scatterer given by secondary electrons resulting in an energy-independent spin transition rate:

$$\Gamma_{ij}^{\mathrm{se}} = \Gamma_0^{\mathrm{se}} |M_{ij}|^2 \tag{5.4}$$

Note that relaxation via photons absorption of the Ho atoms is too low by about 2 orders of magnitude and can thus not explain the observed magnetization reversal and demagnetization rates, and equally fails to explain the faster relaxation on thinner MgO thicknesses [3]. For this work, we assume a constant secondary electron energy dispersion and include only spin dynamics within the lowest multiplet made of 17 states. The flux dependent coupling Γ_0^{se} between Ho spin and secondary electrons as well as the spin-phonon coupling Γ_0^{ph} are material dependent prefactors and can be extracted by comparison with our previous experimental results. For $4f^{10}$ Ho^T at 6.8 T we have measured magnetization reversal rates $(\Gamma^{ph,T})^{-1} \gtrsim 3690$ s and $(\Gamma^{ph,se})^{-1} \approx (0.5nm^2 \times \phi)^{-1}$ at a given photons flux ϕ ($\mathrm{nm^{-2}s^{-1}}$) [3]. By comparison with theory, we find for Ho^T that $\Gamma_0^{\mathrm{se}} \approx 3.4\times10^5 \times \phi/\phi_0$ using $\phi_0 = 0.01$ $\mathrm{nm^{-2}s^{-1}}$ and $\Gamma_0^{\mathrm{ph}} \approx 4.4\times10^8$ $\mathrm{s^{-1}}$. The flux dependent magnetization reversal rates at 6.8 T are shown in fig. 5.6a. The effective spin temperature used for simulation of the X-ray absorption is calculated using an effective Boltzmann ratio between the lowest two magnetic states $p_2/p_1 = \exp((E_1 - E_2)/(k_{\mathrm{B}} T_{\mathrm{eff}}))$. Its flux dependence is shown in fig. 5.6b.

Assuming the spin-scatter couplings for Ho^B to be on the same order, we find intrinsic lifetimes of 1.1 ns and a negligible effect of the secondary electrons on the reversal rate at typical fluxes close to ϕ_0. The quantum mechanical transition matrix elements $|M_{ij}|^2$ are calculated using the eigenstates obtained from the multiplet calculations and using the total angular momentum operator:

$$|M_{ij}|^2 = |\langle i|J|j\rangle|^2 = |\langle i|J_z|j\rangle|^2 + \frac{1}{2}|\langle i|J_-|j\rangle|^2 + \frac{1}{2}|\langle i|J_+|j\rangle|^2 \tag{5.5}$$

The solution in the steady state limit of eq. S1 obtained by rewriting the coupled Pauli Master rate equation system as a matrix multiplication problem $dp/dt = G \times p$ and then finding the kernel and L1 norm:

$$p_{\mathrm{s.s.}} = \ker(G) / \parallel \ker(G) \parallel \tag{5.6}$$

The matrix G contains the experimental parameters such as temperature, photons flux and magnetic field. The dynamical solution to eq. S1 is calculated via direct Runge-Kutta integration. We calculate the magnetization as the product of the magnetic field dependent population found at each point in time multiplied by the total angular momenta of the respective states. The resulting curves are rescaled by the XMCD amplitude found using Quanty

[51] at the initial condition. For $4f^{10}$ Ho^T we find that our calculations overestimate the transition rates at magnetic fields below 2 T. We circumvent this limitation by keeping the transition matrix elements equal to the ones found at 6.8 T, although this merits improvement in the future. Possibly, this stems from overestimated cross-barrier transition matrix elements at low field, although it could also stem from our Debye phonon model overestimating the influence of phonon assisted tunneling below ≈ 2 meV via excited angular momentum states (see subsection 5.3.6). At higher temperature, it has been shown that two-phonon Raman processes mediated by a local phonon mode dominate magnetization reversal at low fields [88]. The vanishing DOS of the local phonon mode below 2 meV could create an effective phonon bottleneck, and thereby preventing efficient cross-barrier transitions.

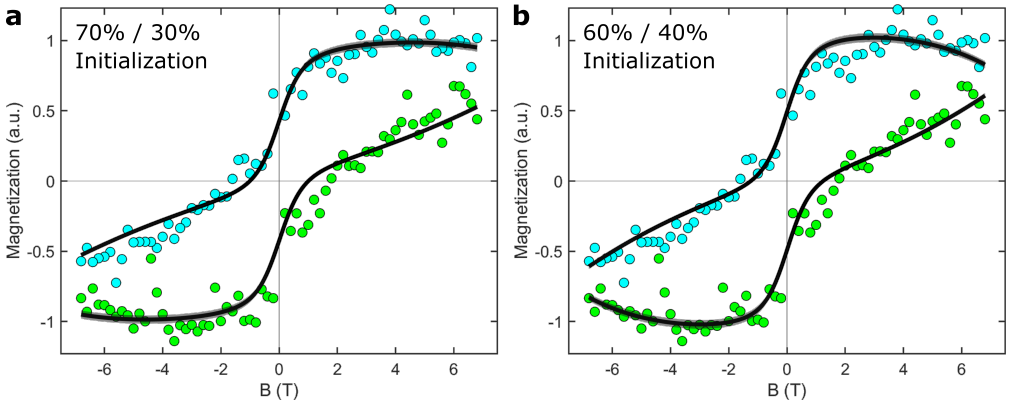

Figure 5.7: **Effect of non-steady-state initialization**: **a**, Assuming an initial 70/30 distribution within the ground state doublet of Ho^T. **b**, An initial 60/40 distribution leads to an excellent agreement with the backwards magnetization curve ($T = 2.5$ K, $dB/dT = 33$ mT/s, $\phi = 1.1\times10^{-2}$ $nm^{-2}s^{-1}$, $\Theta_{Ho} = 0.009$ ML).

Regarding the magnetization loops, a point worth investigating in greater detail is the initial condition. In all theoretical curves displayed throughout the main text, we assume the spins to be initialized in the steady state limit. However, the magnetization curves in fig. 5.4 show partially a non-monotonic trend in the backwards sweep (-6.8 T to 6.8 T) which can not be explained within this framework. Figure 5.7 shows the same measurement as in fig. 5.4a but considering a different initial condition. While at an effective temperature of ≈ 74 K in Ho^T (found for a sample temperature of 2.5 K and a flux of 1.1 ϕ_0 at an external field of 6.8 T) leads to an approximate 78/22 distribution of population in the ground state doublet initially, here we consider a 70/30 and 60/40 initial distribution. This leads the magnetization to initially increase despite decreasing field, and improves the agreement between theory and experiment further. Experimentally, this can occur when experimental parameters such as the magnetic field were changed shortly before acquisition of the data such that the sample has not had enough time to reach the steady state limit.

5.3.5 Additional data

All additional experiments were carried out using similar parameters and sample preparation routines as for the experiments displayed in the main text.

Temperature dependent X-ray absorption

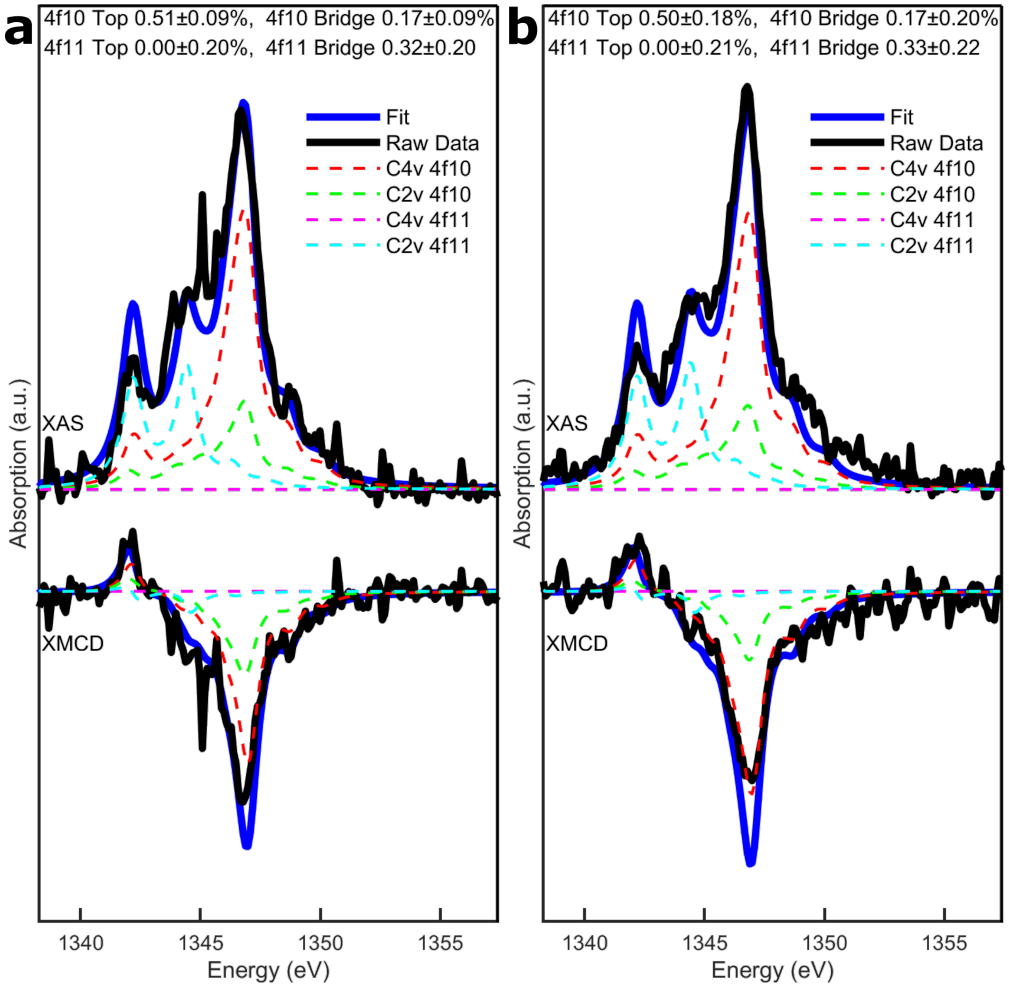

Figure 5.8: **Temperature dependent XAS**: **a**, Sample temperature of 10 K, and b, 30 K (B = 6.8 T, $\phi = 2.15\times10^{-2}$ nm^{-2}s^{-1}, Θ_{Ho} = 0.028 ML).

Varying the temperature offers another way to controllably test the theory presented here. Figure 5.8 shows XAS measurements of the same sample at 10 K and 30 K. When changing the temperature and assuming negligible sample degradation, the sample composition must remain constant at all temperatures. By looking at X-ray measurements at higher temperatures, we find this to be the case only when using the effective temperatures calculated using the Pauli Master equation. While $4f^{10}$ Ho$^{\mathrm{B}}$ and both $4f^{11}$ species are close to or at thermal equilibrium, $4f^{10}$ Ho$^{\mathrm{T}}$ must remain far from equilibrium according to the theory presented

here. Interestingly, the calculated effective temperature in $4f^{10}$ Ho$^{\mathrm{T}}$ is lower at higher sample temperatures at typically used photons fluxes due to the increased spin-phonon scattering driving the sample closer to thermal equilibrium.

Clustering and degradation

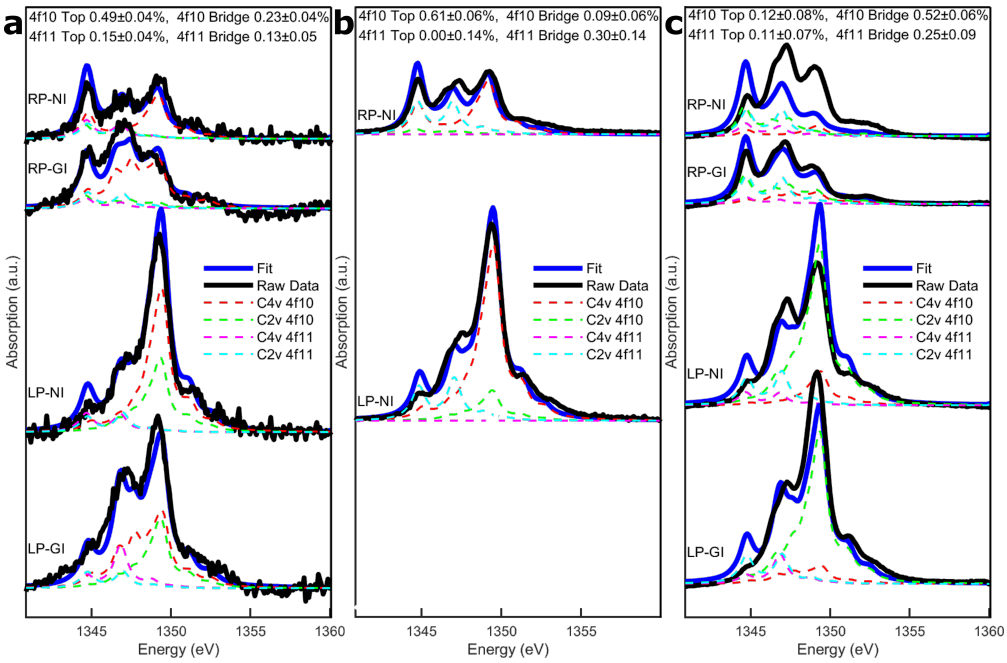

Figure 5.9: **Clustering and depreciation**: **a**, 1$^{\mathrm{st}}$ deposition (Θ_{Ho} = 0.005 ML). b, 2$^{\mathrm{nd}}$ deposition (Θ_{Ho} = 0.067 ML). c, After annealing at 200 K (B = 6.8 T, $\phi = 2.15\times10^{-2}$ nm^{-2}s^{-1}).

In order to test the effect of clustering and general degradation of the sample, we grew a sample at standard conditions yielding a Ho$^{\mathrm{T}}$ majority sample and increased the Ho coverage in subsequent depositions, as well as annealed the system to 200 K. At such a temperatures we expect the single atoms to diffuse and start clustering. Figure 5.9 shows the result of the experiment. As expected, the line shape drastically changes and can no more be explained within the framework of single Ho atoms as presented in this work. Specifically, we find the leftmost shoulder strongly reduced in all spectra indicating a reduction of the $4f^{11}$ species due to increased coordination, as well as a strong reduction of XMCD signal in normal incidence.

Temperature dependent magnetization loops

Fig 5.10 shows temperature dependent magnetization loops at 10, 15 and 20 K. The theoretical calculations are again in excellent agreement with the experimental data. However, between each of these measurements several hours passed, and we find a significant reduction of Ho$^{\mathrm{T}}$ as time passed. For the theoretical simulations we assume a relative reduction of approx. 15% of Ho$^{\mathrm{T}}$ between each subsequent measurement, as well as an overall reduction of amplitude

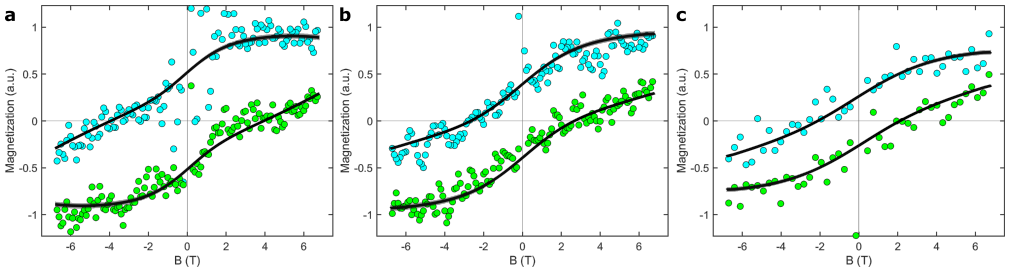

Figure 5.10: **Temperature dependent magnetization loops**: **a**, 10 K, **b**, 15 K, and **c**, 20 K (B = 6.8 T, $\phi = 0.55\times10^{-2}$ nm^{-2}s^{-1}, $\Theta_{\mathrm{Ho}} = 0.01$ ML).

of the XMCD signal of approx. 25%. The latter is an expected result of clustering and sample degradation as demonstrated in fig. 5.9.

5.3.6 Relaxation path analysis and comparison with STM experiments

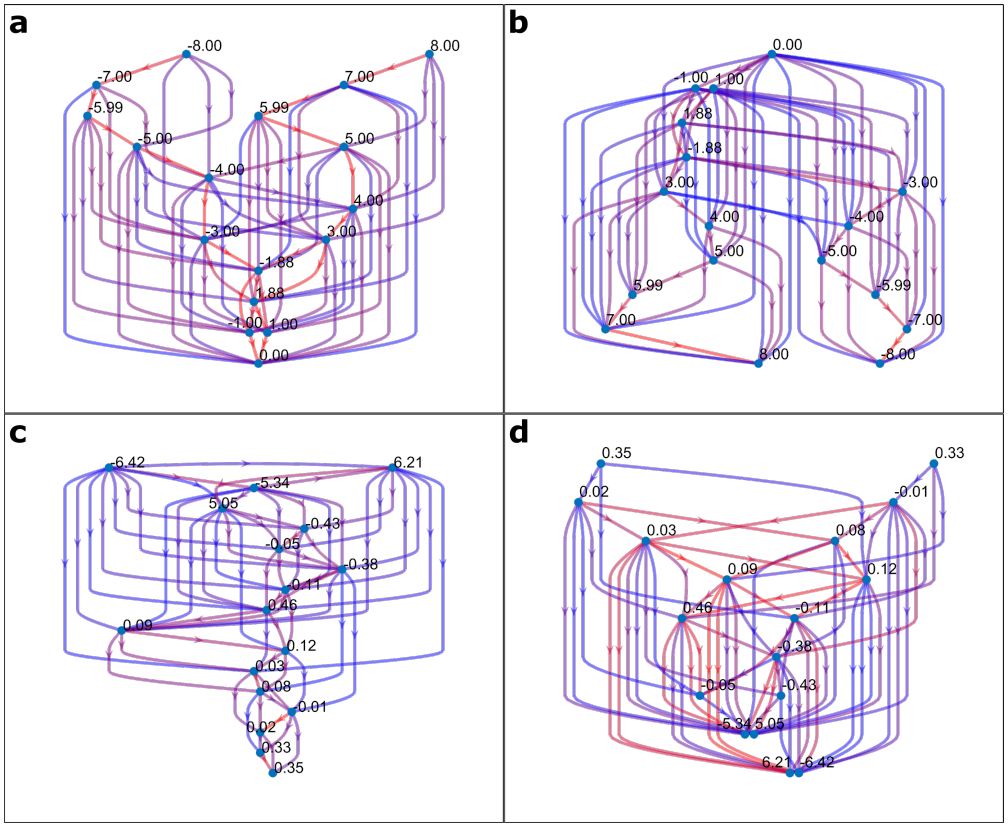

Figure 5.11: **Graph analysis of excitations and deexcitations in Ho spins**: **a**, Excitation and **b**, deexcitation processes in Ho$^{\mathrm{T}}$ and **c**, **d**, Ho$^{\mathrm{B}}$. Transitions drawn correspond to the 50th percentile of the respective transition rates and are logarithmically color coded with red transitions corresponding to most dominant ones (Simulation parameters T = 2.5 K, B = 6.8 T, $\phi = 1.1\times10^{-2}$ nm^{-2}s^{-1}).

Figure 5.11 visualizes the important transition paths defined as $\Gamma^{\mathrm{tot}}_{ij} = \Gamma^{\mathrm{ph}}_{ij} + \Gamma^{\mathrm{se}}_{ij}$. For $\mathrm{Ho^T}$, excitation and deexcitation happens predominantly by climbing the spin ladder up or down, with the off-diagonal crystal field terms introducing efficient sub-barrier shortcuts at energies $\gtrsim 70$ meV. For $\mathrm{Ho^B}$, due to the strongly superposed quantum states in the low-symmetry environment, a finite transition probability between any state exists.

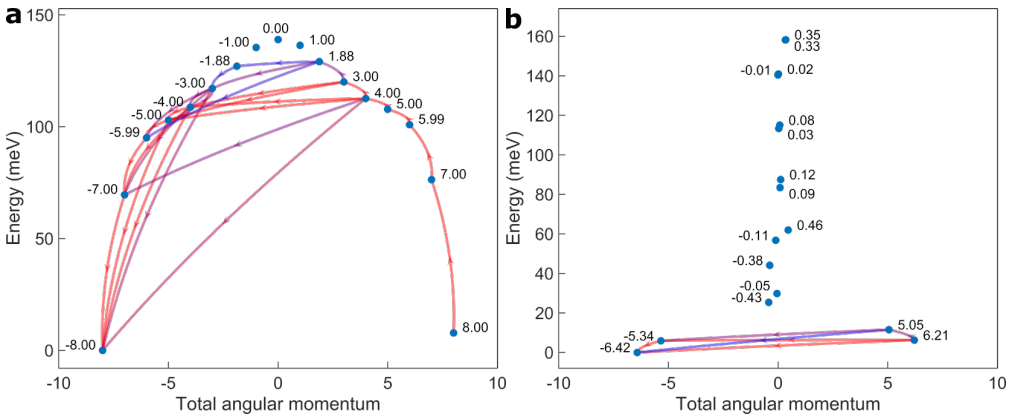

Figure 5.12: **Minimum transition time reversal paths**: **a**, 30 shortest paths from $< m_j >$ = +8 to $< m_j >$ = -8 as define in eq. 6 for $\mathrm{Ho^T}$ and **b**, 4 shortest paths for $\mathrm{Ho^B}$. Transitions are logarithmically color coded by the respective distance with red transitions corresponding to the shortest paths. The numbers of paths are chosen to demonstrate the main physical principles behind the magnetization reversals and are limited for visual clarity (Simulation parameters $T = 2.5$ K, $B = 6.8$ T, $\phi = 1.1\times10^{-2}$ nm^{-2}s^{-1}).

In order to visualize some of the most important relaxation paths, we calculate the set of subsequent transitions transitions $T^{\tau*}_{nm} = \{\tau_{in}, \tau_{ji}, ..., \tau_{mk}\}$ that minimizes the transition time between two states n,m:

$$T^{\tau*}_{nm} = \underset{T_{nm}}{\operatorname{argmin}} \sum_{(i,j)\epsilon T_{nm}} \tau_{ij} \tag{5.7}$$

Here we use $\tau_{ij} = (\Gamma_{ij})^{-1}$. This combinatorial optimization problem is solved using Yen's algorithm [111] leading to the results displayed in fig. 5.12.

Another way to measure relaxation paths is given by SP-STM. The tunneling electrons act as a high-energy scatterer whose energy can be controlled through the applied bias. This results in a bias dependent telegraph signal in $\mathrm{Ho^T}$ [38]. We model the spin dynamics using a Pauli master equation similar to eq. S1 with spin-phonon scattering as defined in eq. S2 and spin-electron-scattering defined as [34]:

$$\Gamma^{\mathrm{te}}_{ijts}(V) = \lambda \frac{G}{e^2} \frac{E_i - E_j - eV}{\exp((E_i - E_j - eV)/(k_{\mathrm{B}}T)) - 1} |M_{ij}|^2 \tag{5.8}$$

$$\Gamma^{\mathrm{te}}_{ijst}(V) = \lambda \frac{G}{e^2} \frac{E_i - E_j + eV}{\exp((E_i - E_j + eV)/(k_{\mathrm{B}}T)) - 1} |M_{ij}|^2 \tag{5.9}$$

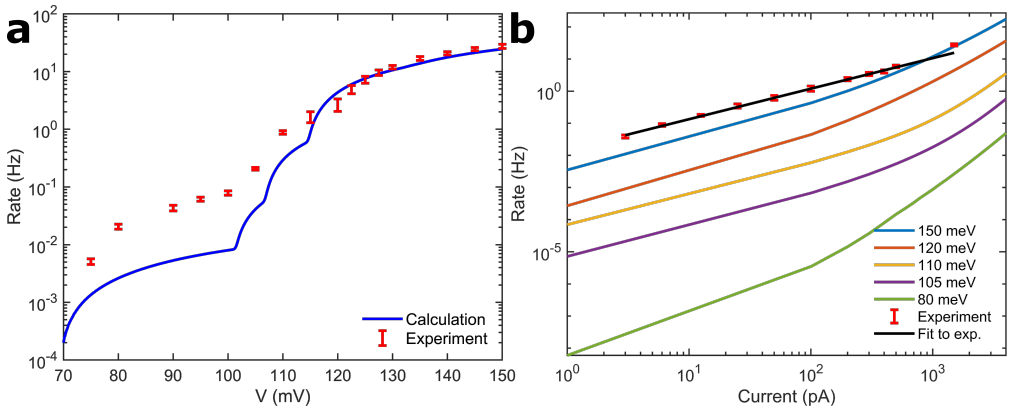

Figure 5.13: **Reversal rates in STM**: Comparison between calculated and measured 2-state switching rates in Ho. **a**, Voltage dependence (I = 1.5 nA). **b**, Current dependence. The fit to experiment is given by $\Gamma(I) = a \times (I/I_0)^N$ using $a = 1.2 \times 10^{-2}$, I_0 = 1 pA, and N = 0.95. Fit parameters and experimental data are given in ref. [38]. The original fit to experiment is based on the data ranging from 3 to 500 pA and has an exponent N close to unity, which indicates a single electron process in the low current range, in agreement with the calculated spectra. An additional data point at 1.5 nA can be recovered by using the data displayed in fig. 5.13a. The switching rate at 1.5 nA is statistically significantly increased compared to the original fit to experiment, indicating a superlinear dependence at large currents. This results from multi electron processes as described in this work and is equally found in the calculated spectra (Simulation parameter: λ = 0.5; Experimental parameters: T = 1.2 K, $B_z \approx 50$ mT, $B_x \approx 492$ mT).

The two equations describe scattering rates for electrons tunneling from sample to tip and vice versa, respectively. The fit parameter λ denotes the fraction of tunneling electrons scattering with the Ho spin. While in principle spin dynamics between 17 different states are present in the system, experimentally only a 2-state switching is observed. Rapid excitations and deexcitations at picosecond to nanosecond timescales between quantum states beyond the ground state doublet are too fast to be resolved using a typical preamplifier with bandwidths $\approx$ 1 kHz and therefore must result in an effective two-state signal. In our calculations, we interpret the 2-state switching as the Ho spin being on one side of the barrier or the other, where on either side it resides predominantly in the lowest state. We calculate the switching rate between either side of the barrier as the steady-state occupation of each of the 17 states multiplied by the associated cross-barrier transition rates per state at a given voltage and current. We again use the transition matrix elements determined at 6.8 T since our model of Ho^T systematically overestimated transition rates below < 2 T as described earlier. Figure 5.13 shows a comparison between the calculated and experimental result. They are qualitatively in good agreement. The calculated energies of the dominant transition pathways are slightly underestimated by less than 5% compared the experimentally observed ones. Possibly, this results from a slight overestimation in the Ho-O bond length in DFT or alternatively from a slight underestimation of the effective electron charge of the underneath oxygen. The mismatch in some of the relative transition intensities most likely stems from incorrect

estimations of the off-diagonal crystal field terms and might be a signature of the limitation of a point charge model, likely in combination with the simplistic model of the phonon DOS. Parts of the disagreement may also result from the invasiveness of the STM measurements, which perturb the system through local electric [112], magnetic [113] and mechanical [114] gating, which is beyond the scope of this work.

The calculated STM spectra in fig. 5.13a shows the first significant increase in the reversal rate at ≈ 70 meV, where transitions from $< m_j > = \pm 8$ to $< m_j > = \pm 7$ become possible. Once this threshold is reached, climbing up the spin ladder in a multi electron process and finally crossing the barrier becomes possible, as shown in fig. 5.12. Subsequent strong increases can be found between 100 and 120 meV, where direct transitions to states allowing for efficient sub-barrier magnetization reversal become possible. Figure 5.13b shows the calculated current dependence of switching rates for different bias voltages. The current dependence shows a non-linear dependence and transitions to superlinear at higher currents, with the onset happening earlier at lower voltages. This nonlinear behavior is a fingerprint of multi electron processes and inconsistent with single electron processes. The onset of the superlinear trend is particularly pronounced at low voltages just above the first threshold, since additional switching occurring when crossing the first voltage threshold is predominantly a result of multi electron processes, as visualized in fig. 5.12a. In agreement with the calculations, this transition to a superlinear dependence can be observed upon close inspection of the data in ref. [38], as detailed in fig. 5.13b. Similarly, these results yield an explanation for the superlinear behavior recently observed for Dy/MgO [75]. In the latter system, sub-barrier tunneling probabilities are even lower compared to Ho/MgO, and therefore a superlinear current dependence can be observed already at low currents.

5.4 Conclusion and outlook

The question of what exactly is measured on a microscopic level when using macroscopic, ensemble-averaging experimental techniques is a common issue. Regarding Ho/MgO, based on initial STM experiments, the assumption was made that the ensemble must consist mostly of top-site Ho. Based on this ultimately wrongful assumption in the context of the herein presented X-ray studies, sum rule analysis lead to wrong conclusions regarding the magnetic properties of $4f^{10}$ top-site Ho. The sum rule analysis is sensitive to the precise configuration of the ensemble and therefore should in future be applied with great care in similar experiments. Relaxation and magnetization reversal measurements, however, are still valid (albeit with a perturbative influence of the secondary electrons), since the observed slow magnetization dynamic necessarily stems from the slowest relaxing species. This fact allowed to discover world's first SAM, as was subsequently confirmed by local STM measurements. The research history of Ho/MgO also shows how one needs to be careful with a Stevens operator based approach to describe the crystal field, since the large amount of free parameters easily leads to overfitting, with different sets of parameters being able to explain the same experimental

observations [56]. Equally, the initial DFT calculations in ref. [3] are in agreement with therein found sum rule analysis, whereby the latter turns out to be incorrect due to the inhomogenous and out-of-equilibrium nature of the measured ensemble. This story further underlines the difficulty of applying DFT in a surface science context, and in return highlights the importance of experimental studies in this context.

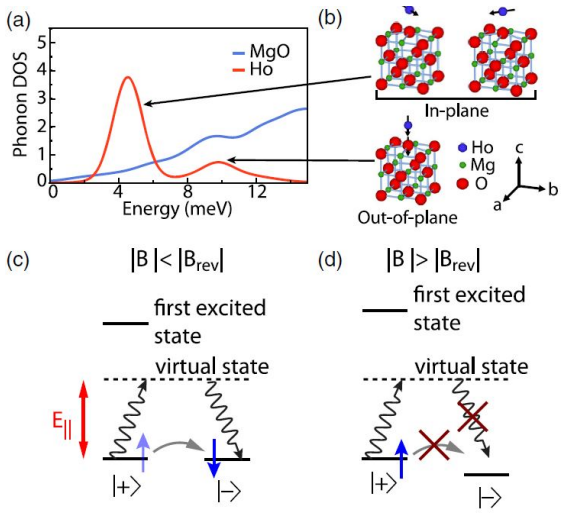

Figure 5.14: **Local phonon DOS and Raman process**: **a**, DFT derived phonon DOS projected onto $4f^{10}$ top-site Ho (red) and the MgO slab (blue). Below 2 meV, the DOS of the local modes vanishes. **b**, Schematic of the local phonon modes. **c**, Raman process between magnetic states close to resonance. **d,** The Raman processes between states far away from resonance may be impossible, if no energetically matching phonons are available. Image and calculations from ref. [88].

The theoretical approach to calculate the static magnetic properties presented in this work relies on relatively few free parameters and therefore represents a hopefully robust approach to describe the magnetic properties of single magnetic adatoms. Regarding Ho and Dy on MgO, this does seem to be the case. Regarding the approach to describe the dynamics, the herein presented model suffices to demonstrate the main points of the paper, namely the fact that we measure a heterogeneous ensemble, and how additional scattering due to an invasive measurement, be it X-ray based or STM based, leads to the observed non-equilibrium properties. Building on this proof of concept, future work may use a more complex model. Equation 5.1 does not include pure QTM, which certainly plays a role at low temperature and low magnetic fields, although in most of the experiments displayed here, it is overshadowed by dominant external scattering mechanisms and spin-phonon scattering. Equally, the equation does not include Raman processes, which have been shown to play a role at elevated temperatures above $\approx$ 20 K where a local in-plane phonon mode gets populated [88], a regime not investigated in detail here. The Debye model for the phonon DOS could in future work be replaced by a DFT derived phonon DOS. This likely yields in a reduced magnetization reversal rate at low Zeeman splittings due to a phonon bottleneck below 2 meV

where the DOS of the local modes vanishes [88], see fig. 5.14. Such a reduction of reversal rates at low fields is strongly counter-intuitive, since the mixing of the magnetic quantum states increases when lowering the external magnetic field, which in return would increase the reversal rates. However, this phenomena was was observed both in Ho/MgO, see ref. [3], as well as in Dy, see previous chapter. Finally, future work may consider a secondary electron dispersion differing from the uniform distribution. Nonetheless, our approach was able to describe to a good degree the heterogeneous composition of the Ho ensemble, as well as its magnetization dynamics and the influence of the secondary electrons, as well as the observed properties in STM based measurements, and was able to explain the different conclusions drawn from local STM and ensemble averaging X-ray measurements. Ideally, this work serves as a template for future studies of heterogeneous magnetic adatom ensembles, and the dynamics therein.

6 Conclusion and outlook

ESR-STM has opened up several new dimensions when it comes to research on magnetic nanostructures on surfaces. Extracting physical parameters such as coherence times and Rabi rates, measuring entanglement and coherent control of these structures, has finally become possible. This work gives a detailed overview of the theoretical concepts behind ESR-STM, and an in-depth discussion on how such experiments can be implemented successfully. We applied this technique to coherently control the metal-organic molecule FePc, and to sense a ligand mediated exchange interaction. Applying ESR-STM to Fe atoms and using them as remote sensors, we demonstrated the outstanding magnetic stability of Dy atoms on MgO even in absence of an external magnetic field. Perspectives on what type of future experiments may be of particular interest regarding these or similar systems can be found at the end of the respective chapters. Later, we analyzed X-ray studies on Ho/MgO. Apart from STM, this experimental technique represents the other main tool that enables to study the magnetic properties of single spins on surfaces. We present a theoretical approach combining DFT, point-charge derived crystal fields, and multiplet calculations to describe the magnetostatic properties of lanthanide adatoms, which works well for both Ho and Dy on MgO. Regarding the magnetization dynamics, we describe in detail the perturbative influence of the X-ray induced secondary electrons, which lead to an increased effective spin temperature. Using the results of these calculations, we find that the Ho adatom ensembles consist of several different species with strongly charge and adsorption site dependent properties, a result also found in current studies on Dy/MgO [96]. The calculated spectra and fitted occurrences of the different adsorption sites and charge configurations lead to an excellent agreement between the theoretical and experimental absorption and dichroism spectra. This reconciles the apparent differences between STM and X-ray derived results for top-site 4f10 Ho and leads to a comprehensive understanding of the first single atom magnet.

Regarding the future, ESR-STM has by now been successfully demonstrated by several research groups around the world, and a further number of groups is currently working on upgrading their systems for ESR-STM. Some of the very recent work revolves around quantum coherent

control [8, 69] and entanglement [42, 115], a direction that will likely be explored further in the future. Of particular interest is hereby the possibility of an STM to engineer tailored quantum matter atom-by-atom [116]. Another avenue worth exploring is presented by nuclear spins. Yang *et al.* have recently demonstrated polarization of the nuclear spin through tunneling electrons, as well as electron-nuclear double resonance [39]. In light of these results, as well as of some of the outstanding results achieved in single magnetic molecules in break junctions [117–119], it is likely only a matter of time until new research on nuclear spins using an STM appears, either directly on nuclear spin dynamics, nuclear spin induced electron spin dynamics, or their combined dynamics. Remote sensing of the magnetic stray field of adatoms or molecules, as was applied in detail to Dy in this work, likely will continue to play a role, with potentially particularly interesting phenomena becoming observable when sensing a nearby system across a quantum phase transition. A completely different route is explored by the research group of K. Franke, who used the technical progress made for ESR-STM, but applied it to investigate radiofrequency phenomena in Yu-Shiba-Rusinov states [120, 121]. X-ray absorption based experiments will continue to play an important role when investigating single magnetic adatoms and molecules due to the exclusive information not found in STM experiments, such as the distinct orbital and spin contributions to the total angular momentum, and the ability to measure large ensembles at once. Future work, however, will hopefully benefit from the experimental and theoretical approaches described in this work to investigate the static and dynamic properties of such quantum magnets.

Bibliography

1. Sessoli, R., Gatteschi, D., Caneschi, A. & Novak, M. A. Magnetic bistability in a metal-ion cluster. *Nature* **365,** 141–143. doi:10.1038/365141a0 (Sept. 1993).
2. Gambardella, P. *et al.* Giant Magnetic Anisotropy of Single Cobalt Atoms and Nanoparticles. *Science* **300,** 1130–1133. doi:10.1126/science.1082857 (May 2003).
3. Donati, F. *et al.* Magnetic remanence in single atoms. *Science* **352,** 318–321. doi:10.1126/science.aad9898 (Apr. 2016).
4. Guo, F.-S. *et al.* Magnetic hysteresis up to 80 kelvin in a dysprosium metallocene single-molecule magnet. *Science* **362,** 1400–1403. doi:10.1126/science.aav0652 (Dec. 2018).
5. Atzori, M. *et al.* Room-Temperature Quantum Coherence and Rabi Oscillations in Vanadyl Phthalocyanine: Toward Multifunctional Molecular Spin Qubits. *Journal of the American Chemical Society* **138,** 2154–2157. doi:10.1021/jacs.5b13408 (Feb. 2016).
6. Goodwin, C. A. P., Ortu, F., Reta, D., Chilton, N. F. & Mills, D. P. Molecular magnetic hysteresis at 60 kelvin in dysprosocenium. *Nature* **548,** 439–442. doi:10.1038/nature23447 (Aug. 2017).
7. Baumann, S. *et al.* Electron paramagnetic resonance of individual atoms on a surface. *Science* **350,** 417–420. doi:10.1126/science.aac8703 (Oct. 2015).
8. Yang, K. *et al.* Coherent spin manipulation of individual atoms on a surface. *Science* **366,** 509–512. doi:10.1126/science.aay6779 (Oct. 2019).
9. Yazdani, A., Jones, B. A., Lutz, C. P., Crommie, M. F. & Eigler, D. M. Probing the Local Effects of Magnetic Impurities on Superconductivity. *Science* **275,** 1767–1770. doi:10.1126/science.275.5307.1767 (Mar. 1997).
10. Madhavan, V., Chen, W., Jamneala, T., Crommie, M. F. & Wingreen, N. S. Tunneling into a Single Magnetic Atom: Spectroscopic Evidence of the Kondo Resonance. *Science* **280,** 567–569. doi:10.1126/science.280.5363.567 (Apr. 1998).
11. Li, J., Schneider, W.-D., Berndt, R. & Delley, B. Kondo Scattering Observed at a Single Magnetic Impurity. *Physical Review Letters* **80,** 2893–2896. doi:10.1103/PhysRevLett.80.2893 (Mar. 1998).
12. Heinrich, A. J., Gupta, J. A., Lutz, C. P. & Eigler, D. M. Single-Atom Spin-Flip Spectroscopy. *Science* **306,** 466–469. doi:10.1126/science.1101077 (Oct. 2004).

13. Meier, F., Zhou, L., Wiebe, J. & Wiesendanger, R. Revealing Magnetic Interactions from Single-Atom Magnetization Curves. *Science* **320,** 82–86. doi:10.1126/science.1154415 (Apr. 2008).

14. Loth, S., Etzkorn, M., Lutz, C. P., Eigler, D. M. & Heinrich, A. J. Measurement of Fast Electron Spin Relaxation Times with Atomic Resolution. *Science* **329,** 1628–1630. doi:10.1126/science.1191688 (Sept. 2010).

15. Choi, T. *et al.* Atomic-scale sensing of the magnetic dipolar field from single atoms. *Nature Nanotechnology* **12,** 420–424. doi:10.1038/nnano.2017.18 (May 2017).

16. Willke, P. *et al.* Hyperfine interaction of individual atoms on a surface. *Science* **362,** 336–339. doi:10.1126/science.aat7047 (Oct. 2018).

17. Binnig, G., Rohrer, H., Gerber, C. & Weibel, E. Surface Studies by Scanning Tunneling Microscopy. *Physical Review Letters* **49,** 57–61. doi:10.1103/PhysRevLett.49.57 (July 1982).

18. Young, R., Ward, J. & Scire, F. The Topografiner: An Instrument for Measuring Surface Microtopography. *Review of Scientific Instruments* **43,** 999–1011. doi:10.1063/1.1685846 (July 1972).

19. Young, R., Ward, J. & Scire, F. Observation of Metal-Vacuum-Metal Tunneling, Field Emission, and the Transition Region. *Physical Review Letters* **27,** 922–924. doi:10.1103/PhysRevLett.27.922 (Oct. 1971).

20. Amato, I. Candid Cameras for the Nanoworld. *Science* **276,** 1982–1985. doi:10.1126/science.276.5321.1982 (June 1997).

21. Stroscio, J. A. & Eigler, D. M. Atomic and Molecular Manipulation with the Scanning Tunneling Microscope. *Science* **254,** 1319–1326. doi:10.1126/science.254.5036.1319 (Nov. 1991).

22. Wiesendanger, R., Güntherodt, H.-J., Güntherodt, G., Gambino, R. J. & Ruf, R. Observation of vacuum tunneling of spin-polarized electrons with the scanning tunneling microscope. *Physical Review Letters* **65,** 247–250. doi:10.1103/PhysRevLett.65.247 (July 1990).

23. Chen, C. J. *Introduction to Scanning Tunneling Microscopy: Second Edition* (Oxford University Press, 1993).

24. Voigtlaender, B. *Scanning Probe Microscopy: Atomic Force Microscopy and Scanning Tunneling Microscopy* (Springer-Verlag, 2015).

25. Wiesendanger, R. Spin mapping at the nanoscale and atomic scale. *Reviews of Modern Physics* **81,** 1495–1550. doi:10.1103/RevModPhys.81.1495 (Nov. 2009).

26. Néel, N., Kröger, J. & Berndt, R. Quantized Conductance of a Single Magnetic Atom. *Physical Review Letters* **102,** 086805. doi:10.1103/PhysRevLett.102.086805 (Feb. 2009).

27. Forrester, P. R., Bilgeri, T., Patthey, F., Brune, H. & Natterer, F. D. Antiferromagnetic MnNi tips for spin-polarized scanning probe microscopy. *Review of Scientific Instruments* **89,** 123706. doi:10.1063/1.5042530 (Dec. 2018).

28. Paul, W. *et al.* Control of the millisecond spin lifetime of an electrically probed atom. *Nature Physics* **13,** 403–407. doi:10.1038/nphys3965 (Apr. 2017).

29. Breuer, H.-P. & Petruccione, F. *The Theory of Open Quantum Systems* (Oxford University Press, 2002).

30. Gatteschi, D., Sessoli, R. & Villain, J. *Molecular Nanomagnets* (Oxford University Press, 2006).

31. Ternes, M. Spin excitations and correlations in scanning tunneling spectroscopy. *New Journal of Physics* **17,** 063016. doi:10.1088/1367-2630/17/6/063016 (June 2015).

32. Ternes, M. Probing magnetic excitations and correlations in single and coupled spin systems with scanning tunneling spectroscopy. *Progress in Surface Science* **92,** 83–115. doi:10.1016/j.progsurf.2017.01.001 (Feb. 2017).

33. Tedrow, P. M. & Meservey, R. Spin Polarization of Electrons Tunneling from Films of Fe, Co, Ni, and Gd. *Physical Review B* **7,** 318–326. doi:10.1103/PhysRevB.7.318 (Jan. 1973).

34. Loth, S. *et al.* Controlling the state of quantum spins with electric currents. *Nature Physics* **6,** 340–344. doi:10.1038/nphys1616 (May 2010).

35. Lado, J. L., Ferrón, A. & Fernández-Rossier, J. Exchange mechanism for electron paramagnetic resonance of individual adatoms. *Physical Review B* **96,** 205420. doi:10.1103/PhysRevB.96.205420 (Nov. 2017).

36. Seifert, T. S. *et al.* Longitudinal and transverse electron paramagnetic resonance in a scanning tunneling microscope. *Science Advances* **6,** eabc5511. doi:10.1126/sciadv.abc5511 (Oct. 2020).

37. Yang, K. *et al.* Engineering the Eigenstates of Coupled Spin-$1/2$ Atoms on a Surface. *Physical Review Letters* **119,** 227206. doi:10.1103/PhysRevLett.119.227206 (Nov. 2017).

38. Natterer, F. D. *et al.* Reading and writing single-atom magnets. *Nature* **543,** 226–228. doi:10.1038/nature21371 (Mar. 2017).

39. Yang, K. *et al.* Electrically controlled nuclear polarization of individual atoms. *Nature Nanotechnology* **13,** 1120. doi:10.1038/s41565-018-0296-7 (Dec. 2018).

40. Willke, P. *et al.* Probing quantum coherence in single-atom electron spin resonance. *Science Advances* **4,** eaaq1543. doi:10.1126/sciadv.aaq1543 (Feb. 2018).

41. Bae, Y. *et al.* Enhanced quantum coherence in exchange coupled spins via singlet-triplet transitions. *Science Advances* **4,** eaau4159. doi:10.1126/sciadv.aau4159 (Nov. 2018).

42. Veldman, L. M. *et al.* Free coherent evolution of a coupled atomic spin system initialized by electron scattering. *arXiv:2101.10765 [cond-mat]* (Jan. 2021).

43. Paul, W., Baumann, S., Lutz, C. P. & Heinrich, A. J. Generation of constant-amplitude radio-frequency sweeps at a tunnel junction for spin resonance STM. *Review of Scientific Instruments* **87,** 074703. doi:10.1063/1.4955446 (July 2016).

44. Baumann, S. *et al.* Origin of Perpendicular Magnetic Anisotropy and Large Orbital Moment in Fe Atoms on MgO. *Physical Review Letters* **115,** 237202. doi:10.1103/PhysRevLett.115.237202 (Dec. 2015).

45. Abragam, A. & Bleaney, B. *Electron Paramagnetic Resonance of Transition Ions* (Oxford University Press, 2012).

46. Baranov, P. G., Bardeleben, H. J. v., Jelezko, F. & Wrachtrup, J. *Magnetic Resonance of Semiconductors and Their Nanostructures: Basic and Advanced Applications* (Springer-Verlag, 2017).

47. Yang, K. *et al.* Tunable giant magnetoresistance in a single-molecule junction. *Nature Communications* **10,** 1–7. doi:10.1038/s41467-019-11587-x (Aug. 2019).

48. Brune, H. & Gambardella, P. Magnetism of individual atoms adsorbed on surfaces. *Surface Science. Special Issue of Surface Science dedicated to Prof. Dr. Dr. h.c. mult. Gerhard Ertl, Nobel-Laureate in Chemistry 2007* **603,** 1812–1830. doi:10.1016/j.susc.2008.11.055 (June 2009).

49. Baltic, R. *Magnetic Stability of Single Lanthanide Atoms on Graphene* 2018. doi:10.5075/epfl-thesis-8342.

50. Singha, A. *et al.* Orbital-resolved single atom magnetism measured with X-ray absorption spectroscopy. *arXiv:2012.10972 [cond-mat]* (Dec. 2020).

51. Haverkort, M. W. Quantyfor core level spectroscopy - excitons, resonances and band excitations in time and frequency domain. *Journal of Physics: Conference Series* **712,** 012001. doi:10.1088/1742-6596/712/1/012001 (May 2016).

52. Schintke, S. *et al.* Insulator at the Ultrathin Limit: MgO on Ag(001). *Physical Review Letters* **87,** 276801. doi:10.1103/PhysRevLett.87.276801 (Dec. 2001).

53. Baumann, S., Rau, I. G., Loth, S., Lutz, C. P. & Heinrich, A. J. Measuring the Three-Dimensional Structure of Ultrathin Insulating Films at the Atomic Scale. *ACS Nano* **8,** 1739–1744. doi:10.1021/nn4061034 (Feb. 2014).

54. Tsymbal, E. Y. & Zutic, I. *Spintronics Handbook: Spin Transport and Magnetism, Second Edition* (CRC Press, 2019).

55. Fernandes, E. *Adsorption Sites of Metal Atoms on MgO Thin Films and Rotational Quantum State Spectroscopy of Physisorbed H2* 2017. doi:10.5075/epfl-thesis-8144.

56. Natterer, F. D., Donati, F., Patthey, F. & Brune, H. Thermal and Magnetic-Field Stability of Holmium Single-Atom Magnets. *Physical Review Letters* **121,** 027201. doi:10.1103/PhysRevLett.121.027201 (July 2018).

57. Gschneidner, K., Buenzli, J.-C. & Pecharsky, V. *Book Series: Handbook on the Physics and Chemistry of Rare Earths* (Elsevier, 2005).

58. Guo, F.-S., Bar, A. K. & Layfield, R. A. Main Group Chemistry at the Interface with Molecular Magnetism. *Chemical Reviews* **119,** 8479–8505. doi:10.1021/acs.chemrev.9b00103 (July 2019).

59. Rechkemmer, Y. *et al.* A four-coordinate cobalt(II) single-ion magnet with coercivity and a very high energy barrier. *Nature Communications* **7,** 10467. doi:10.1038/ncomms10467 (Feb. 2016).

60. Lawrence, J. M., Riseborough, P. S. & Parks, R. D. Valence fluctuation phenomena. *Reports on Progress in Physics* **44,** 1–84. doi:10.1088/0034-4885/44/1/001 (Jan. 1981).

61. Rinehart, J. D. & Long, J. R. Exploiting single-ion anisotropy in the design of f-element single-molecule magnets. *Chemical Science* **2,** 2078–2085. doi:10.1039/C1SC00513H (Oct. 2011).

62. Natterer, F. D. *et al.* Upgrade of a low-temperature scanning tunneling microscope for electron-spin resonance. *Review of Scientific Instruments* **90,** 013706. doi:10.1063/1.5065384 (Jan. 2019).

63. Claude, L. *Construction d'un microscope à effet tunnel à basse température et études d'impuretés magnétiques en surfaces* 2005. doi:10.5075/epfl-thesis-3276.

64. Dubout, Q. *Magnetism of Single Adatoms and Small Adsorbed Clusters Investigated by Means of Low-Temperature STM* 2013. doi:10.5075/epfl-thesis-5727.

65. Seifert, T. S. *et al.* Single-atom electron paramagnetic resonance in a scanning tunneling microscope driven by a radio-frequency antenna at 4 K. *Physical Review Research* **2,** 013032. doi:10.1103/PhysRevResearch.2.013032 (Jan. 2020).

66. Van Weerdenburg, W. M. J. *et al.* A scanning tunneling microscope capable of electron spin resonance and pump–probe spectroscopy at mK temperature and in vector magnetic field. *Review of Scientific Instruments* **92,** 033906. doi:10.1063/5.0040011 (Mar. 2021).

67. Zhang, X. *et al.* Probing Magnetism in Artificial Metal–Organic Complexes Using Electronic Spin Relaxometry. *The Journal of Physical Chemistry Letters* **11,** 5618–5624. doi:10.1021/acs.jpclett.0c01281 (July 2020).

68. Zhang, X. *et al.* Electron Spin Resonance of Single Molecules and Magnetic Interaction through Ligands. *accepted in Nature Chemistry*. doi:10.21203/rs.3.rs-134144/v1 (Feb. 2021).

69. Willke, P. *et al.* Coherent spin control of single magnetic molecules on surfaces. *submitted to ACS Nano.*

70. Stepanow, S. *et al.* Mixed-valence behavior and strong correlation effects of metal phthalocyanines adsorbed on metals. *Physical Review B* **83,** 220401. doi:10.1103/PhysRevB.83.220401 (June 2011).

71. Zhang, H. G. *et al.* Assembly of iron phthalocyanine and pentacene molecules on a graphene monolayer grown on Ru(0001). *Physical Review B* **84,** 245436. doi:10.1103/PhysRevB.84.245436 (Dec. 2011).

72. Tsukahara, N. *et al.* Adsorption-Induced Switching of Magnetic Anisotropy in a Single Iron(II) Phthalocyanine Molecule on an Oxidized Cu(110) Surface. *Physical Review Letters* **102,** 167203. doi:10.1103/PhysRevLett.102.167203 (Apr. 2009).

73. Hiraoka, R. *et al.* Single-molecule quantum dot as a Kondo simulator. *Nature Communications* **8,** 16012. doi:10.1038/ncomms16012 (June 2017).

74. Lee, M., Yoon, J. & Lee, D. *Atomic Scale Magnetic Sensing and Imaging Based on Diamond NV Centers* doi:10.5772/intechopen.84204 (IntechOpen, Feb. 2019).

75. Singha, A. *et al.* Engineering atomic-scale magnetic fields by dysprosium single atom magnets. *Nature Communications* **12,** 4179. doi:10.1038/s41467-021-24465-2 (July 2021).

76. Pivetta, M. *et al.* Measuring the Intra-Atomic Exchange Energy in Rare-Earth Adatoms. *Physical Review X* **10,** 031054. doi:10.1103/PhysRevX.10.031054 (Sept. 2020).

77. Forrester, P. R. *et al.* Quantum state manipulation of single atom magnets using the hyperfine interaction. *Physical Review B* **100,** 180405. doi:10.1103/PhysRevB.100.180405 (Nov. 2019).

78. Willke, P. *et al.* Tuning Single-Atom Electron Spin Resonance in a Vector Magnetic Field. *Nano Letters* **19,** 8201–8206. doi:10.1021/acs.nanolett.9b03559 (Nov. 2019).

79. Yang, K. *et al.* Tuning the Exchange Bias on a Single Atom from 1 mT to 10 T. *Physical Review Letters* **122,** 227203. doi:10.1103/PhysRevLett.122.227203 (June 2019).

80. Coronado, E. Molecular magnetism: from chemical design to spin control in molecules, materials and devices. *Nature Reviews Materials* **5,** 87–104. doi:10.1038/s41578-019-0146-8 (Feb. 2020).

81. Baltic, R. *et al.* Superlattice of Single Atom Magnets on Graphene. *Nano Letters* **16,** 7610–7615. doi:10.1021/acs.nanolett.6b03543 (Dec. 2016).

82. Gaita-Ariño, A., Luis, F., Hill, S. & Coronado, E. Molecular spins for quantum computation. *Nature Chemistry* **11,** 301–309. doi:10.1038/s41557-019-0232-y (Apr. 2019).

83. Wasielewski, M. R. *et al.* Exploiting chemistry and molecular systems for quantum information science. *Nature Reviews Chemistry* **4,** 490–504. doi:10.1038/s41570-020-0200-5 (Sept. 2020).

84. Dreiser, J. Molecular lanthanide single-ion magnets: from bulk to submonolayers. *Journal of Physics: Condensed Matter* **27,** 183203. doi:10.1088/0953-8984/27/18/183203 (Apr. 2015).

85. Liddle, S. T. & Slageren, J. v. Improving f-element single molecule magnets. *Chemical Society Reviews* **44,** 6655–6669. doi:10.1039/C5CS00222B (Sept. 2015).

86. Ungur, L. & Chibotaru, L. F. Strategies toward High-Temperature Lanthanide-Based Single-Molecule Magnets. *Inorganic Chemistry* **55,** 10043–10056. doi:10.1021/acs.inorgchem.6b01353 (Oct. 2016).

87. Shiddiq, M. *et al.* Enhancing coherence in molecular spin qubits via atomic clock transitions. *Nature* **531,** 348–351. doi:10.1038/nature16984 (Mar. 2016).

88. Donati, F. *et al.* Unconventional Spin Relaxation Involving Localized Vibrational Modes in Ho Single-Atom Magnets. *Physical Review Letters* **124,** 077204. doi:10.1103/PhysRevLett.124.077204 (Feb. 2020).

89. Fernandes, E. *et al.* Adsorption sites of individual metal atoms on ultrathin MgO(100) films. *Physical Review B* **96,** 045419. doi:10.1103/PhysRevB.96.045419 (July 2017).

90. Dreiser, J. *et al.* X-ray induced demagnetization of single-molecule magnets. *Applied Physics Letters* **105,** 032411. doi:10.1063/1.4891485 (July 2014).

91. Westerström, R. *et al.* An Endohedral Single-Molecule Magnet with Long Relaxation Times: DySc2N@C80. *Journal of the American Chemical Society* **134,** 9840–9843. doi:10.1021/ja301044p (June 2012).

92. Donnio, B. *et al.* Magneto-optical interactions in single-molecule magnets: Low-temperature photon-induced demagnetization. *Solid State Sciences* **12,** 1307–1313. doi:10.1016/j.solidstatesciences.2010.06.003 (Aug. 2010).

93. Piamonteze, C. *et al.* X-Treme beamline at SLS: X-ray magnetic circular and linear dichroism at high field and low temperature. *Journal of Synchrotron Radiation* **19,** 661–674. doi:10.1107/S0909049512027847 (Sept. 2012).

94. Barla, A. *et al.* Design and performance of BOREAS, the beamline for resonant X-ray absorption and scattering experiments at the ALBA synchrotron light source. *Journal of Synchrotron Radiation* **23,** 1507–1517. doi:10.1107/S1600577516013461 (Nov. 2016).

95. Singha, A. *et al.* $4f$ occupancy and magnetism of rare-earth atoms adsorbed on metal substrates. *Physical Review B* **96,** 224418. doi:10.1103/PhysRevB.96.224418 (Dec. 2017).

96. Donati, F. unplished.

97. Hartmann-Boutron, F., Politi, P. & Villain, J. Tunneling and magnetic relaxation in mesoscopic molecules. *International Journal of Modern Physics B* **10,** 2577–2637. doi:10.1142/S0217979296001148 (Sept. 1996).

98. Bellessa, G., Vernier, N., Barbara, B. & Gatteschi, D. Phonon-Assisted Tunneling in High-Spin Molecules: Experimental Evidence. *Physical Review Letters* **83,** 416–419. doi:10.1103/PhysRevLett.83.416 (July 1999).

99. Leuenberger, M. N. & Loss, D. Spin tunneling and phonon-assisted relaxation in Mn12-acetate. *Physical Review B* **61,** 1286–1302. doi:10.1103/PhysRevB.61.1286 (Jan. 2000).

100. Domke, M. *et al.* Experimental Proof for Coordination-Dependent Valence of Tm Metal. *Physical Review Letters* **56,** 1287–1290. doi:10.1103/PhysRevLett.56.1287 (Mar. 1986).

101. Gruber, A. *et al.* Scanning Confocal Optical Microscopy and Magnetic Resonance on Single Defect Centers. *Science* **276,** 2012–2014. doi:10.1126/science.276.5321.2012 (June 1997).

102. Baierl, S. *et al.* Nonlinear spin control by terahertz-driven anisotropy fields. *Nature Photonics* **10,** 715–718. doi:10.1038/nphoton.2016.181 (Nov. 2016).

103. Bayliss, S. L. *et al.* Optically addressable molecular spins for quantum information processing. *Science* **370,** 1309–1312. doi:10.1126/science.abb9352 (Dec. 2020).

104. Eisert, J., Friesdorf, M. & Gogolin, C. Quantum many-body systems out of equilibrium. *Nature Physics* **11,** 124–130. doi:10.1038/nphys3215 (Feb. 2015).

105. Afanasiev, D. *et al.* Ultrafast control of magnetic interactions via light-driven phonons. *Nature Materials* **20,** 607–611. doi:10.1038/s41563-021-00922-7 (May 2021).

106. Giannozzi, P. *et al.* Advanced capabilities for materials modelling with Quantum ESPRESSO. *Journal of Physics. Condensed Matter: An Institute of Physics Journal* **29,** 465901. doi:10.1088/1361-648X/aa8f79 (Nov. 2017).

107. Prandini, G., Marrazzo, A., Castelli, I. E., Mounet, N. & Marzari, N. Precision and efficiency in solid-state pseudopotential calculations. *npj Computational Materials* **4,** 1–13. doi:10.1038/s41524-018-0127-2 (Dec. 2018).

108. Perdew, J. P., Burke, K. & Ernzerhof, M. Generalized Gradient Approximation Made Simple. *Physical Review Letters* **77,** 3865–3868. doi:10.1103/PhysRevLett.77.3865 (Oct. 1996).

109. Topsakal, M. & Wentzcovitch, R. M. Accurate projected augmented wave (PAW) datasets for rare-earth elements (RE = La-Lu). *Computational Materials Science* **95,** 263–270. doi:10.1016/j.commatsci.2014.07.030 (Aug. 2014).

110. Cowan, R. D. *The Theory of Atomic Structure and Spectra* (University of California Press, 1981).

111. Yen, J. Y. Finding the K Shortest Loopless Paths in a Network. *Management Science* **17,** 712–716 (1971).

112. Sonntag, A. *et al.* Electric-Field-Induced Magnetic Anisotropy in a Nanomagnet Investigated on the Atomic Scale. *Physical Review Letters* **112,** 017204. doi:10.1103/PhysRevLett.112.017204 (Jan. 2014).

113. Yan, S., Choi, D.-J., Burgess, J. A. J., Rolf-Pissarczyk, S. & Loth, S. Control of quantum magnets by atomic exchange bias. *Nature Nanotechnology* **10,** 40–45. doi:10.1038/nnano.2014.281 (Jan. 2015).

114. Burgess, J. A. J. *et al.* Magnetic fingerprint of individual Fe 4 molecular magnets under compression by a scanning tunnelling microscope. *Nature Communications* **6,** 1–7. doi:10.1038/ncomms9216 (Sept. 2015).

115. Yang, K. *et al.* Probing resonating valence bond states in artificial quantum magnets. *Nature Communications* **12,** 993. doi:10.1038/s41467-021-21274-5 (Feb. 2021).

116. Khajetoorians, A. A., Wegner, D., Otte, A. F. & Swart, I. Creating designer quantum states of matter atom-by-atom. *Nature Reviews Physics* **1,** 703–715. doi:10.1038/s42254-019-0108-5 (Dec. 2019).

117. Vincent, R., Klyatskaya, S., Ruben, M., Wernsdorfer, W. & Balestro, F. Electronic readout of a single nuclear spin using a molecular spin transistor. *Nature* **488,** 357–360. doi:10.1038/nature11341 (Aug. 2012).

118. Thiele, S. *et al.* Electrically driven nuclear spin resonance in single-molecule magnets. *Science* **344,** 1135–1138. doi:10.1126/science.1249802 (June 2014).

119. Godfrin, C. *et al.* Operating Quantum States in Single Magnetic Molecules: Implementation of Grover's Quantum Algorithm. *Physical Review Letters* **119,** 187702. doi:10.1103/PhysRevLett.119.187702 (Nov. 2017).

120. González, S. A. *et al.* Photon-assisted resonant Andreev reflections: Yu-Shiba-Rusinov and Majorana states. *Physical Review B* **102,** 045413. doi:10.1103/PhysRevB.102.045413 (July 2020).

121. Peters, O. *et al.* Resonant Andreev reflections probed by photon-assisted tunnelling at the atomic scale. *Nature Physics* **16,** 1222–1226. doi:10.1038/s41567-020-0972-z (Dec. 2020).

Tobias Bilgeri

Address	Chemin du Tennis 1, 1026 Echandens, Switzerland
Date of birth	20th of July 1993
Born in	Feldkirch, Vorarlberg, Austria
Nationality	Austrian
Telephone	+41 787177832
Email	bilgeri.to@gmail.com

Physicist with a broad range of experience across nanoscale solid state physics, open quantum systems and geophysics, from an experimental, computational and theoretical perspective. I have ample experience in guiding research projects with diverse international teams and delivering excellent results. In my free time, I enjoy participating in data science competitions employing cutting edge machine learning algorithms.

Education

École Polytechnique Fédérale de Lausanne — **Switzerland**
- Ph.D. Physics — 08.2017 – 07.2021

Sorbonne University / UPMC — **France**
- M.Sc. Physics, *summa cum laude* — 08.2016 – 06.2017

University of Cologne — **Germany**
- B.Sc. Physics, *magna cum laude* — 09.2012 – 08.2015

Work Experience

Laval Science AG, Quantitative Researcher — 09.2021 –, **Switzerland**
EPFL, Research and Teaching Assistant (H. Brune) — 08.2017 – 07.2021, **Switzerland**
IBS Center for Quantum Nanoscience, Visiting Scientist (A. Heinrich) — 09.2019 – 06.2020, **Korea**
Sorbonne University, Master's Thesis, Quantum materials (T. Cren) — 02.2017 – 06.2017, **France**
IST Austria, Intern, Quantum Integrated Devices (J. Fink) — 07.2016 – 08.2016, **Austria**
European Institute for Marine Studies, Intern, Theoretical Geophysics — 05.2016 – 06.2016, **France**
Univ. of Cologne, Bachelor's Thesis, Nanomaterials (A. Grüneis) — 04.2015 – 08.2015, **France**
CDM Smith Consult GmbH, Intern, Geophysical Survey Assistant — 10.2013, **Germany**
Plankel Bohrungen GmbH, Intern, Drilling Assistant — 08. – 09.2013, **Austria**
Austrian Armed Forces, National Military Service — 09.2010 – 02.2011, **Austria**
IBS Paper Performance Group, Intern, Various Tasks — 08 – 09.2008, 03. & 09.2011, **Liechtenstein**

Skills, Activities and Interests

Programming: Python (using Numpy, Pandas, Apache Spark, Koalas, Scikit-Learn, XGBoost, TensorFlow, Keras Tuner, Optuna, etc.), Matlab, Scala, Mathematica, Latex
Languages: German, English, French
Hobbies: Motorcycling, Sailing, Backpacking, Diving, Handball, Machine Learning, Quant Finance
Scholarships: 6500€ by LabEx MATISSE at Sorbonne University/UPMC, 10000€ by Institut de Physique du Globe de Paris (declined), Marie Sklodowska-Curie PhD Fellowship at IST Austria (declined).